Tissue Cutting in Needle Biopsy

By

Jason Zachary Moore

A Dissertation Submitted in Partial Fulfillment
Of the Requirements for the Degree of
Doctor of Philosophy
(Mechanical Engineering)
in the University of Michigan
2011

Doctoral Committee:

Professor Albert J. Shih, Chair
Assistant Professor Shorya Awtar
Assistant Professor Samantha Daly
Clinical Professor Patrick McLaughlin

2011

Acknowledgements

I thank my advisor, Professor Albert Shih, for his help guiding me as I conducted the research for this thesis. It was always an adventure.

This thesis would not have been possible without the help of many people from all over the University. I thank Dr. Patrick McLaughlin, who helped open a world of possibilities for needle devices. I also would like to thank Carl McGill, my lab partner, who helped in much of the needle work. I also thank Jonathon Schwartz who assisted in many experiments.

I also thank the visiting scholars of Haojun Zheng and Qinhe Zhang who both helped me pioneer the early biopsy needle work. I specially thank Haojun for inviting me to perform research at Tsinghua University for the summer of 2008 for an amazing experience I will never forget.

Finally, I owe a big thank you to my family, for their encouragement all throughout my life to pursue my dreams. Mom and Dad, I love you very much. Last but not least I thank my wonderful fiancée Sarah, who is always there for me. You are my best friend; I love you.

Table of Contents

List of Figures

List of Appendices

Nomenclature

α	Normal rake angle
γ	Radial position of point on needle cutting edge
γ_2	Radial position of point on non-cutting edge of needle
γ_A	First radial position where Ellipse 1 meets Ellipse 2 on a non-symmetric two-plane needle
γ_B	Second radial position where Ellipse 1 meets Ellipse 2 on a non-symmetric two-plane needle
γ_e	Radial position where Section 1 meets Section 2 on an ECE needle
η	Chip flow angle in oblique cutting
θ	Range of γ where needle contacts tissue at the moment of tissue cutting
λ	Inclination angle
ξ	Bevel angle of a flat plane needle
ξ_1	Bevel angle of non-symmetric two-plane needle that forms Ellipse 1
ξ_2	Bevel angle of non-symmetric two-plane needle that forms Ellipse 2
φ	Angle of wedge that forms ECE needle tip
ψ	Offset angle between planes of non-symmetric two-plane needle
A	Inside needle tip area
B_i	y-intercept of vector $\boldsymbol{g}$ given an inside cutting edge
B_o	y-intercept of vector $\boldsymbol{g}$ given an outside cutting edge
c	Half the width of the top of the wedge that forms the ECE needle tip
$f(\lambda,\alpha)$	Specific force of blade cutting edge given λ and α
F_C	Needle tip cutting edge force
F_L	Needle tip leading edge force
F_N	Initial cutting force for a needle inserted into tissue
G	Slope of $\boldsymbol{g}$ in the xy plane
h	Height offset between two-planes of non-symmetric two-plane needle
K	Positive scale factor for concave and convex needles
l	Tool chip contact length in traditional metal cutting
l_c	Tissue contact length measured towards the center of the ellipse
l_n	Length of Section 2 in the z-direction on an ECE needle tip
l_t	Tissue contact length measured tangent to the cutting edge
l_{xz}	Tissue contact length measured in the xz plane
L	Needle tip insertion length
n	Number of leading needle tip edges
P	Number of planes in multi-plane needle
q	Distance in the x-direction where y = 0 from the inside needle wall to point E
r_i	Inside needle radius

r_o	Outside needle radius
S	Scale factor for comparing blade insertion results to needle force model
t	Needle thickness
A_γ	Plane tangent to the needle cutting face
P_n	Plane with normal vector $\boldsymbol{s}$
P_r	Plane with normal vector $\boldsymbol{v}$
$\boldsymbol{a}$	Vector formed by intersection of P_n and A_γ
$\boldsymbol{b}$	Vector formed by intersection of P_n and P_r
$\boldsymbol{d}$	Derivative vector of the needle profile in the xz plane
$\mathbf{g}$	Vector describing direction of l_t
$\boldsymbol{n_\gamma}$	Normal vector to the needle cutting face
$\boldsymbol{s}$	Tangent vector to the needle tip cutting edge
$\boldsymbol{v}$	Vector describing cutting direction of the needle
$\boldsymbol{v_c}$	Vector describing tissue flow direction on needle tip cutting edge
$\boldsymbol{v_t}$	Vector describing tool direction in oblique cutting

Abstract

This research advances knowledge in needle cutting of tissue leading to the invention and validation of the enhanced cutting edge (ECE) biopsy needle. Biopsy needle tip cutting edge geometry is defined using analytical models. With these geometrical definitions a mechanistic force model is developed to predict the needle insertion force for a given needle geometry. The force model then leads to the development of the improved ECE needle tip geometry.

Needle biopsy is one of the most common medical procedures to cut and remove tissue for pathological diagnosis. Currently little study has focused on hollow needle tissue cutting. This lack of knowledge has led to the use of biopsy needles and devices that are inefficient at cutting tissue, thereby hindering the accuracy of the diagnosis, increasing the discomfort to the patient, and lengthening the procedure time. This dissertation directly fills this void in hollow needle tissue cutting knowledge to improve the yield of biopsy and advance the understanding of hollow needle tissue cutting in biopsy.

This study is conducted in four topics that build on each other to reach the ultimate goal of developing the novel ECE biopsy needle. First, analytical models of needle geometry are developed for identification of inclination angle, normal rake angle, needle tip insertion length, and needle tip area on a variety of flat plane and curved needle tips. Second, oblique tissue cutting is studied through blade and needle tissue cutting experiments and three analytical models are developed to describe tissue flow angle and needle contact length. Third, a general hollow needle insertion force model is developed to predict needle insertion force. Fourth, a novel ECE needle tip is developed based on positive geometrical characteristics discovered by the force model for cutting tissue. This ECE needle is validated against a regular style needle and shown to produce longer biopsy sample lengths.

This research aims to improve the procedure of needle biopsy through increasing fundamental knowledge in needle cutting mechanics and developing the improved needle geometry of the ECE needle. This research can lead to more accurate biopsy diagnosis, lower patient discomfort, and shorter procedure time.

Chapter 1 Introduction

In the mid 1850's Rudolph Verchow developed the concept of diagnosis through examination of cells (Race 2004). Later Ernest Besnier developed the medical term "biopsy" in 1879 to signify a term for collecting tissue samples (Zerbino 1994). Since this time, advances in medical knowledge and pathological equipment have lead to the increased ability to use biopsy as a diagnostic tool.

Today biopsy is one of the most common diagnostic tools used by doctors to detect the presence of abnormalities, such as cancer. In the procedure tissue is removed from a specific location, usually via the assistance of imaging technology. A pathologist takes this tissue and examines it to determine if any abnormalities are present, thereby allowing the doctor and the patient to make a more informed medical choice of action.

There exists a wide variety of biopsy procedures and techniques including fine needle aspiration, open surgical biopsy, and core needle biopsy. Fine needle aspiration is for removing fluid or individual cells from the body via syringe and small diameter needle. Open surgical biopsy is an invasive procedure where a surgeon goes into the body and cuts out a piece of tissue for examination. Core needle biopsy is the most preferred for removing tissue because a thin needle is used to remove tissue making it a minimally invasive procedure.

There are two main styles of needle core biopsy: the tru-cut and end-cut needle biopsy, as shown in Figure 1.1. Both methods use a hollow needle and stylet (solid rod) to capture the sample. To perform the tru-cut method (Figure 1.1(A)): first step the needle is position in front of the biopsy target, second step the stylet which has a notch cut into the side advances forward, and third step the biopsy needle advances forward cutting the tissue leaving a trapped specimen inside the needle. To perform the end-cut method (Figure 1.1(B)): first step the needle is position in front of the biopsy target, and in the second step the hollow needle advances forward cutting the tissue and a mechanism seals

the sample inside the needle. The length of the biopsy sample is usually less than the needle insertion length due to inefficiencies in cutting by the needle tip edge geometry and the resistance due to friction of tissue moving inside the needle.

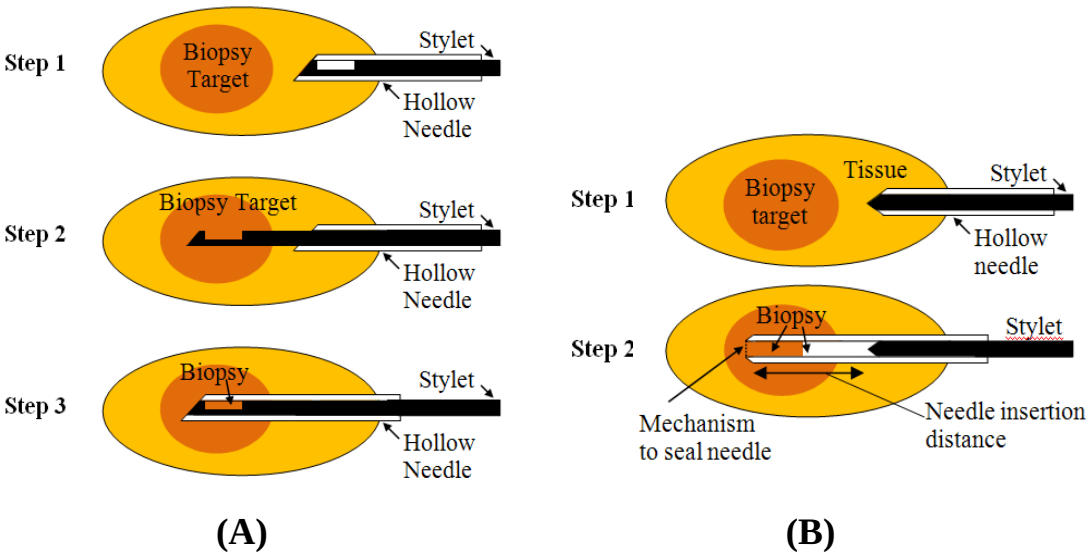

Figure 1.1: (A) Tru-cut and (B) end-cut needle biopsy

The needle tip geometry is an important factor for an efficient biopsy. Needle tips come in a wide variety of shapes and designs. Several commercialized needle tip designs are shown in Figure 1.2.

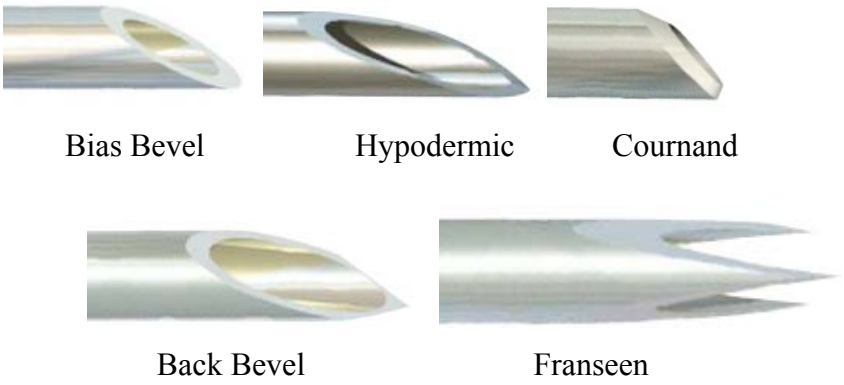

Figure 1.2: Common needle tip styles

1.1 Research Motivation

An increase in cancer rates combined with the emergence of early detection methods for cancer has greatly increased the frequency of needle biopsy procedures. For example, for early detection of prostate cancer, the most common cancer in men, the prostate specific antigen (PSA) level in the blood can be easily tested. If the PSA level is greater than 4 ng/ml, a needle biopsy is performed to confirm the presence of cancer. The increased frequency of mammograms for breast cancer, and advanced imagining scans (MRI, CT, PET, ect.) for other cancers has also increased the frequency of needle biopsy procedures, which are necessary to confirm a diagnosis of cancer.

There is a lack of cutting efficiency in current needle biopsy designs which hinders the accuracy of the diagnosis, increases the discomfort to the patient, and lengthens the procedure. Current prostate biopsy procedures are shown to produce false negative results as high as 24% of the time (Lane 2008). Higher needle cutting efficiency has been proven in the case of prostate cancer to increase the accuracy of diagnosis because a greater volume of tissue can be captured with a single needle insertion and examined (Iczkowski 2002). By capturing longer biopsy samples with a single needle insertion fewer additional needle insertions are necessary. This allows for faster operation speed and less pain to the patient. The shorter procedure time will allow for the surgeon to operate on more patients in a given time frame thereby reducing the economic cost for both the patient and health insurance companies.

Currently limited research has been performed on hollow biopsy needle geometry. More efficient biopsy cutting methods can be developed with a better understanding of how specific factors influence the biopsy outcome. This research strives to fill this gap in knowledge.

1.2 Needle

1.2.1 Needle outside and inside diameters

The basic dimensions of the needle are given by the needle gauge size and the wall thickness. The needle gauge size gives the outside diameter of the needle. For example, the 18 gauge needle, which is commonly used in prostate biopsy, has 1.27 mm outside diameter. The wall thickness of a needle typically comes in four size classes,

from largest to smallest: regular wall (RW), thin wall (TW), extra thin wall (XTW), and ultra thin wall (UTW). For example, Figure 1.3 (B) and (C) show the UTW and RW 18 gauge bias bevel needles, which have 0.076 and 0.220 mm thickness, respectively. The selection of wall thickness greatly affects the inside volume and efficiency in biopsy. UTW needles are commonly used for biopsy applications.

1.2.2 Needle tip geometry

Commercial needle tips are generated by a special burr-free grinding process, which typically creates a plane, Figure 1.3(A). By indexing the needle tip in different orientations during grinding, various needle tip geometries can be generated. More advanced needle geometries are made of curved surfaces which will be discussed in detail in Chapter 2.

A multi-plane needle contains planes oriented symmetrically or non-symmetrically around the needle, as shown in Figure 1.4. A symmetric orientation means that the planes are tilted an equal angle relative to the needle axis and are placed in equal intervals around the circumference of the cylindrical needle; while a non-symmetric design means the planes are oriented in any other configuration. Defining the orientation for non-symmetrical needles is more complex due to the added variables. Figure 1.4 shows both two and three-plane symmetric and non-symmetric needle tips. Any number of planes can be used to form a plane needle tip.

The curved leading edge of the needle tip acts as the tool cutting edge, as marked in Figure 1.3 and Figure 1.4. For the bias bevel needle, the cutting edge transitions from the outer edge to the inner edge. In the case of multi-plane formed needles, the cutting edge is usually only the inner edge. The geometry of the cutting edge has a major impact on the cutting performance of the needle.

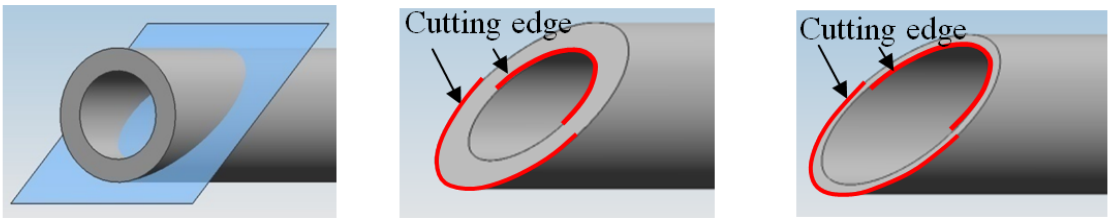

(A) (B) (C)

Figure 1.3: One-plane bias bevel needle tip and cutting edge: (A) generation of needle tip by a plane, (B) RW needle, and (C) UTW needle

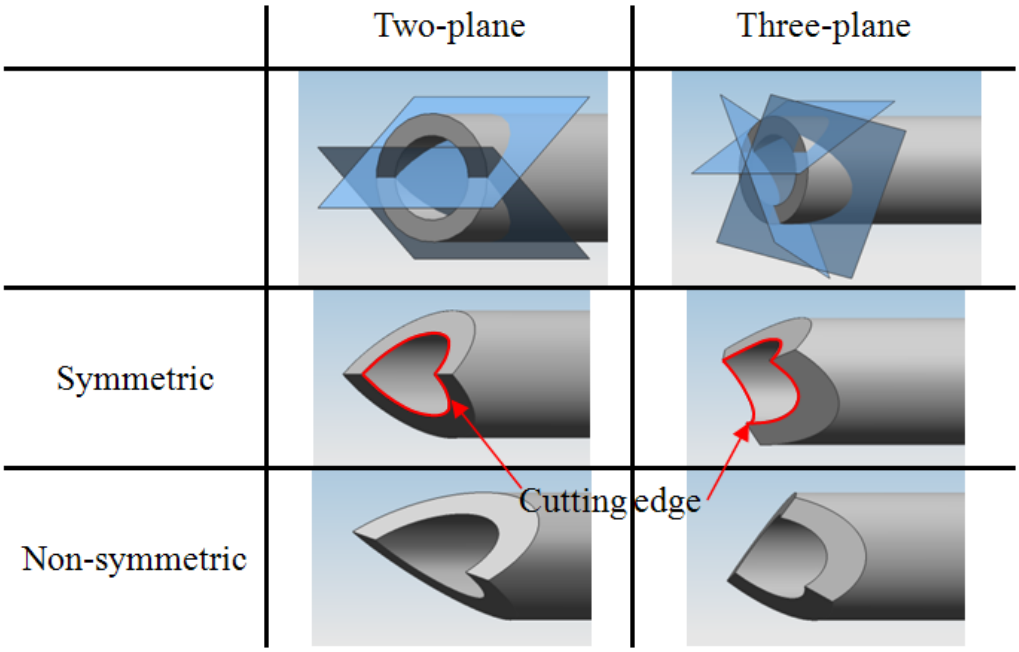

Figure 1.4: Multi-plane symmetric and non-symmetric needle tip

1.3 Literature Review

1.3.1 Needle tip cutting geometry

In machining, the tool geometry is critical to the cutting operation (Boothroyd 2006). Two critical parameters at the cutting point are the normal rake angle, α, and inclination angle, λ (Stephenson 2006). These angles define the geometry of the cutting edge. Experimental results have shown that inclination angle affects the forces on the needle upon insertion and that too low of a λ fails to successfully cut the tissue (Moore

2009a, Zheng 2009). Understanding the values λ and α is important for selecting the needle geometry for efficient cutting.

Although needles are widely used, there is limited research on needle cutting geometry. Effects of needle geometry on insertion forces and needle deviation were analyzed by O'Leary et al. (2003) and Podder et al. (2005) for solid needles. Needle bending analysis due to basic bevel needle geometry has been performed in many studies (Okamura 2004, Glozman 2004, Webster 2006, and Abolhassani 2007). Defining the needle geometry along with α and λ for any style of needle is a challenge that has yet to be thoroughly examined; rather much work has focused on the effects of needle geometry.

1.3.2 End-cut versus tru-cut biopsy

The tru-cut biopsy method lacks sample volume efficiency, because only a fraction of the stylet's volume can be used to collect tissue. The end-cut biopsy, as shown in Figure 1.1(B), uses the tip of the needle to perform the tissue cutting and the full volume of the hollow needle can collect the cut tissue (Haggarth 2002).

Studies have shown that end-cut needles can produce significantly longer samples with less fragmentation than a tru-cut biopsy needle; however, the results are much less consistent (Ubhayaker 2002, Ozden 2003). Longer biopsy lengths have been shown to lead to significantly better cancer detection making the concept of end-cut biopsy needles very appealing (Fink 2005, Iczkowski 2002).

End-cut needles variability in performance has led to their lack of acceptance in prostate biopsy procedures. Historically end-cut biopsy needles have always had performance stability problems as reported by the early work of Hopper et al. (1993a, 1993b, 1995). The BioPince needle attempts to correct this problem by having a mechanism seal the needle tip as shown in Figure 1.1(B); however, studies have shown it still has a 27% failure rate of successful tissue capture (Ubhayakar 2002). Such a high failure rate currently makes the tru-cut biopsy needle the better choice even though its shorter biopsy length provides less than ideal coverage.

1.3.3 Tissue cutting modeling

Extensive research has been conducted to investigate the needle-tissue interaction upon solid needle insertion with the ultimate aim to build a haptic model for surgical procedures (Brett 1997, Kataoka 2002, DiMaio 2003, Okamura 2004, Hing 2006, Podder 2006). Podder et al. (2005) investigated the effect of needle tip geometry on force and deflection. Chanthasopeephan (2006) studied the tissue cutting force using a sharp, computer-controlled knife with the aim to build a computational model for haptic display. Dehghan et al. (2007) used an ultrasonic-based motion measurement tool to quantify the accuracy of the model for brachytherapy, a medical procedure using needles to guide radioactive seeds into position for treatment. Abolhassani et al. (2007) presents the most recent survey of needle insertion in soft tissue, including the modeling of needle insertion forces, tissue deformation, needle deflection, robot assisted needle insertion, and the effect of trajectories on tissue deformation.

Unfortunately none of these studies can be directly applied to biopsy needle cutting which uses a hollow needle. Hollow needle cutting differs from solid needle cutting because the contact length, length that tissue is in contact with the metal needle tip, of a hollow needle is significantly smaller. The literature survey shows that results are lacking on the variation of forces along the cutting edge of a hollow needle. The knowledge of tissue cutting forces is an indispensible tool in the design of effective needle tip geometries.

1.4 Research Scope, Goals and Tasks

The scope of this research is to determine positive geometrical needle tip characteristics that can be applied to needle tip design for the creation of a more effective needle tip geometry. Analysis of tissue cutting forces and a better understanding of needle geometry are keys to developing a successful biopsy method. The major goal of this research is the development of a needle tip design that can capture a larger sample of tissue (high cutting efficiency).

Currently there has been little analysis of hollow needle geometry and how geometry affects cutting performance. This research fills this void by giving detailed

analysis of how the parameters of λ and α affect biopsy cutting force. The tasks of this research include:

- Mathematical modeling of needle geometry for identification of inclination angle, normal rake angle, needle tip insertion length, needle tip area, and contact length
- Determination of tissue oblique cutting flow angle and contact length of a needle
- Development and validation of a hollow needle insertion force model
- Creation and validation of an improved needle geometry, the enhanced needle edge (ECE) needle

1.5 Outline

This report presents modeling of needle tip cutting edge geometry, tissue oblique cutting flow angle experiments and models, hollow needle force model, and ECE needle development and validation. Layout is described in the following paragraphs.

Chapter 2 provides mathematical models of needle tip geometry for inclination angle, normal rake angle, needle tip insertion length, and needle tip area on a variety of different needles. Both plane style and curved surface needles are examined.

Chapter 3 provides three mathematic models of tissue oblique cutting flow angle and contact length of a needle. Experimental results are presented to explore tissue flow angle on a needle.

Chapter 4 develops a needle tip insertion force model based on elementary cutting tool edges (ECT). Blade experiments are performed to develop a specific force model of which the needle force model is based. Needle insertion experiments are used to validate the model.

Chapter 5 develops the concept of the enhanced cutting edge (ECE) needle tip design. Biopsy experiments are performed that show the ECE needle is able to outperform conventional style needles tips.

Chapter 6 summarizes conclusions and presents future work that can further improve the procedure of needle biopsy.

Chapter 2 Needle Tip Cutting Edge Geometry

This chapter is based on Moore et al. (2010a and 2009b). The inclination angles and normal rake angles for flat planes and curved surfaces are explored. The insertion length and inside needle tip area is also explored for symmetric multi-plane needle tips.

2.1 Mathematical Model for Inclination Angle of Plane Needles

2.1.1 Bias bevel needle tip

The bias bevel needle is made by one-plane being ground at a specified bevel angle, ξ, as shown in Figure 2.1. A *xyz* axis with the *z* axis coinciding with the needle axis and the *x* axis passing through the lowest point of the outside needle tip radius, r_o. The radial position of a point A along the needle is defined as γ.

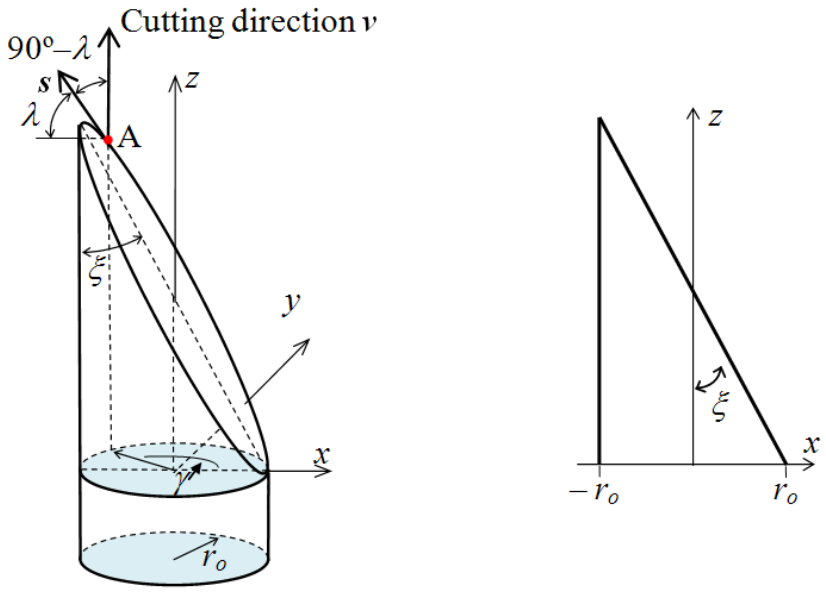

(A) (B)

Figure 2.1: Bias bevel needle model: (A) bias needle tip and (B) *xz* cross-section

When observing the bias bevel needle in the *xz* plane, as shown in Figure 2.1(B), the needle profile forms a straight line with a slope of $-\cot \xi$ and a *z* intercept of $r_o \cot \xi$, thereby yielding the equation of $z = (r_o - x) \cot \xi$. Putting in terms of γ, the parametric equations of an ellipse to define the shape of the needle tip are:

$$\begin{aligned} x &= r_o \cos \gamma \\ y &= r_o \sin \gamma \\ z &= r_o (1 - \cos \gamma) \cot \xi \end{aligned} \tag{2.1}$$

The normal vector of the *xy* plane $\boldsymbol{v} = \{0, 0, 1\}$ and the tangent vector $\boldsymbol{s}$, shown at point A on Figure 2.1(A), can be expressed as: $\boldsymbol{s} = \{-r_o \sin\gamma, r_o \cos\gamma, r_o \cot\xi \sin\gamma\}$. The angle between the P_r plane (plane with normal vector $\boldsymbol{v}$) and $\boldsymbol{s}$ is the inclination angle, λ.

$$\sin \lambda = \frac{|\boldsymbol{s} \bullet \boldsymbol{v}|}{\|\boldsymbol{s}\| \, \|\boldsymbol{v}\|} = \frac{|\cot \xi \sin \gamma|}{\sqrt{1 + \cot^2 \xi \sin^2 \gamma}} \tag{2.2}$$

The equation for λ of one-plane bias bevel needle tip is:

$$\lambda(\xi, \gamma) = \arcsin \frac{|\cot \xi \sin \gamma|}{\sqrt{1+\cot^2 \xi \sin^2 \gamma}} \quad (0 \le \gamma \le 2\pi) \tag{2.3}$$

2.1.2 Symmetrical multi-plane needle tip

A symmetrical multi-plane needle tip is formed by evenly spaced planes being positioned at identical bevel angles (ξ). Two-plane and three-plane needle tips are shown in Figure 2.2. The *xyz* axis is defined using the same rule as in the bias bevel needle. Commercially, the three-plane symmetric needle is called a Franseen needle.

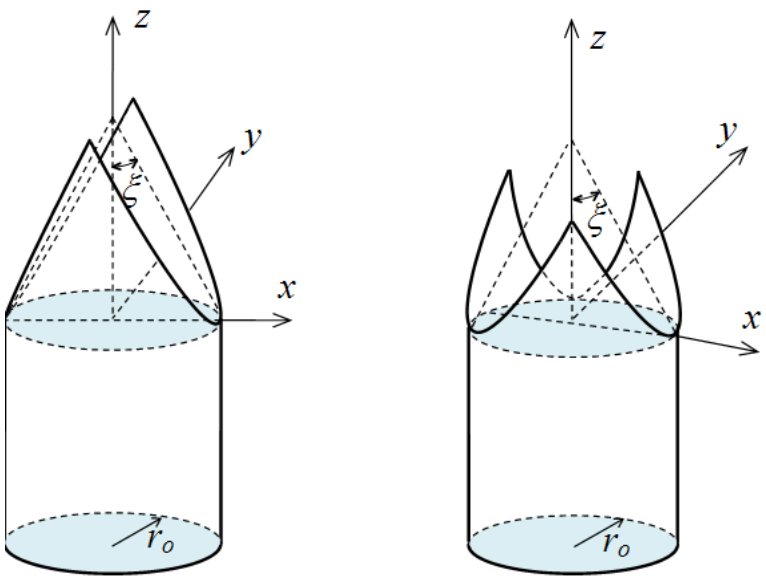

(A) (B)

Figure 2.2: Multi-plane symmetrical needles: (A) two-plane and (B) three-plane (Franseen)

The geometry of a symmetric multi-plane needle is based on the same principles of using the parametric equations for an ellipse, Equation 2.1. The inclination angle for a symmetrical multi-plane needle is based on Equation 2.3 with a phase shift of $-(i-1)\frac{2\pi}{P}$ applied to γ where the P (≥ 2) is an integer representing the number of planes and i (= 1, 2, … , P) defines which segment of the plane is being examined. This leads to the general inclination angle equation for the symmetrical multi-plane needle being:

$$\lambda(\xi, P, \gamma) = \arcsin \frac{\left|\cot\xi \sin\left(\gamma-(i-1)\frac{2\pi}{P}\right)\right|}{\sqrt{1+\cot^2\xi \sin^2\left(\gamma-(i-1)\frac{2\pi}{P}\right)}} \quad \frac{\pi}{P}(2i-3) \leq \gamma \leq \frac{\pi}{P}(2i-1) \qquad (2.4)$$

2.1.3 Non-symmetrical two-plane needle tip

A non-symmetric needle formed by two-planes, as shown in Figure 2.3, can be fully defined given the offset height between two-planes (h), offset angle between planes (ψ), the bevel angle of the two-planes relative to the z axis (ξ_1 and ξ_2), and r_o. The needle

cutting edge is formed by two ellipses, marked as Ellipses I and II. These two ellipses intersect at two sharp tips. The non-symmetry of the planes makes determining the position of the sharp tip of the needle, i.e., location where the two planes meet, difficult. These two sharp points, marked as A and B in Figure 2.3, have γ equals γ_A and γ_B, respectively.

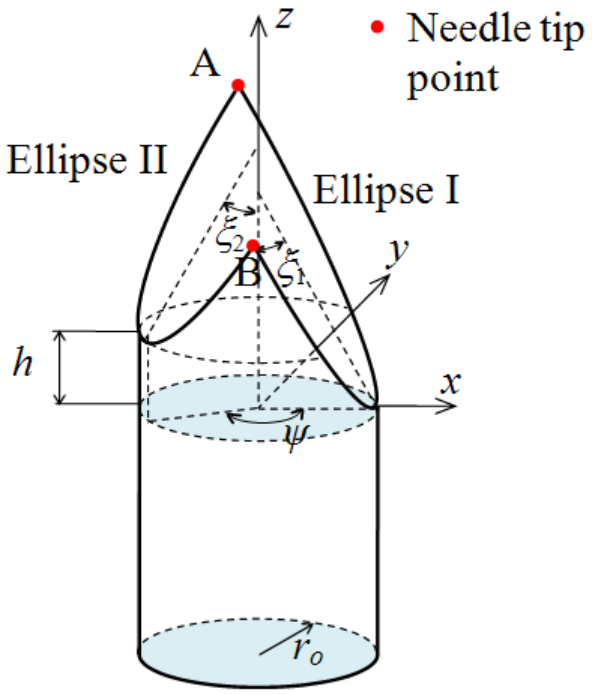

Figure 2.3: Non-symmetric two-plane needle

Based on Equation 2.1, the parametric equations for Ellipse I with bevel angle ξ_1 are:

$$\begin{aligned} x_1(\gamma) &= r_o \cos\gamma \\ y_1(\gamma) &= r_o \sin\gamma \\ z_1(\gamma) &= r_o (1 - \cos\gamma) \cot\xi_1 \end{aligned} \tag{2.5}$$

The parametric equations for Ellipse II can be formed by adding a phase shift, ψ, and the change in height, h.

$$x_2(\gamma) = r_o \cos\gamma$$

$$y_2(\gamma) = r_o \sin \gamma \tag{2.6}$$
$$z_2(\gamma) = r_o (1 - \cos (\gamma + \psi)) \cot \xi_2 + h$$

The location of where the two-planes meet is then found by setting $z_1(\gamma) = z_2(\gamma)$.

$$r_o (1 - \cos \gamma) \cot \xi_1 = r_o (1 - \cos (\gamma + \psi)) \cot \xi_2 + h \tag{2.7}$$

The Maple software ver. 12 (Waterloo Maple Inc.) is used to solve this equation in terms of γ_A and γ_B, the location where two ellipses meet. The solution of γ_A and γ_B is long and presented in the Appendix A.

The inclination angle can be found at any γ along the radius of the needle for Ellipses I and II.

$$\lambda(\xi_1, \gamma) = \arcsin \frac{\left|\cot \xi_1 \sin \gamma\right|}{\sqrt{1 + \cot^2 \xi_1 \sin^2 \gamma}} \quad (0 \le \gamma \le \gamma_A) \text{ and } (\gamma_B \le \gamma \le 2\pi)$$
$$\lambda(\xi_2, \psi, \gamma) = \arcsin \frac{\left|\cot \xi_2 \sin(\gamma + \psi)\right|}{\sqrt{1 + \cot^2 \xi_2 \sin^2(\gamma + \psi)}} \quad (\gamma_A \le \gamma \le \gamma_B) \tag{2.8}$$

2.2 Mathematical Model for Normal Rake Angle of Plane Needles

The oblique cutting configuration is applied to find the normal rake angle at a point on a bias bevel needle cutting edge. The normal rake angle, α, is defined as the angle between two planes P_r and A_γ measured in plane P_n, as shown in Figure 2.4. P_r is the plane at cutting point and parallel to the *xy* plane, A_γ is the face plane of the needle tip surface, and P_n is a plane with a normal vector ***s***, vector tangent to cutting edge (Boothroyd 2005). These three planes can be found on a bias bevel needle tip as shown in Fig. 7. The normal vector to these planes are defined using γ, ξ, and r_o. The plane P_r has a normal vector $\boldsymbol{v} = \{0,0,1\}$, plane A_γ has a normal vector $\boldsymbol{n_\gamma} = \{\cos \xi, 0, \sin \xi\}$, and plane P_n has a normal vector $\boldsymbol{s} = \{- r_o \sin \gamma, r_o \cos \gamma, r_o \cot \xi \sin \gamma\}$.

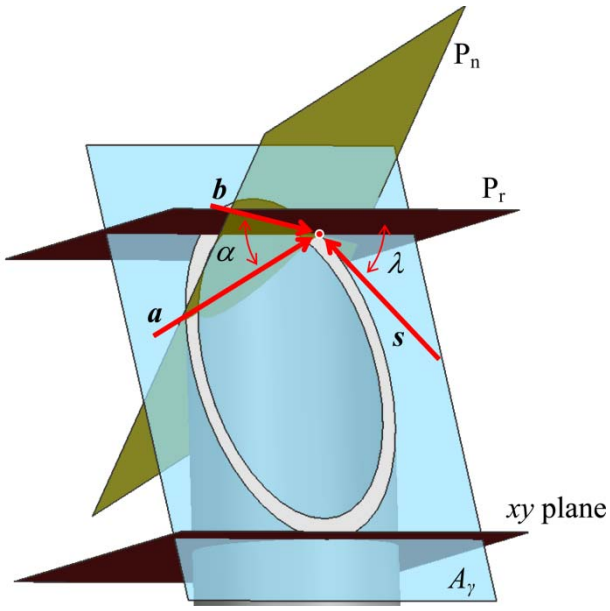

Figure 2.4: Definition of rake angle in the bias bevel needle

Vectors ***a*** and ***b*** mark the intersection of planes P_n A_γ and P_n P_r, respectively, as illustrated in Fig. 7. Vectors ***a*** and ***b*** are defined using the cross products of the normal vectors:

$$\boldsymbol{a} = \boldsymbol{s} \times \boldsymbol{n}_\gamma = \{ r_o \cos\gamma \sin\xi,\ r_o \cot\xi \sin\gamma \cos\xi + r_o \sin\gamma \sin\xi,\ - r_o \cos\gamma \cos\xi \} \tag{2.9}$$

$$\boldsymbol{b} = \boldsymbol{s} \times \boldsymbol{v} = \{ r_o \cos\gamma,\ r_o \sin\gamma,\ 0 \} \tag{2.10}$$

The rake angle for a bias bevel needle is the angle between vector ***a*** and ***b***:

$$\alpha = \arccos \frac{\boldsymbol{a} \bullet \boldsymbol{b}}{\|\boldsymbol{a}\| \|\boldsymbol{b}\|} = \arccos\sqrt{\cos^2\gamma \sin^2\xi + \sin^2\gamma} \tag{2.11}$$

Equation 2.11 can also be applied to two-plane symmetric needles because the elliptical cutting edge of a bias bevel needle is identical to that of a two-plane symmetric needle.

2.3 Inclination Angle of Curved Surface Needle

The inclination angle for any style of continuously differentiable, first order derivative of cutting edge is continuous (class C^1), curved needle tip can be found once the needle tip geometry of the cutting edge is defined. An example of this style of needle is shown in Figure 2.5. The outside radius of the needle is r_o, the inside radius is r_i, and γ is the radial position of a point on the needle cutting edge.

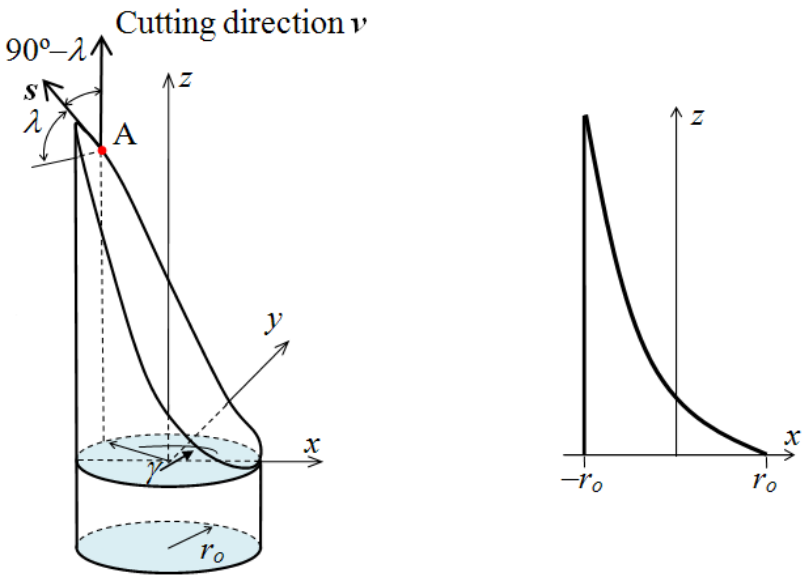

(A) (B)

Figure 2.5: Curved surface needle: (A) outside curved profile and (B) *xz* cross section

Parametric Equations 2.12 and 2.13 respectively describe the inside and outside needle edge.

$$\begin{aligned} x_o &= r_o \cos\gamma \\ y_o &= r_o \sin\gamma \\ z_o &= \text{any continuously differentiable equation} \end{aligned} \tag{2.12}$$

$$\begin{aligned} x_i &= r_i \cos\gamma \\ y_i &= r_i \sin\gamma \\ z_i &= \text{any continuously differentiable equation} \end{aligned} \tag{2.13}$$

For constructing a needle using traditional grinding techniques, a surface would be cut into a needle that mathematically could be described as a two dimensional line being extruded in a linear direction. This constant slope along the needle edge causes the inside and outside cutting edges to be identical except for the radius that describe its position, $z_o'(\gamma)/z_i'(\gamma) = r_o/r_i$. All of the curved surface needles discussed will be of this type.

The normal vector of the *xy* plane is $\boldsymbol{v} = \{0, 0, 1\}$. The tangent vector $\boldsymbol{s}$, shown at point A on Figure 2.5(A), can be expressed as: $\boldsymbol{s} = \{-r_o \sin\gamma, r_o \cos\gamma, z_o'(\gamma)\}$. The angle between the P_r plane (plane with normal vector $\boldsymbol{v}$) and $\boldsymbol{s}$ is the inclination angle, λ.

$$\sin\lambda = \frac{|\boldsymbol{s}\cdot\boldsymbol{v}|}{\|\boldsymbol{s}\|\|\boldsymbol{v}\|} \tag{2.14}$$

This leads to the equations for the inclination angle of any differentially curved needle:

$$\lambda = \arcsin\frac{|z_o'(\gamma)|}{\sqrt{r_o^2 + z_o'(\gamma)^2}} \quad \text{(when } \gamma \text{ is on outside cutting edge)} \tag{2.15}$$

$$\lambda = \arcsin\frac{|z_i'(\gamma)|}{\sqrt{r_i^2 + z_i'(\gamma)^2}} \quad \text{(when } \gamma \text{ is on inside cutting edge)} \tag{2.16}$$

Needles formed by 2-d lines being extruded in a linear direction contain the same slope along the inside cutting edge as the outside cutting edge, meaning the radius dependence will drop out of the inclination angle equations and Equation 2.15 will equal Equation 2.16 around the entire needle ($0 \le \gamma \le 360°$). If the needle tip is formed in another way then special attention must be taken to determine where there is an inside cutting edge and an outside cutting edge. On one plane bias bevel needles for instance, for $-90° < \gamma < 90°$, the inside needle edge acts as the cutting edge and, for $90° < \gamma < 270°$, the outside needle edge acts as the cutting edge.

2.4 Rake Angle of Curved Needle

As illustrated in Figure 2.6, the rake angle of a needle can be defined using the planes of P_r, A_γ, and P_n as with plane needles. Unlike inclination angle, the rake angle is

determined by two parameters, the cutting edge that defines the ***s*** direction and the location of the needle face defined by $\boldsymbol{n_\gamma}$, normal vector to A_γ.

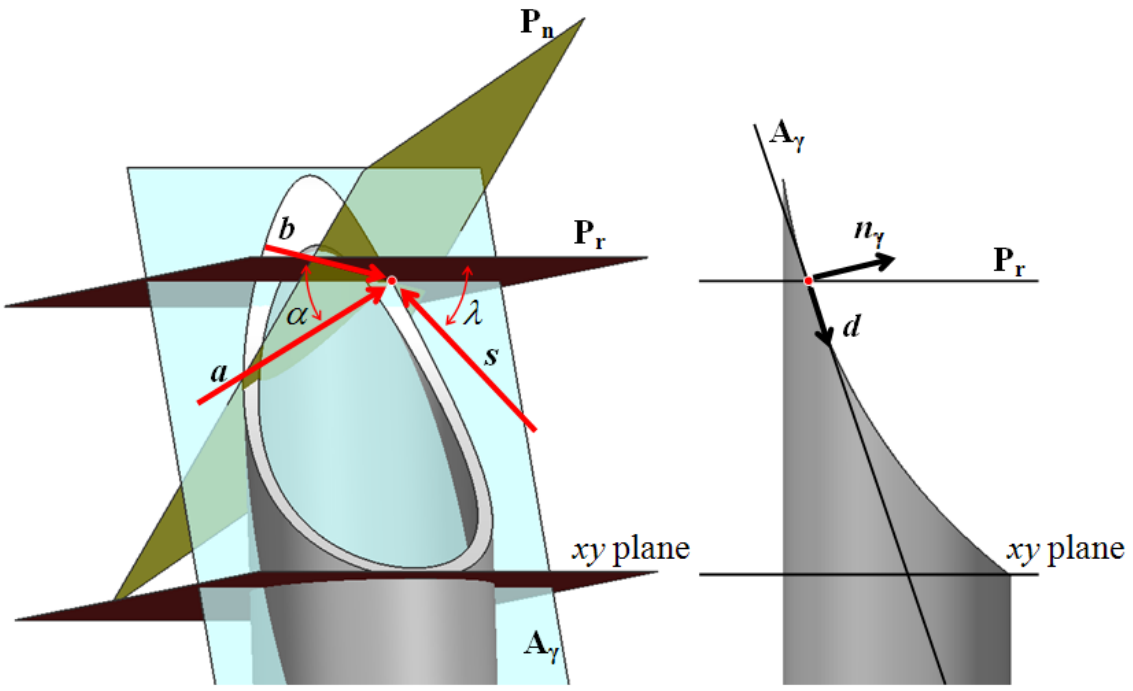

Figure 2.6: Rake angle of a curved surface needle

If the needle surface is formed by a 2-d line drawn in the *xz* plane being extruded in the *y* direction (a configuration that could be easily ground into a needle), vector $\boldsymbol{s} = \{-r_o \sin\gamma\ ,\ r_o \cos\gamma,\ z_o'(\gamma)\}$ around the entire needle and $\boldsymbol{n_\gamma}$ is found based on the needle profile in the *xz* plane, as shown in Figure 2.6. The derivative vector of the curve in the *xz* plane is $\boldsymbol{d} = \{1,\ 0,\ z_o'(\gamma)/(-r_o \sin\gamma)\}$, that must be perpendicular to the $\boldsymbol{n_\gamma}$ vector, $\boldsymbol{d} \bullet \boldsymbol{n_\gamma} = 0$. Solving this finds $\boldsymbol{n_\gamma} = \{\ z_o'(\gamma)/(r_o \sin\gamma),\ 0,\ 1\}$.

Vectors ***a*** and ***b*** represent the intersection of planes P_n A_γ and P_n P_r, respectively, and can be found as:

$$\boldsymbol{a} = \boldsymbol{s} \times \boldsymbol{n_\gamma} = \{r_o \cos\gamma,\ \frac{z_o'(\gamma)^2}{r_o \sin\gamma} + r_o \sin\gamma\ ,\ -z_o'(\gamma)\cot\gamma\} \tag{2.17}$$

$$\boldsymbol{b} = \boldsymbol{s} \times \boldsymbol{v} = \{r_o \cos\gamma,\ r_o \sin\gamma,\ 0\} \tag{2.18}$$

The rake angle is the angle between vectors $\boldsymbol{a}$ and $\boldsymbol{b}$:

$$\alpha = \arccos \frac{\boldsymbol{a}\cdot\boldsymbol{b}}{\|\boldsymbol{a}\|\|\boldsymbol{b}\|} = \arccos \frac{{r_o}^2+{z_o}'(\gamma)^2}{r_o\sqrt{{r_o}^2+{z_o}'(\gamma)^2(2+\cot^2\gamma)+\frac{{z_o}'(\gamma)^4}{{r_o}^2\sin^2\gamma}}} \tag{2.19}$$

2.5 Cutting Length and Inside Needle Tip Area

The cutting length of the needle (L) and the inside needle tip area (A) have yet to be explored in hollow needle research. The cutting length is defined as the length of the needle tip in the z direction, as shown in Figure 2.7. This is an important parameter because the tissue must travel over this length before it can be cut and captured inside the biopsy needle. Ideally the cutting length should be as small as possible to minimize the needle insertion depth needed to capture the tissue.

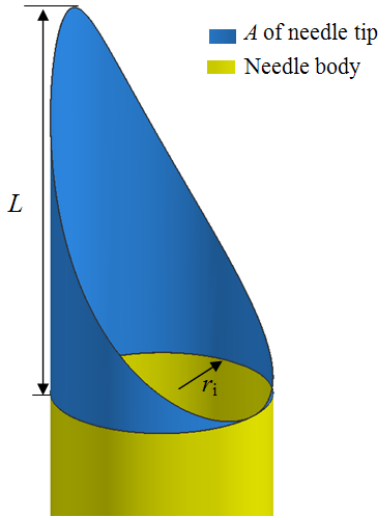

Figure 2.7: Insertion length (L) and inside area (A) of needle tip

The increase in inside needle tip area upon insertion is an important parameter because it determines the amount of friction the biopsy segment will encounter as it first begins to slide into the needle, as shown in Figure 2.7. If this initial friction force is too great, the biopsy segment may not flow into the needle, causing the biopsy to not capture any tissue.

A MatLab program was created to solve the values of A along insertion and L on symmetric multi-plane needle tips. The necessary inputs were the number of planes, the bevel angle, and the inside needle radius.

2.6 Results and Discussion of Inclination Angle for Plane Needles

2.6.1 Bias bevel needle tip

Figure 2.8 shows the inclination angle for three bias bevel needle tips with ξ = 15º, 30º and 45º found using Equation 2.3. At γ = 0º and 180º, λ is equal to 0º, regardless of ξ. The tip of the bias bevel needle (γ = 180º), where the needle first contacts tissue during insertion, has λ = 0º, which is the worst cutting configuration for needle insertion. This problem can be solved using the multi-plane needle.

Smaller ξ creates larger inclination angles where the maximum λ = 90º–ξ for a bias bevel needle. A larger ξ reduces λ thereby creating higher cutting forces. For other types of plane needles the bevel angle dictates the maximum possible inclination angle where $\lambda \leq 90º-\xi$.

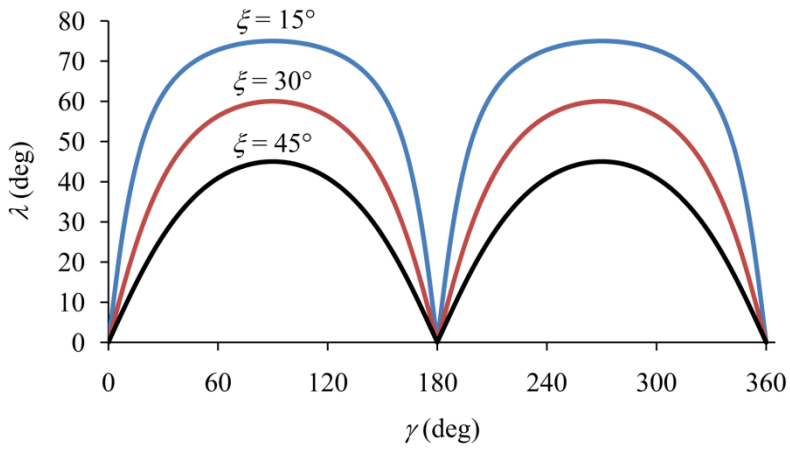

Figure 2.8: Inclination angle of the bias bevel needles

2.6.2 Symmetrical multi-plane needle tip

A multi-plane symmetric needle's inclination angle can be solved using Equation 2.4. The perspective view and λ of a symmetric multi-plane needle tip of P = 2, 3, and 4, ξ = 30º, and r_o = 1 mm are shown in Figure 2.9. The number of needle tip points (sharp

points that occur where ellipses meet and equally space around the radius) on the needle tip is equal to P.

Similar to the bias bevel needle, as shown in Figure 2.8, the minimum λ is also equal to 0º for all symmetric multi-plane needles. Unlike the bias bevel needle, the location of $\lambda = 0º$ is the last point and not the first point on the needle tip cutting edge contacting the tissue. The number of points where $\lambda = 0º$ is equal to the number of planes used to construct the needle, because $\lambda = 0º$ is located at the bottom of the ellipse formed by each plane.

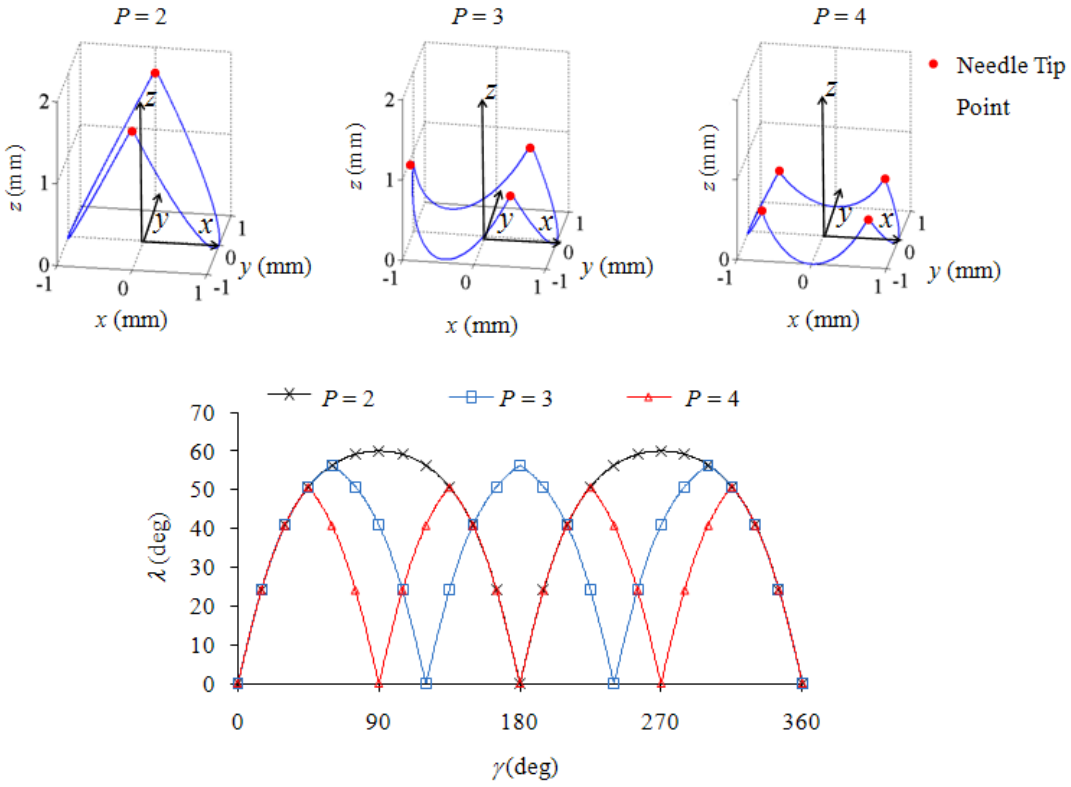

Figure 2.9: Cutting edge profile and λ for multi-plane needles with $P = 2$, 3, and 4, $\xi = 30º$, and $r_o = 1$ mm

At a tip of the multi-plane needle where the needle first contacts tissue during insertion ($\gamma = 90º$ for $P = 2$, $\gamma = 66.7º$ for $P = 3$, and $\gamma = 45º$ for P=4), the λ is maximum, which is the best cutting configuration for needle insertion. This is opposite to the bias bevel needle with $\lambda = 0º$ at the needle tip point. The $\lambda = 60º$, 56.3º, and 50.8º for $P = 2$, 3,

and 4, respectively, for $\xi = 30^{\circ}$. For a given ξ, increase the P beyond two reduces the maximum λ, thereby, making the needle less effective at cutting.

The effect of ξ on λ of multi-plane needles with $P = 3$ and 4 is shown in Figure 2.10. The same trend as seen in the bias bevel needle (Figure 2.8) is observed, that the increase in ξ reduces the λ.

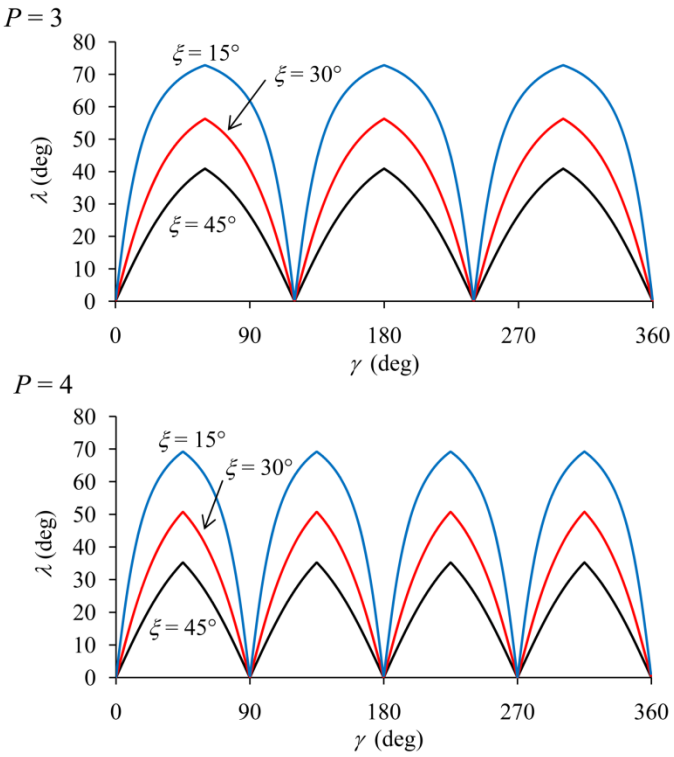

Figure 2.10: Inclination angle of a symmetrical multi-plane needle ($P = 3$ and 4) with $\xi =$ 15º, 30º and 45º

2.6.3 Non-symmetrical two-plane needle tip

The effects of ψ and h on λ of non-symmetric two-plane needles are discussed in the following two sections.

2.6.3.1 Effect of ψ

Figure 2.11 shows the shape of the needle cutting edge and λ for $\xi_1 = 30º$, $\xi_2 = 30º$, $r_o = 1$ mm, $h = 0$ mm, and $\psi = 45º$, 90º, and 180º. Increasing ψ shifts the location of the maximum and minimum λ which occur on Ellipse II. Ellipse I remains fixed in place,

therefore, the λ from $0^{o} \leq \gamma \leq 90^{o}$ remains the same as ψ varies from 45° to 180°. Changing ψ can lower the high λ that occurs on Ellipse II, thereby, making it more difficult to cut the soft tissue.

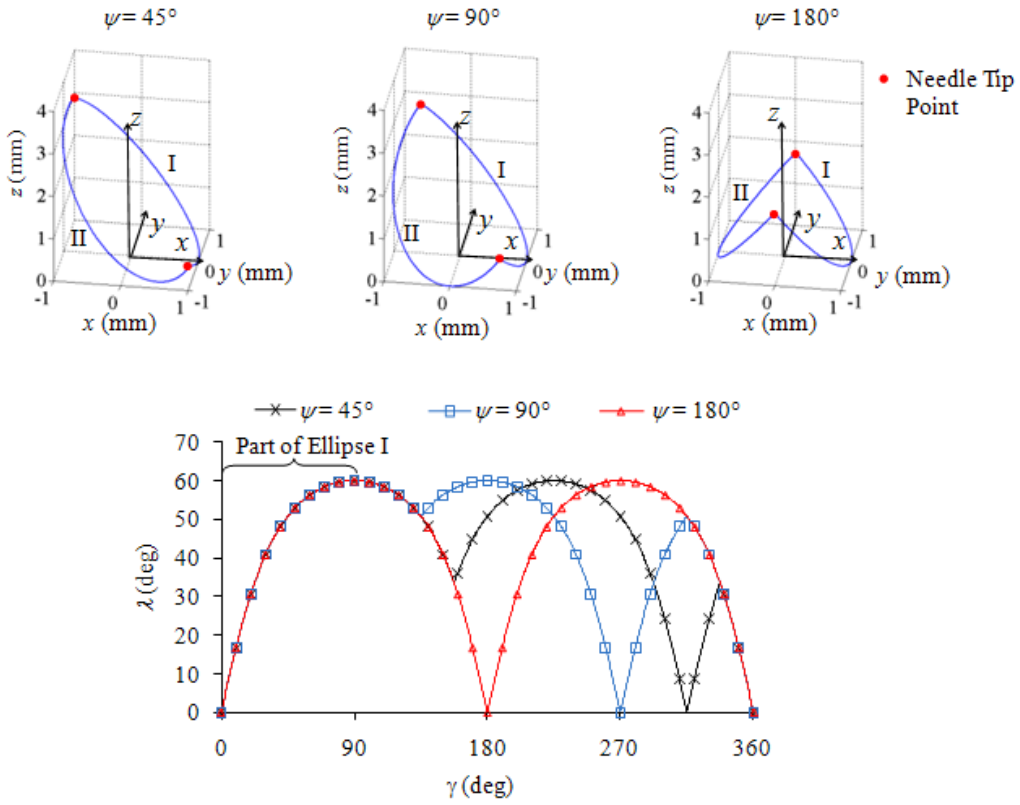

Figure 2.11: Cutting edge profile and λ when $\xi_1 = 30^{o}$, $\xi_2 = 30^{o}$, $r_o = 1$ mm, and $h = 0$ for $\psi = 45^{o}$, 90^{o}, and 180^{o}

2.6.3.2 Effect of h

Figure 2.12 shows the shape of the needle cutting edge and inclination angle for $\xi_1 = 30^{o}$, $\xi_2 = 30^{o}$, $r_o = 1$ mm, $\psi = 135^{o}$, and $h = 0$, 1 and 2 mm. Increasing h causes Ellipses I and II to meet at γ values closer to ψ. Again Ellipse I remains fixed in place, therefore the λ remains the same for $0^{o} \leq \gamma \leq 90^{o}$. Varying h can lower the maximum λ reached by Ellipse II.

A unique effect of varying h is observed on λ, which becomes discontinuous as in the case of $h = 1.5$ and 2 mm. This occurs because the λ on one side of the needle tip is different than the λ on the opposite side of the needle tip. The cutting characteristics

change greatly at this transition point. This interesting characteristic may greatly affect the cutting performance of the needle as a whole.

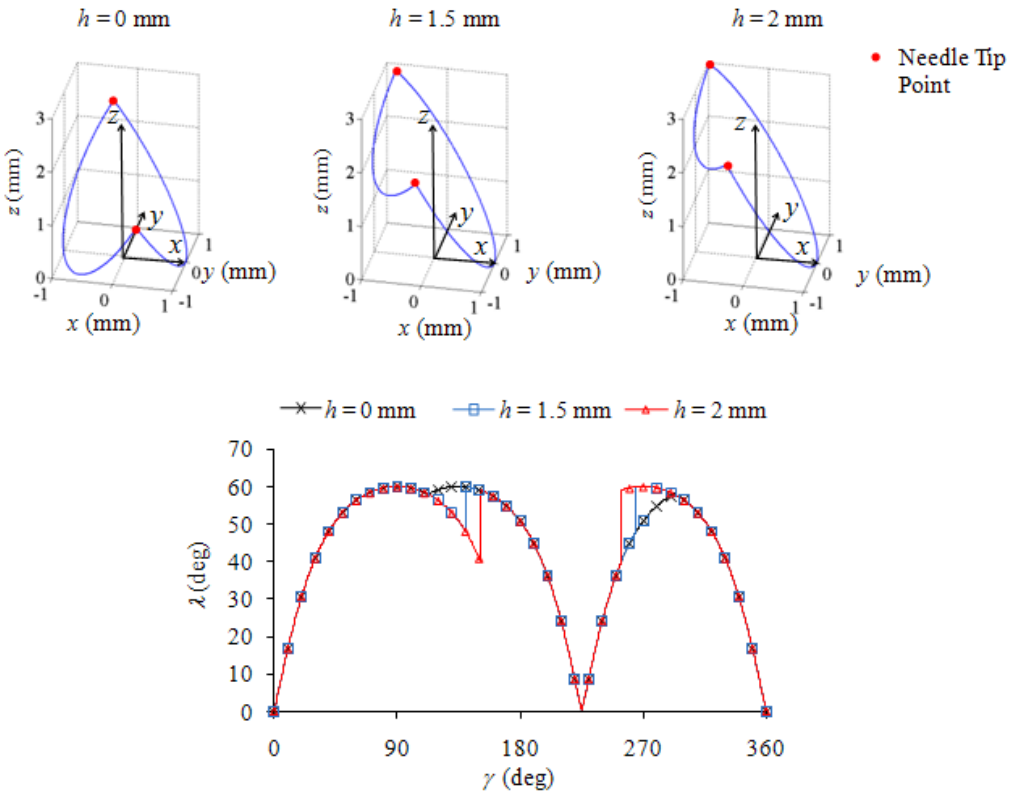

Figure 2.12: Cutting edge profile and λ when $\xi_1 = 30°$, $\xi_2 = 30°$, $r_o = 1$ mm, $\psi = 135°$ and $h = 0$, 1.5, and 2 mm

2.6.4 Plane needle comparison of the inclination angle

A bias bevel needle contains a full elliptical cutting edge profile that forms the base needle tip shape for all types of plane needles given they contain the same ξ value. Adding more planes and varying the orientation of the planes only changes how the basic elliptical cutting edge profile is sectioned together and does not change the range of λ that are possible for a given ξ value.

The maximum λ achieved by a plane needle is dictated by the plane with the smallest ξ, where $\lambda \leq 90° - \xi$ for all plane needles. This occurs because the value $90° - \xi$ marks the steepest point on the bias bevel ellipse, and therefore the point of maximum inclination. As illustrated in Fig. 9, this high λ is not reached in the case of symmetric

multi-plane needles where $P > 2$. Varying the plane orientation, such as h and ψ, can also determine if the maximum λ is equal to 90º–ξ.

The minimum λ for all plane needles is 0º and the number of times that this occurs around the needle circumference is equal to P given that $P > 1$. In the case of the one-plane bias bevel needle ($P = 1$), there are two points where $\lambda = 0°$, at the top ($\gamma = 180°$) and bottom ($\gamma = 0°$) of the elliptical cutting profile. Multi-plane needles ($P > 1$) do not contain top portions of the elliptical cutting edge profile, and instead contain one lower portion of the elliptical cutting edge profile for each plane that is used to form the needle tip. Thereby, creating the situation on mutli-plane needles where the number of points with $\lambda = 0°$ equals the number of planes.

2.7 Results of Rake Angle and Discussion for Plane Needles

Figure 2.13 shows the results of the α for a bias bevel needle with $\xi = 15º$, 30º, and 45º. The range of α is between 0 and 90º–ξ. For other types of plane needles, this statement remains true because all plane needles are based on the same basic ellipse geometry.

The maximum α values occur at $\gamma = 0º$ and 180º, top and bottom of the ellipse, with a value equal to 90º–ξ. The higher rake angle represents a sharper cutting edge and makes it easier for tissue to pass over the needle cutting surface. All plane needles contain at least one relative minimum point of the ellipse; therefore, the maximum α is 90º–ξ for all plane-needles.

The minimum α occurs at $\gamma = 90º$ and 270º, midpoints of the ellipse where the cutting edge changes from the inside to the outside of the needle, with a value of 0º. The α does not become negative because the cutting edge changes sides at the point $\alpha = 0º$. Varying P, h, and ψ can potentially raise the minimum α if the midpoint of the ellipse is not revealed thereby making the cutting edge always on the inside of the needle.

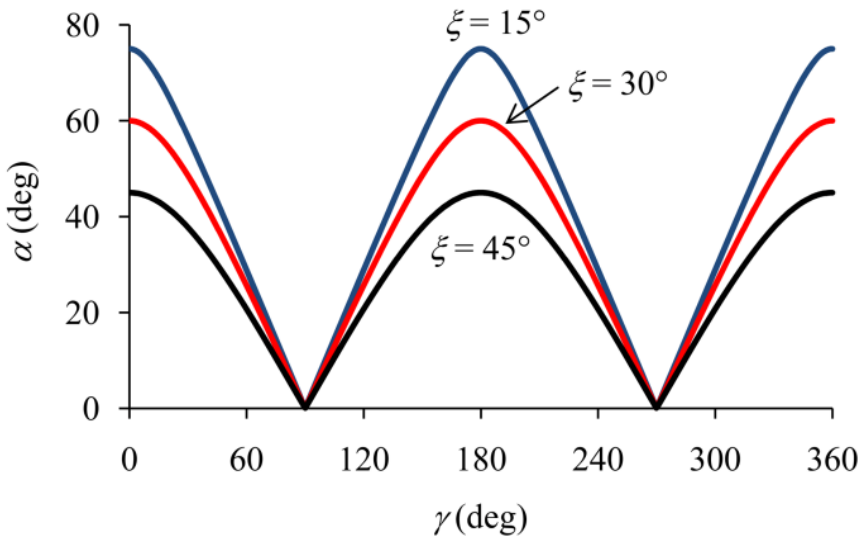

Figure 2.13: Rake angle of bias bevel needle for $\xi = 15°$, 30°, and 45°

2.8 Curved Needle Inclination Angle Results

The inclination angle of convex and concave curved surface needles are examined and compared to the traditional flat plane bias bevel needle. The inclination angles for a bias bevel, concave, and convex needle are found using Equations 2.15 and 2.16 along with the z_o values in Table 2.1.

Table 2.1: Bias Bevel, Concave, and Convex Values of z_o

Description	$z_o(\gamma)$	Variables
Bias bevel (one-plane)	$r_o\,(1 - \cos\gamma)\cot\xi$	ξ = bevel angle of the plane
Concave curved bevel	$K(r_o\cos\gamma - r_o)^2$	K = positive scale factor
Convex curved bevel	$K\,(r_o\cos(\gamma) + r_o)^2 + 4Kr_o{}^2$	

The needle tip profiles created using the z_o values in Table 2.1 are shown in Fig. 7. Concave and convex needles are formed by curved surfaces cutting through the needle tip profile with a given scaling factor K. When $K = 1$ the insertion length is 4 while when $K = 0.5$ the insertion length is 2. Therefore, a lower K value scales down the needle tip insertion length.

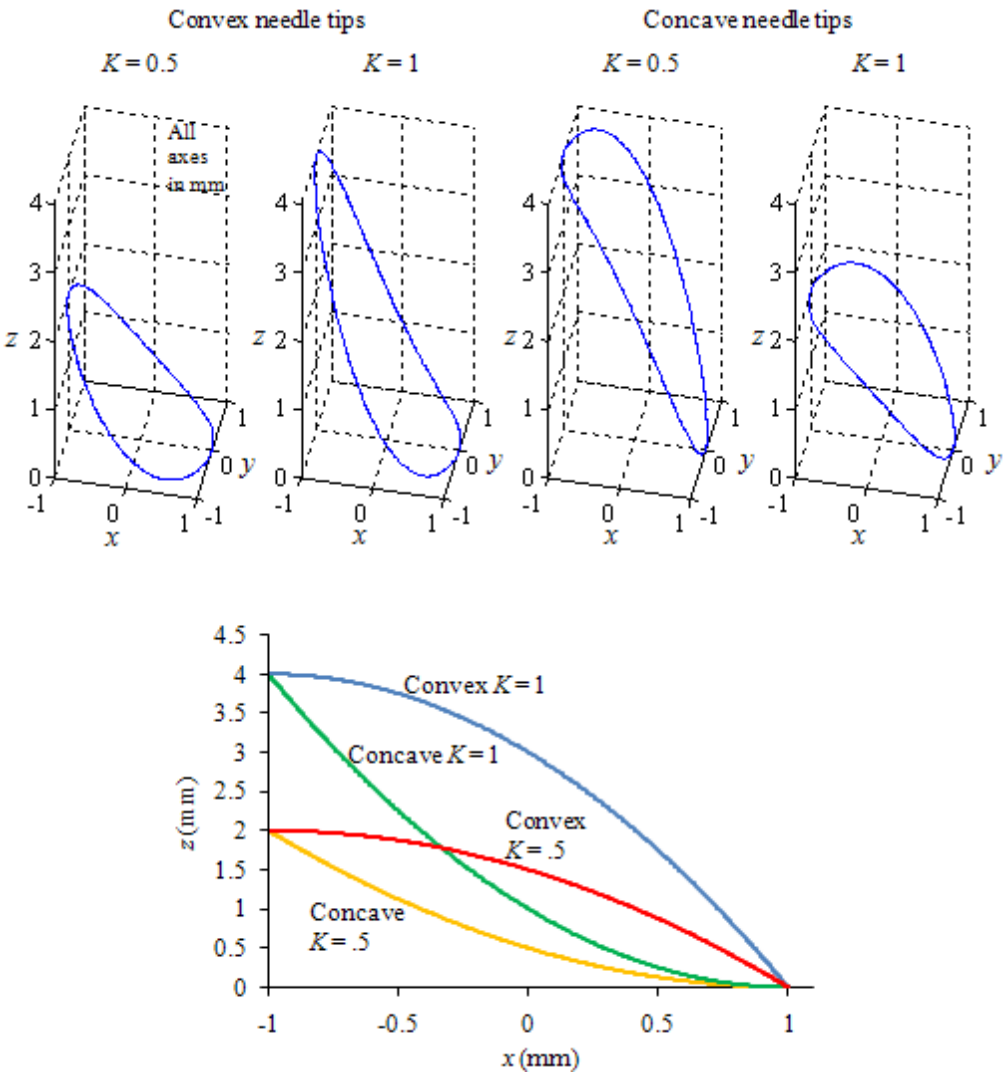

Figure 2.14: Concave and Convex needles at r_o = 1 mm, K = 1, and K = 0.5

The inclination angles of concave and convex needles for K = 1 and 0.5 on a flat plane bias bevel needle are given in Figure 2.15. It is observed that varying K scales the maximum z value down by that amount. This leads to higher inclination angles for higher K values. The inclination angle graphs for concave and convex needles are identical with a phase shift of 180º applied to the data.

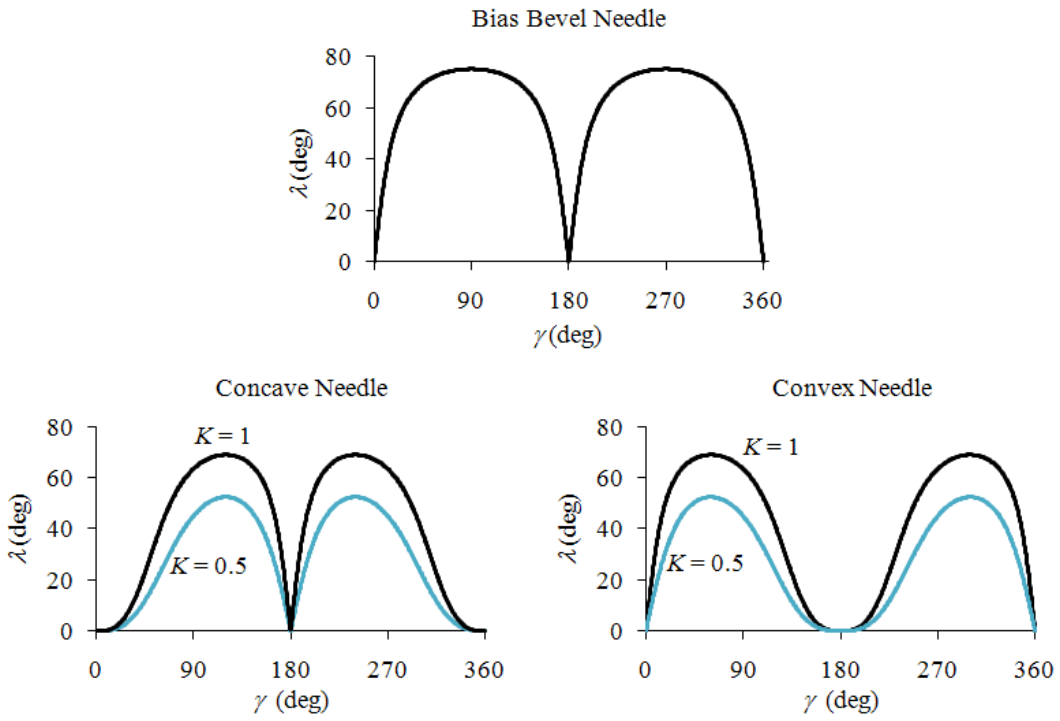

Figure 2.15: Inclination angle for concave, convex, and bias bevel needles are given r_o = 1 mm, $K = 0.5$, $K = 1$, and $\xi = 15^o$

The convex needles contain an extremely low inclination angle around $\gamma = 180^o$, whereas the concave needle's inclination angle quickly increases around $\gamma = 180^o$. The bevel needle's inclination angle profile is identical at the top and bottom of the cutting edge, whereas curved surface needles allow for differing inclination angle profiles. Therefore, the curved surface needles allow for greater flexibility in designing the inclination angle around a needle tip.

2.9 Results and Discussion of Rake Angle for Plane Needles

The rake angles of concave and convex needles are found using Equation 2.19, and results are shown in Figure 2.16. Concave and convex style needles have the same rake angle profile given a phase shift of 180º. It is shown in Figure 2.16 that higher K values create higher rake angles.

Compared to a regular bias bevel needle the curved surface needles have a drastically different rake angle profile, as shown in Figure 2.16. The curved surface

needles contain three relative maximums in rake angle which positions and magnitudes differ depending on the K value and the type of needle, concave or convex. The convex needle contains a rake angle $\alpha = 0^{\circ}$ at the top of the cutting edge ($\gamma = 180^{\circ}$) while the concave needle contains a maximum rake angle at $\gamma = 180^{\circ}$. The bias bevel needle contains identical rake angle values at the top and the bottom of the cutting edge. This symmetry creates a lack of flexibility in designing the needle tip rake angle.

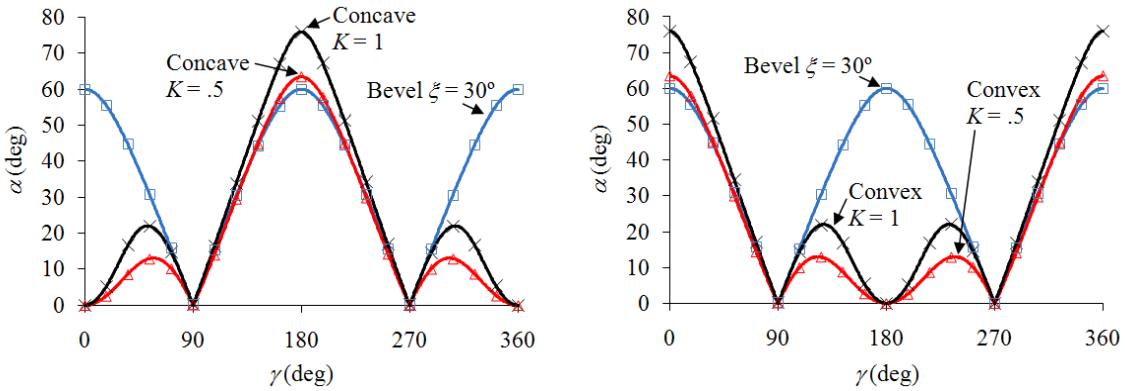

Figure 2.16: Rake angle for concave, convex, and bias bevel needles are given $K = 0.5$, $K = 1$, and $\xi = 30^{\circ}$

2.10 Insertion Length and Needle Tip Area

Figure 2.17 shows A upon needle tip insertion for 18 gauge ultra thin wall (r_i = 0.559 mm) multi-plane symmetric needles with a bevel angle of $\xi = 30^{\circ}$ and P = 1, 2, 3 and 4. L is shown in Figure 2.17 as the insertion depth at the point of complete needle tip insertion.

There is a drastic change in L and A of the needle tip depending on the number of planes used to form the symmetric needles. Higher P values lead to lower final A and L values. Biopsy performance experimentation is necessary to determine the effect A and L have on the efficiency of the needle tip cutting operation.

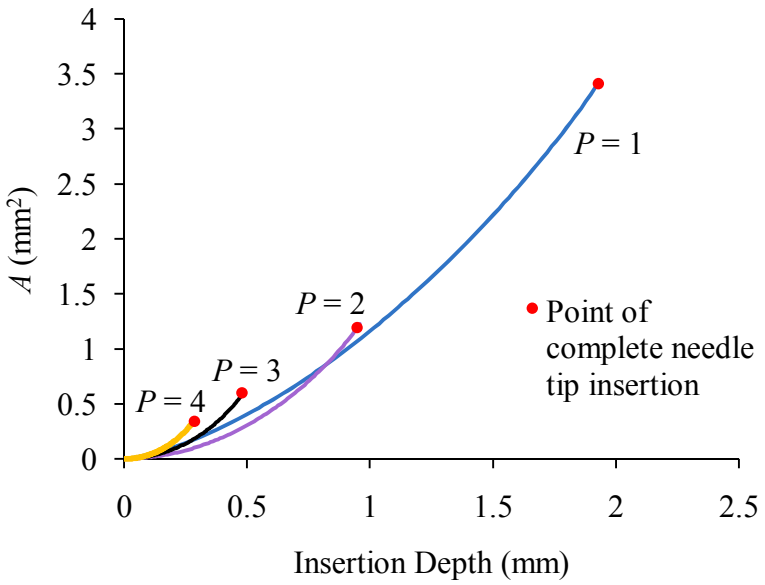

Figure 2.17: Needle insertion depth and inside area of 18 gauge (1.27 mm diameter) multi-plane symmetric needles, $\xi = 30^{\circ}$ and P = 1, 2, 3 and 4

2.11 Conclusions

The inclination angle, rake angle, cutting length of the needle (L) and the inside needle tip area (A) were examined for both flat and curved plane needles.

The three plane needle styles examined were the bias bevel, symmetric multi-plane, and non-symmetric two-plane needles. The rake angle was solved for the bias bevel needle. The maximum inclination angle achievable is dictated by ξ ($\lambda \leq 90^{\circ}-\xi$) and other variables such as h, ψ, and the number of planes could only decrease this maximum. For symmetric multi-plane needles, increasing the number of planes lowered the inclination angle. For multi-plane needles, the number of points where $\lambda = 0^{\circ}$ was equal to the number of planes used to construct the needle. Varying h and ψ shifted the needle geometry, thereby changing where the ellipses met. The rake angle for plane needles was limited by ξ ($0^{\circ} \leq \alpha \leq 90^{\circ}-\xi$). Biopsy performance experiments show that the needle tip geometry defined by inclination and rake angles directly affects biopsy performance. Longer biopsy samples are obtained for two-plane needles with higher rake and inclination angles (lower bevel angles).

Curved surface needle tips had the ability to create more variation in inclination and rake angle than traditional plane needles. Unlike the bias bevel needle the inclination and rake angles were not identical at both the top and bottom of the needle tip. This flexibility in choosing a rake and inclination angle allows for greater freedom in creating optimized needle tip geometry. The values of A and L of symmetric plane needle tips were shown to drastically vary depending on the number of planes used to create the needle tips.

In Chapter 4 the solutions to rake and inclination angles are utilized to develop a force model that predicts needle insertion force given a needles rake and inclination angle.

Chapter 3 Tissue Oblique Cutting Flow Angle and Needle Insertion Contact Length

This chapter is based on Moore et al. (2010b). The tissue oblique cutting flow angle for needle tips is experimentally determined leading to the development of three needle insertion cutting length models.

3.1 Introduction

The chip flow angle in oblique cutting has been extensively studied for metallic work-materials (Stabler 1951, Russell 1966, Luk 1972, Wen 2003, Fang 2005). The well-known and most commonly used Stabler's rule (Stabler 1951) states that, as illustrated in Figure 3.1, the chip flow angle, η, is equal to the inclination angle, λ, of the straight cutting edge in oblique cutting of metal while the rake angle, α, does not affect η. Studies have shown that slight deviations from Stabler's rule do occur; however, they are typically smaller than the scatter in measurements (Boothroyd 2006). The chip flow angle is an important parameter in machining because it determines the tool-chip contact length, l, and forces in machining.

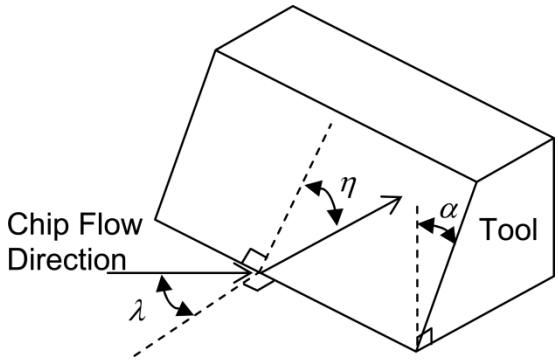

Figure 3.1: The chip flow angle (η), inclination angle (λ), and rake angle (α), of oblique cutting with straight cutting edge

For the soft, easy-deformable tissue material, Stabler's rule may not be applied directly to determine the chip flow angle. This Chapter investigates the chip flow angle in oblique cutting of tissue. A direct application of this knowledge is on the needle biopsy cutting of tissue. The chip flow angle determines the trajectory of tissue on the needle tip surface.

This Chapter first goes through experiments to observe tissue contact trajectory on two straight edge oblique cutting blades and an 11 gauge needle. Based on the observations, three mathematical models for determining contact length for needle insertion are proposed and analyzed.

3.2 Experimental Setup

The tools, machine, and work-materials are discussed in the following section.

3.2.1 Tools

Experiments are performed on two blades with straight cutting edges and one 11 gauge thin wall (TW) biopsy needle with 20° bevel angle, as shown in Figure 3.2. All three tools are made of the 316 stainless steel with no heat treatment. The thickness of the blade is 0.51 mm. Wall thickness of the needle is 0.25 mm.

The two blades, denoted as Blades 1 and 2, have defined rake and inclination angles and represent segments on the 20° bevel angle, ξ, needle cutting edge. Blade 1 has a 7° inclination angle and 70° rake angle. It represents the cutting edge parameter of the Section 1, marked on the needle in Figure 3.2. Blade 2 has a 66° inclination angle and 27° rake angle and represents the Section 2 on the needle in Figure 3.2. Both Blades 1 and 2 represent an elementary cutting tool (ECT) of the needle cutting edge.

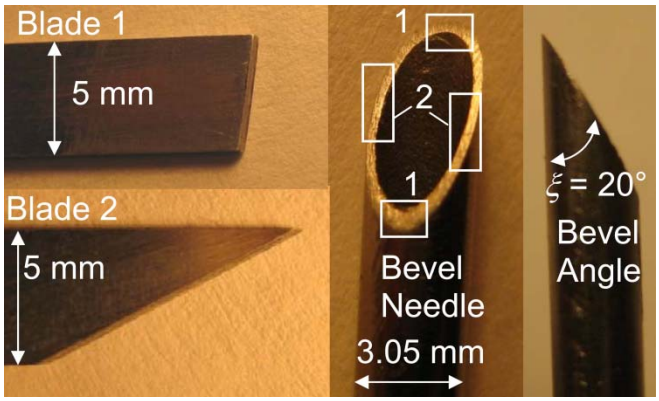

Figure 3.2: Tools used in contract length experiments: blade 1, blade 2, and bevel needle

To visually observe the trajectory of the tissue across the blades and needle and determine the chip flow angle, a spot using ink as the dye is first placed on the cutting edge of the blades and needle. During the insertion into the phantom gel and bovine liver work-materials, the spread of the dye is recorded to study the chip flow angle.

3.2.2 Needle and blade insertion machine

The experimental setup to insert a needle into the bovine liver is shown in Figure 3.3(A). In the setup, the bovine liver was constrained inside a cavity and a pneumatic cylinder exerted a constant force from the top. Work-holding is important to achieve consistent experiment results on soft work-materials, as demonstrated in the study of elastomer machining (Shih 2003). In this study, a static pressure of 15.5 kPa is applied to the top of bovine liver.

As shown in Figure 3.3(B), the phantom material is cured between two sheets of transparent acrylic plates. This allows the visual observation of the motion of the dye spot during needle and blade insertion. The bovine liver is not transparent and the needle and blade need to be retracted to see the trajectory of ink dye.

A linear stage (Siskiyou instruments 200cri) is utilized to insert the needle and blade. In this study, an insertion speed of 1.5 mm/s is used. For phantom experiments, the needle and blade travel in increments of 5 mm allowing for the dye to travel and images to be taken during insertion. For bovine liver experiments the blade and needle travel 10 mm into the tissue and then retract allowing for images to be taken before and after insertion.

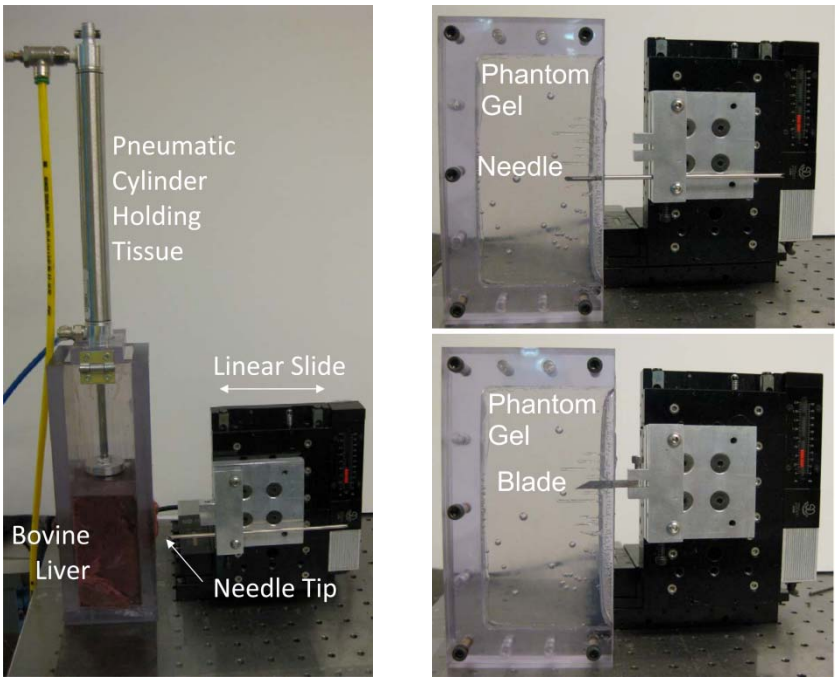

(A) (B)

Figure 3.3: (A) Overview of the setup with the bovine liver box, linear stage, and needle and (B) Phantom gel fixture with needle and a blade

3.2.3 Work material

The phantom gel is made from a 1:1 ratio of liquid plastic to plastic softener obtained from M−F Manufacturing (Ft. Worth, TX). This material is made from polyvinyl chloride (PVC) modified with plastisol to increase its softness. This material was used by Sarvazyan et al. (1998) to resemble soft tissue and provides good visibility to see the ink die through the material.

The bovine liver was fresh and precut to fit into the tissue holder box. Previous testing showed bovine liver has a Young's modulus of 3.5 kPa while the phantom gel is stiffer with a Young's modulus of 12.4 kPa (Moore 2009a).

3.3 Experimental Results

A total of eight experiments were performed, four on phantom gel and four on bovine liver. As shown in Figure 3.4 -Figure 3.6, the ink dye is placed on the tip of the blade and on two locations of the bevel needle edge. These figures show the experimental

observations for two blades inserted into phantom, the needle and blades being inserted into bovine liver, and needle being inserted into phantom, respectively.

The blade results, for both phantom (Figure 3.4) and bovine liver (Figure 3.5), show that the high inclination of blade 2, which represents the steep mid section of the needle, causes the ink to travel along the length of the cutting face of the blade. While for blade 1, which represents the front tip of the needle, the ink travels over the blade because of the high rake angle. This is about the same as predicted by Stabler's rule with low inclination angle. However, for Blade 2, the expected direction based on Stabler's rule is illustrated in Figure 3.4. The difference in directions show Stabler's rule is not applicable for soft tissue and phantom materials. The soft, compressible work-material flows along the sharp edge, as shown in Figure 3.4(B) and Figure 3.5(B).

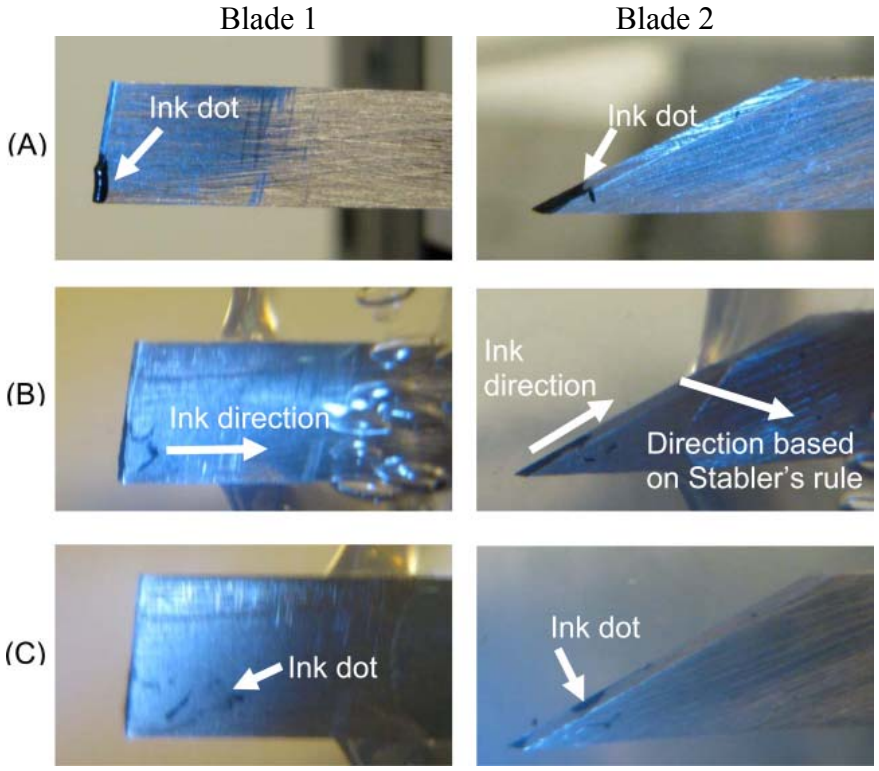

Figure 3.4: Blade insertion to phantom at depth of (A) 0 mm, (B) 5 mm, and (C) 10 mm

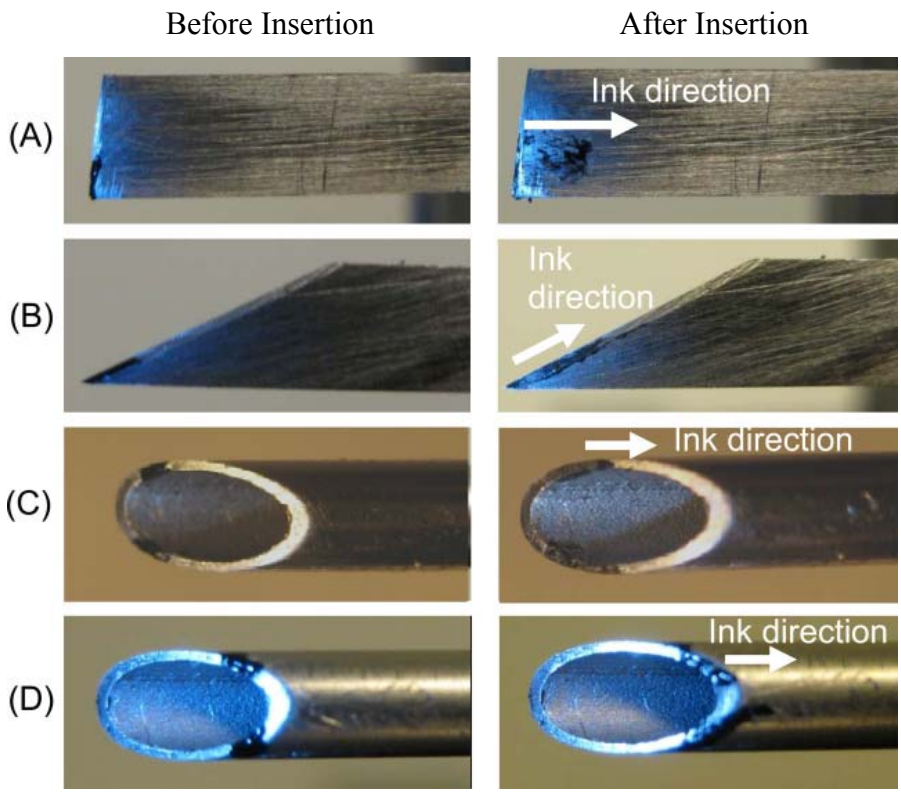

Figure 3.5: Needle and blade results for bovine liver experiments on (A) blade 1, (B) blade 2, (C) needle with ink at $\gamma = \pm 135°$, and (D) needle with ink at $\gamma = \pm 45°$

The needle results, in both the bovine liver (Figure 3.5) and phantom (Figure 3.6), reveal that when the ink dot is on the front half of needle with the peripheral angle γ equal to ±135°, the tissue flow direction is straight across the face of the needle into the inside of the needle. When the ink dot is on the back half of the needle with the peripheral angle γ equal to ±45°, the direction is straight across the needle face and the ink ends up on the outside of the needle. This differs from Stabler's rule where chip flow direction is dependent only on inclination angle. Rather, the overall needle geometry, which includes both inclination and rake angle, dictate the tissue flow direction to be along the needle face and in the plane of the needle direction.

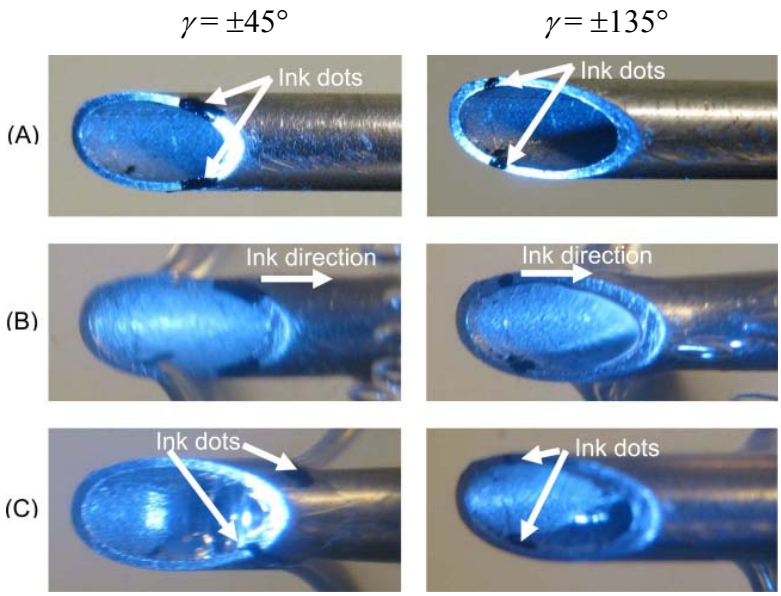

Figure 3.6: Needle phantom results when inserted to a depth of (A) 0 mm, (B) 5 mm, and (C) 10 mm

3.4 Contact Length in Needle Insertion

Based on the experimental results, a contact length model to explain tissue flow direction, l_{xz}, is developed along with two other models, l_t and l_c, which are illustrated in Figure 3.7. Figure 3.8 shows that for model l_{xz} the vector of tissue flow, $\boldsymbol{v}_c$, is at an angle $180°-\xi$ away from the cutting direction (needle axis) vector $\boldsymbol{v}_t$. This is supported by experimental observations in the preceding section. In Figure 3.7, the l_t model applies to extremely stiff tissue conditions where $\eta = 0°$. The l_c model is based on the assumption that if high vacuum suction force is applied inside the needle it will drive the tissue toward the center of the hollow needle. At $\gamma = 0°$ and $\gamma = 180°$, all three models have the same contact length, i.e., $l_{xz} = l_t = l_c$.

As shown in Figure 3.7, three models determine the tissue-needle contact length starting from the first contact point C on the cutting edge for the one-plane bias bevel needle. Point N is the opposite side along the contact length on the non-cutting edge. Given C = $\{C_x, C_y, C_z\}$ and N = $\{N_x, N_y, N_z\}$, the contact length can be found as:

$$l = \sqrt{(C_x - N_x)^2 + (C_y - N_y)^2 + (C_z - N_z)^2} \tag{3.1}$$

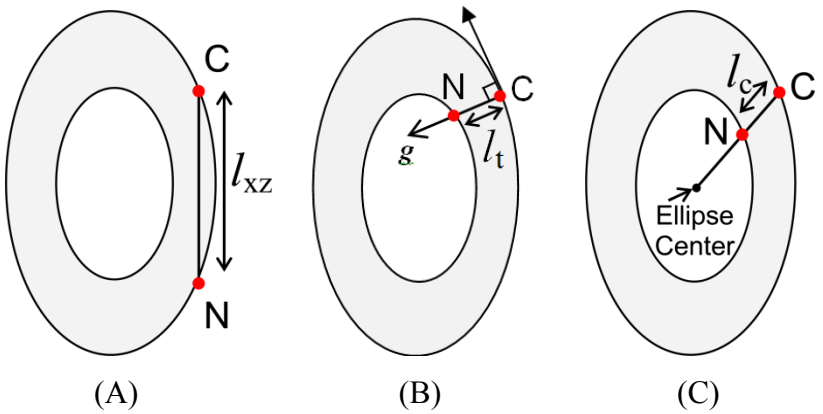

(A) (B) (C)

Figure 3.7: Bias bevel needle contact length models: (A) along the *xz* plane, (B) measured along vector ***g***, and (C) along ellipse radial line

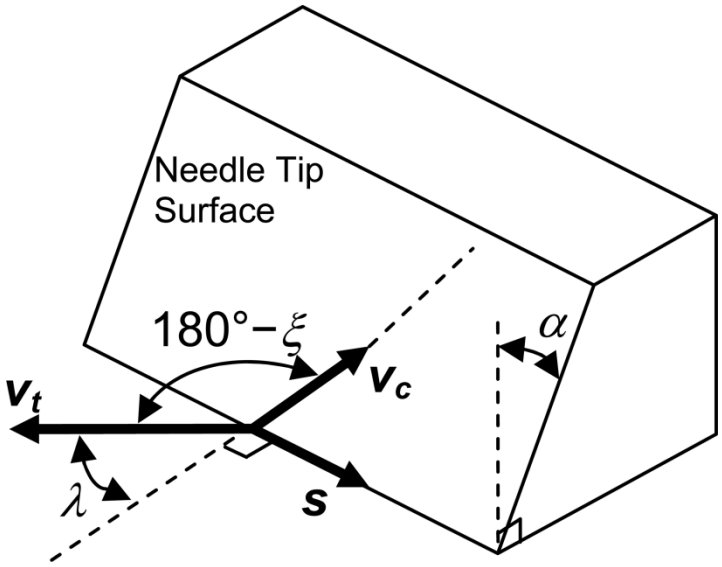

Figure 3.8: Model l_{xz} tissue flow direction based experimental observations

3.4.1 l_{xz} Contact length tissue flow model

The first step in solving for l_{xz} on a bias bevel needle is to identify Equations 3.2 and 3.3 that define both the outside and inside cutting edge, (x_o, y_o, z_o) and (x_i, y_i, z_i), respectively, given r_o is the outside needle raduis, r_i is the inside needle raduis, γ marks the radial position of points along the cutting edge, and ξ is the bevel angle of the needle, as illustrated in Figure 3.9.

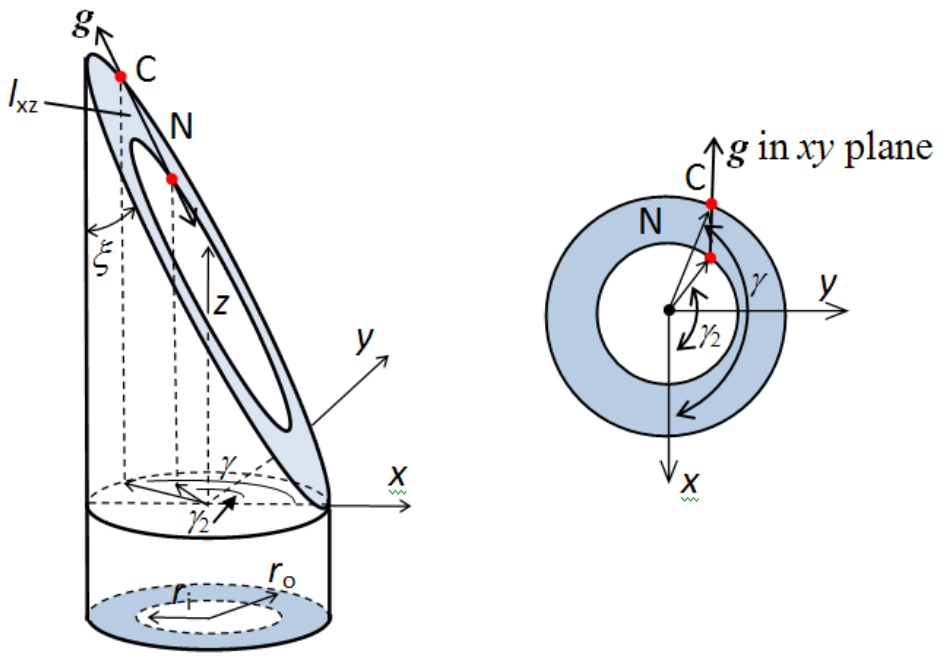

Figure 3.9: Needle diagram

$$x_o = r_o \cos\gamma$$
$$y_o = r_o \sin\gamma$$
$$z_o = r_o (1 - \cos\gamma) \cot\xi \tag{3.2}$$

$$x_i = r_i \cos\gamma$$
$$y_i = r_i \sin\gamma$$
$$z_i = r_i (1 - \cos\gamma) \cot\xi + (r_o - r_i) \cot\xi \tag{3.3}$$

To solve for l_{xz}, three different regions of the needle tip surface are examined shown in Figure 3.10 as R1, R2, and R3. R1 marks the region where there is an inside cutting edge, $-\pi/2 < \gamma < \pi/2$, R2 marks the region on the outside cutting edge where l_{xz} is bounded by the cutting edge and the outside needle raduis, $\frac{\pi}{2} < \gamma < \frac{\pi}{2} + \cos^{-1}\frac{r_i}{r_o}$, and R3 marks the region on the outside cutting edge where l_{xz} is bouned by the outside cutting edge and the inside needle raduis, $\frac{\pi}{2} + \cos^{-1}\frac{r_i}{r_o} < \gamma < \frac{3\pi}{2} - \cos^{-1}\frac{r_i}{r_o}$.

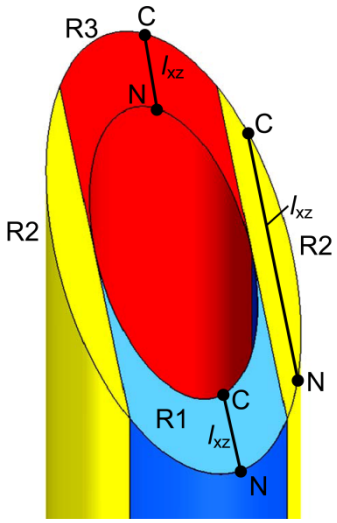

Figure 3.10: Cutting face is divided into three regions to find cutting length (l_{xz}) from point c to point n

The next step is to determine γ_2, which marks the location of the point on the non-cutting edge, point N. For R1 the *y*-components of the parametric equations that form the outside and inside cutting edge, Equations 3.2 and 3.3, are set equal to each other yielding γ_2:

$$r_i \sin\gamma = r_o \sin\gamma_2$$

$$\gamma_2 = \sin^{-1}\left(\frac{r_i}{r_o}\sin\gamma\right) \tag{3.4}$$

Similarly in region R3, γ_2 is found as:

$$r_o \sin\gamma = r_i \sin\gamma_2$$

$$\gamma_2 = \pi - \sin^{-1}\left(\frac{r_o}{r_i}\sin\gamma\right) \tag{3.5}$$

In region R2, γ_2 is on the opposite side of the *y* axis yielding:

$$\gamma_2 = \pi - \gamma \tag{3.6}$$

In region R1, C = $\{x_i(\gamma), y_i(\gamma), z_i(\gamma)\}$ and N = $\{x_o(\gamma_2), y_o(\gamma_2), z_o(\gamma_2)\}$. In region R2 and R3, point C is found as C = $\{x_o(\gamma), y_o(\gamma), z_o(\gamma)\}$. In region R2, N = $\{x_o(\gamma_2), y_o(\gamma_2), z_o(\gamma_2)\}$; while in region R3, N = $\{x_i(\gamma_2), y_i(\gamma_2), z_i(\gamma_2)\}$. With these positions Equation 3.1 can be used to find the contact lengths for model l_{xz}.

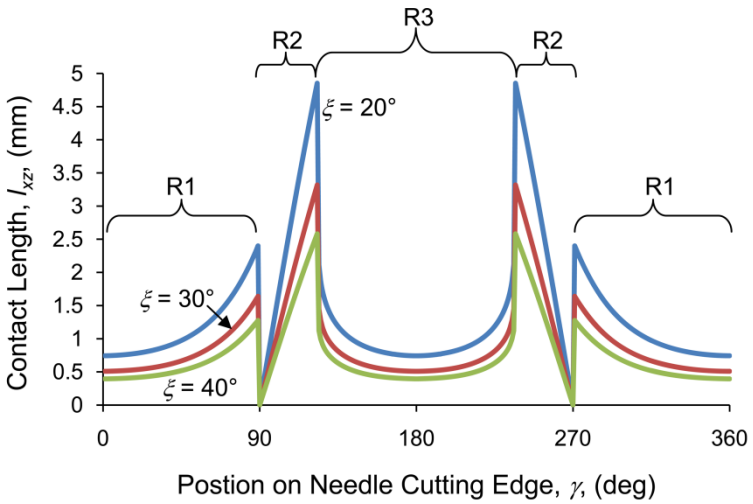

Figure 3.11: Contact length model l_{xz} for an 11 gauge thin wall needle

Figure 3.11 illustrates model l_{xz} for an 11 gauge thin wall needle (r_i = 1.27 mm and r_o = 1.524 mm) with bevel angles of 20°, 30°, and 40°. Smaller bevel angles create significantly longer contact lengths. The contact length is discontinuous between each of the regions as illustrated by the sudden change in contact length values.

3.4.2 l_t Contact length tissue flow model

In the case of model l_t vector $\boldsymbol{g}$ as marked in Figure 3.9 is perpendicular to the cutting edge of the needle. The slope of $\boldsymbol{g}$ in the xy plane for both the inside and outside cutting edges can be found as:

$$G = \frac{\cot\xi \sin\gamma \cos\xi + \sin\gamma \sin\xi}{\cos\gamma \sin\xi} = \frac{\tan\gamma}{\sin^2\xi} \tag{3.7}$$

The y-intercept of vector $\boldsymbol{g}$ projected into the xy plane differs depending if the cutting edge is on the outside (B_o) or on the inside (B_i):

$$B_o = y_o - G\,x_o = r_o(\sin\gamma - G\cos\gamma)$$
$$B_i = y_i - G\,x_i = r_i(\sin\gamma - G\cos\gamma) \tag{3.8}$$

The point where this line (vector $\boldsymbol{g}$ projected onto the xy plane) intersects the non-cutting needle edge is marked by γ_2 as point N. On the outside cutting edge, the x location of N is found by:

$$r_i = \sqrt{x_i^{\,2} + (Gx_i + B_o)^2}$$
$$x_i = \left(\frac{-GB_o \pm \sqrt{r_i^{\,2} - B_o^{\,2} + G^2 r_i^{\,2}}}{1+G^2} \right) \tag{3.9}$$

On the inside cutting edge, the x location of N is found similarly by:

$$r_o = \sqrt{x_o^{\,2} + (Gx_o + B_i)^2}$$
$$x_o = \left(\frac{-GB_i \pm \sqrt{r_o^{\,2} - B_i^{\,2} + G^2 r_o^{\,2}}}{1+G^2} \right) \tag{3.10}$$

If the cutting edge is in transition from the inside to the outside, $\gamma = \pi/2$ or $3\pi/2$, then $\gamma_2 = \gamma$.

In order for this method to work, two constraints, $0 < r_i^2 - B_o^2 + G^2 r_i^2$ and $0 < r_o^2 - B_i^2 + G^2 r_o^2$, have to be met. This statement holds true when the needle has a relatively small wall thickness. From the solution to the quadratic equations, Equations 3.9 and 3.10, two solutions are found. The solution that produces the smaller l_t value is the correct one to use in measuring the contact length.

To finish solving for γ_2, the parametric equation for the x location is used given point C is on the outside cutting edge:

$$\gamma_2 = \cos^{-1}\left(\frac{x_i}{r_i}\right) \qquad 0 < \gamma < \pi$$

$$\gamma_2 = 2\pi - \cos^{-1}\left(\frac{x_i}{r_i}\right) \qquad \pi < \gamma < 2\pi \tag{3.11}$$

If point C is on the inside cutting edge:

$$\gamma_2 = \cos^{-1}\left(\frac{x_o}{r_o}\right) \qquad 0 < \gamma < \pi$$

$$\gamma_2 = 2\pi - \cos^{-1}\left(\frac{x_o}{r_o}\right) \qquad \pi < \gamma < 2\pi \tag{3.12}$$

The coordinates of points N and C are found with γ_2 and γ, respectively. Given an outside cutting edge: N = $\{x_i(\gamma_2), y_i(\gamma_2), z_i(\gamma_2)\}$ and C = $\{x_o(\gamma), y_o(\gamma), z_o(\gamma)\}$. Given an inside cutting edge: N = $\{x_o(\gamma_2), y_o(\gamma_2), z_o(\gamma_2)\}$ and C = $\{x_i(\gamma), y_i(\gamma), z_i(\gamma)\}$. With these positions Equation 3.1 can be used to find the contact lengths for model l_t.

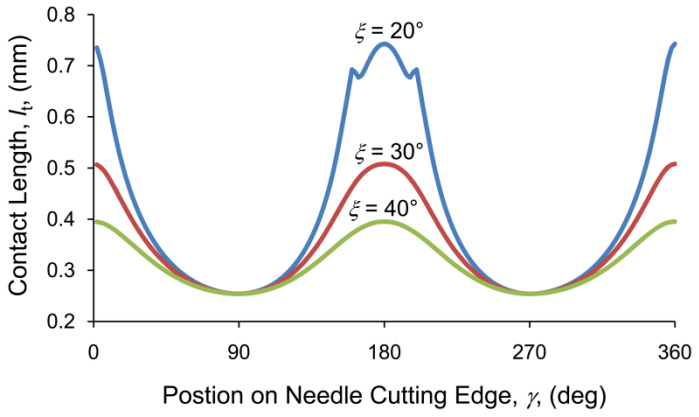

Figure 3.12: Contact length model l_t for an 11 gauge thin wall needle

Figure 3.12 illustrates model l_t for an 11 gauge thin wall needle for varying bevel angles. This model produces significantly lower contact length results than model l_{xz}. When γ is around 180° and $\xi = 20°$ there is three local maximum contact lengths. This unusual variation in contact length is caused because the tissue flow directions intersect each other when $\xi = 20°$ as shown in Figure 3.13. Because tissue is a solid these intersecting flow directions would not be possible meaning the model is not as accurate for smaller bevel angle needles such as $\xi = 20°$.

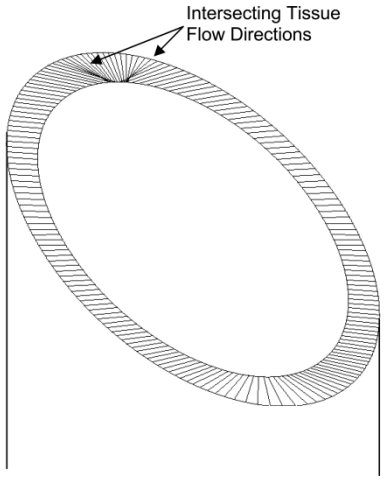

Figure 3.13: Tissue flow directions intersect in model l_t when $\xi = 20°$ for an 11 gauge thin wall needle

3.4.3 l_c Contact length tissue flow model

Model l_c is less complicated than the other two models because $\gamma = \gamma_2$, meaning the radial position of point C and point N are the same. Therefore, given an outside cutting edge N = $\{x_i(\gamma), y_i(\gamma), z_i(\gamma)\}$ and C = $\{x_o(\gamma), y_o(\gamma), z_o(\gamma)\}$. Given an inside cutting edge: N = $\{x_o(\gamma), y_o(\gamma), z_o(\gamma)\}$ and C = $\{x_i(\gamma), y_i(\gamma), z_i(\gamma)\}$. With these positions Equation 3.1 can be used to find the contact lengths for model l_c.

Figure 3.14 illustrates model l_c for an 11 gauge thin wall needle. Similar to model l_t a lower bevel angle leads to longer contact lengths. However, the models differ in that tissue flow directions will never intersect as in model l_t. This model does not produce as high of maximum contact lengths as model l_{xz}.

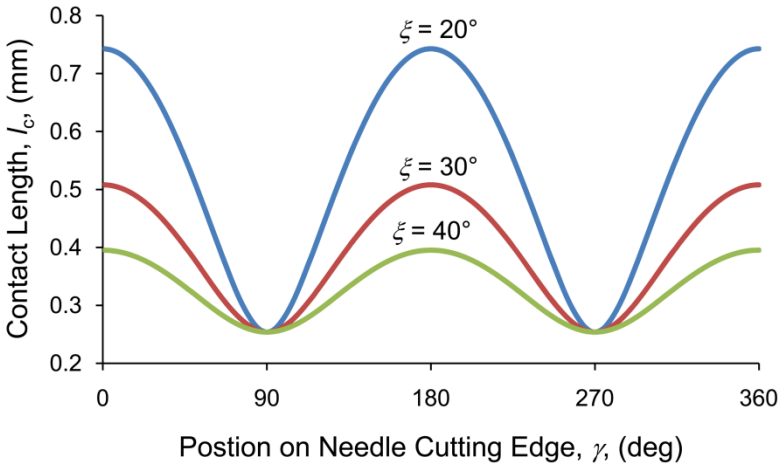

Figure 3.14: Contact length model l_c for an 11 gauge thin wall needle

3.5 Conclusions

Experimental results showed that the oblique cutting tissue flow direction was different from Stabler's rule and dependent on not only the inclination angle but also the rake angle and, for the case of needle, the bevel angle ξ. For the needle it was observed that the tissue flow followed the direction of the xz plane across the needle tip surface. A contact length model based on this observation along with two other models were proposed and analyzed.

Solving the contact length for needle geometry is a crucial step to understanding the tissue cutting process. Future studies will utilize this information to optimize needle geometry.

Chapter 4 Hollow Needle Insertion Force Model

This chapter is based on Moore et al. (2010c). A mechanistic approach using elementary cutting tool (ECT) edges of varying inclination and normal rake angles is demonstrated to be capable to predict hollow needle insertion force. A needle force model is developed and validated for the specific case of 11 gauge two-plane symmetric needles. Blades of varying inclination and rake angles are inserted into bovine liver to determine the specific force of initial tissue cutting for the given edge geometry; this information is applied to the ECT force model which is validated against experimental force results of hollow needles inserted into bovine liver.

4.1 Introduction

Mechanistic approaches for the prediction of cutting forces have been well established in machining (Ehmann 1997). One of the methods used to develop cutting force models relies on the concept of elementary cutting tool (ECT) edges (Li 2007). In this method, the force that acts on an ECT is determined. The total force that acts on the tool, in turn, is the sum of all ECT forces. The necessary requirements for implementing this approach are the availability of exact tool geometry models and experimentally determined specific cutting force values. To apply the mechanistic approach to needle tissue cutting, analytic expressions for λ and α were developed in Chapter 2 for a wide variety of needles. Using these developments as a basis, the goal of this work is to show that the mechanistic approach based on the ECT concept can be applied to study cutting forces during needle insertion into tissue. To this end, a general needle force model is proposed and then validated for the specific case of 11 gauge two-plane needles. Force insertion experiments with 16 blades of varying geometry into bovine liver are used to establish the relationship between the specific cutting force and the cutting edge angles λ and α.

Section 4.2 discusses rake and inclination angle on a two-plane symmetric needle. Section 4.3 presents the proposed mechanistic insertion force model. Section 4.4 explains the experimental setup followed by model validation results in Section 4.5.

4.2 Hollow Needle Cutting Edge Rake and Inclination Angles

Force model validation experiments are preformed on five two-plane symmetric needles of ξ = 10°, 15°, 20°, 25°, 30°. Chapter 2 previously solved for the inclination and rake angles of a two-plane symmetric needle as shown in Figure 4.1 and Figure 4.2.

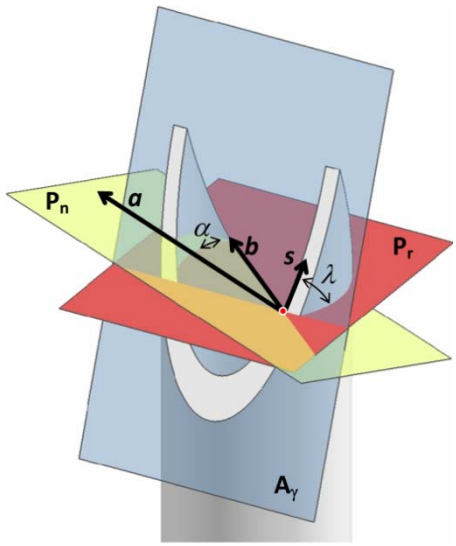

Figure 4.1: Two-plane symmetric needle diagram

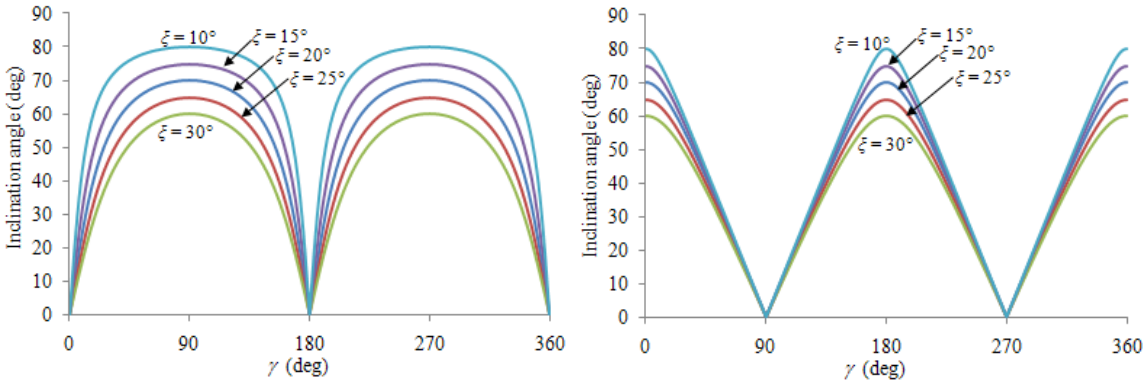

Figure 4.2: Two-plane symmetric needle rake and inclination angles

4.3 Mechanistic Approach for Cutting Force Prediction

In the context of this chapter the focus will be the determination of the initial cutting force (F_N) upon needle insertion into the tissue. This is the force that is required to initially fracture the tissue bonds and begin penetration. F_N, considering the geometric entities of the needle (Figure 4.3(a)), can be considered as the sum of two components: the cutting edge force (F_C) along the needle's inside cutting edge and the force (F_L) acting at its leading edges, i.e.:

$$F_N = F_C + F_L \tag{4.1}$$

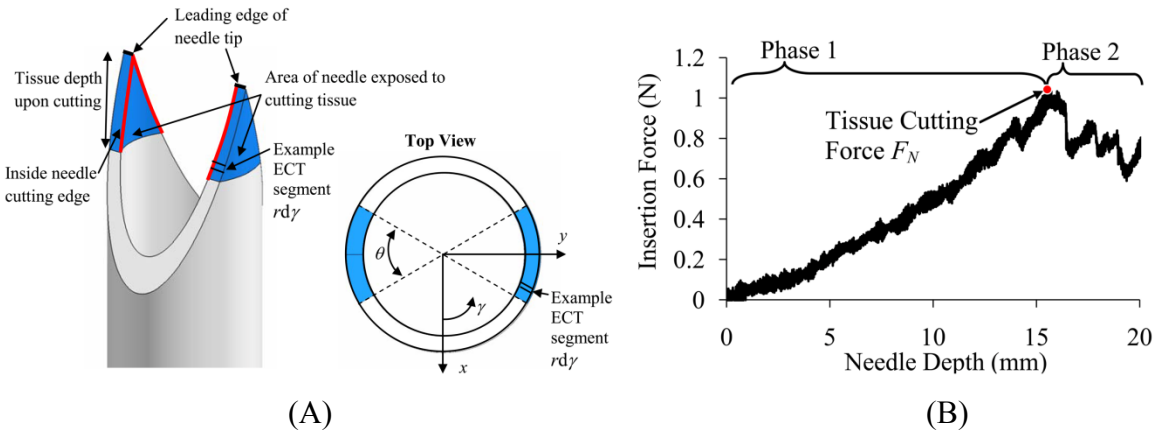

(A) (B)

Figure 4.3: (A) Leading and cutting needle edges and (B) two phases in needle force insertion into tissue

Heverly et al. (2005) have experimentally observed that there exist two distinct phases in the evolution of the tissue cutting force. In the first phase (Phase 1) the tissue deflects in the region where the cutting edge pushes on the tissue. This force increases as the tissue deflects; however, no tissue cutting occurs. The second phase (Phase 2), during which the tissue cuts, is characterized by a sudden decrease or leveling-off of the force. These two phases may repeat multiple times. The first transition between the two phases marks the force F_N. A typical insertion force profile depicting the phases is shown in Figure 4.3(B).

In the following sub-sections, based on the ECT concept, analytical expressions for the two constituent tissue cutting force components will be developed.

4.3.1 Cutting edge force - F_c

To determine F_C based on the ECT concept, the needle's cutting edge is divided into a continuous series of infinitesimal segments having a cutting width equal to $r\mathrm{d}\gamma$, as shown in Figure 4.3(A). Each $\mathrm{d}\gamma$ section of the needle contributes an infinitesimal force per cut width (specific force) that is a function of the particular segment's λ and α. In accordance with the ECT method, the specific force, $f(\lambda,\alpha)$, needs to be experimentally determined. In the current work this will be accomplished through the use of planar blades with varying λ and α. The resultant inside cutting edge force at the moment of initial tissue cutting is then calculated by integration as:

$$F_C = S\int_b^a f(\lambda,\alpha) r \, d\gamma \tag{4.2}$$

where a and b denote the range or series of ranges of γ where the needle is in contact with the tissue upon initial tissue facture, r is the radius of the cutting edge, and S is a scaling factor, to be discussed in detail in the Section 4.3.

The value of the integration limits in Equation 4.2 depends on the region of contact between the needle tip and tissue. If the needle tip is very sharp and long the tissue may cut before complete needle insertion takes place, making a and b not simply 0 to 2π radians, but instead, as illustrated by the two-plane symmetric needle in Figure 4.3(A), equal to $a = \frac{\pi+\theta}{2}$ and $b = \frac{\pi-\theta}{2}$ on one half of the needle, where θ denotes the range of contact between the needle and tissue. Due to symmetry the second half of the needle will contribute the same amount of force. Hence, for the two-plane symmetric needle the resultant force (F_C) can be found by multiplying Equation 4.2 by 2.

4.3.2 Leading edge force - F_c

The leading edge force of the needle tip (F_L) must also be considered when calculating the total force on the needle as shown in Figure 4.3(A). The λ and α of the leading edge are, λ_{Li} and α_{Li}, respectively, where i denotes the leading edge being examined, when a constant leading edge geometry is assumed which is true of almost all

needles. For example, the leading edge of a two-plane symmetric needle has the following geometry: $\lambda_L = 0°$ and $\alpha_L = \frac{\pi}{2} - \xi$ for both of its two leading edges, $i = 1$ and $i = 2$. The leading edge force is calculated as:

$$F_L = t\sum_{i=1}^{n} f(\lambda_{Li}, \alpha_{Li}) \tag{4.3}$$

where t is the thickness of the needle and $n(>0)$ is the total number of leading edges. For a variable leading edge geometry integration should be applied across the varying geometry of the needle thickness. If there are no specific leading edges, such as in the case of a one-plane needle, then $n = 0$ and therefore $F_L = 0$.

4.3.3 Initial cutting force - F_n

By combining the force components given by Equations 4.1, 4.2 and 4.3 a complete model for the determination of the initial cutting force (F_N) for any hollow biopsy needle is given by Equation 4.4 and by Equation 4.5 for the specific case of a two-plane symmetric needle, i.e.:

$$F_N = S\int_b^a f(\lambda,\alpha) r\, d\gamma + t\sum_{i=1}^{n} f(\lambda_{Li}, \alpha_{Li}) \tag{4.4}$$

$$F_N = S\int_{\frac{\pi-\theta}{2}}^{\frac{\pi+\theta}{2}} 2f(\lambda,\alpha) r\, d\gamma + 2\, t f(0,\ \frac{\pi}{2} - \xi) \tag{4.5}$$

F_N neglects the friction force between the tissue and the needle face. This value is not considered because it is small due to the small surface area of the needle's tip cutting face. The frictional forces would become much more significant when examining needle forces on a needle that is already inserted into the tissue.

4.3.4 The scaling factor *S*

The models given by Equations 4.4 and 4.5 include a scaling factor, *S,* to take into account, the differences that arise when applying the flat blade model of $f(\lambda,\alpha)$ to the

needle whose cutting edge is curved. When comparing a flat blade to a curved edge, it is observed that the blade creates less tissue deflection, Figure 4.4(A), than a needle, Figure 4.4(B), and thereby utilizes less energy and more efficiently applies force to the tissue than a needle due to its non-curved geometry. The *S* factor would vary depending on needle diameter, needle thickness, and the level of vacuum applied inside the needle. In our study the *S* factor is found using a least squares fit to experimental data in Equation 4.5.

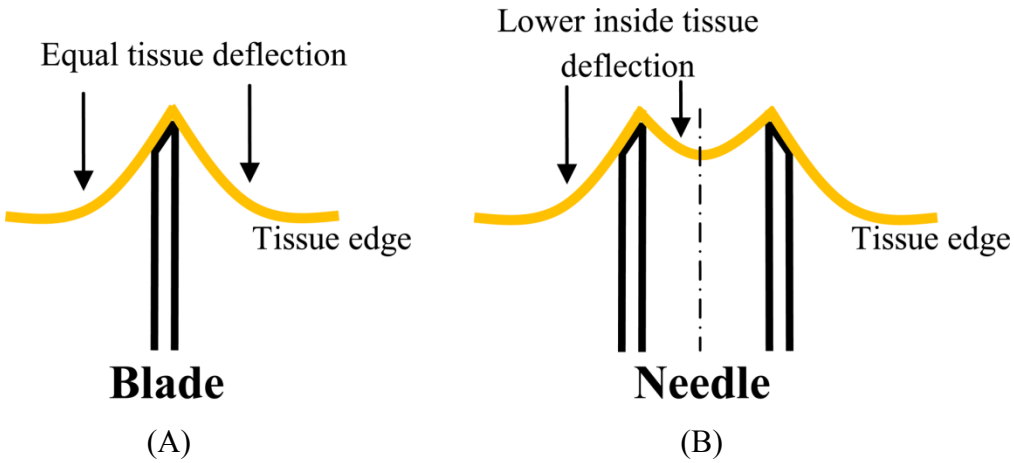

Figure 4.4: Higher tissue deviation on (A) blade than on (B) needle

4.4 Experimental Setup and Procedure

The experimental setup used to test the blades and needles, Figure 4.5, uses a Siskiyou Instrument's 200cri linear stage, a Kistler 9256A1 piezoelectric force dynamometer, and a tissue holder that, via a pneumatic cylinder, applies a constant pressure of 15.5 kPa on the tissue block to ensure consistent tissue conditions. Tissue is a very soft work material; therefore, consistent tissue holding conditions are critical to produce consistent results as demonstrated by Shih et al. (2004) in a study of elastomer machining.

The blades and needles tested had an identical thickness (t) of 0.25 mm and were made of 316 stainless steel. The contact width of the blades upon insertion was experimentally measured to determine the specific force.

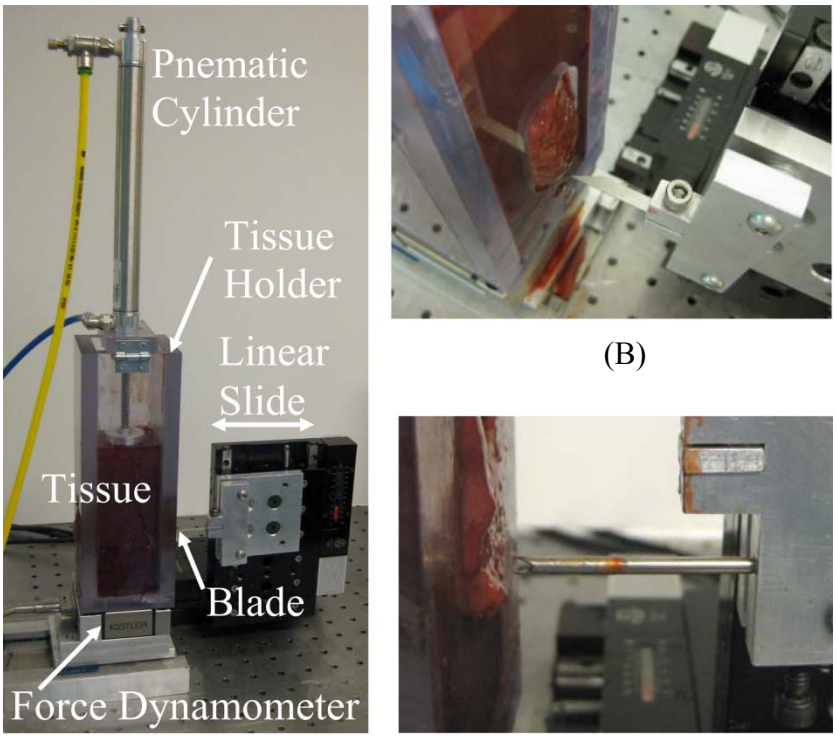

Figure 4.5: (A) Overview of the experimental setup, (B) blade cutting of bovine liver, and (C) needle insertion into bovine needle

Two sets of experiments, explained below, were performed to validate the proposed force model defined by Equation 4.5. Both experiments use force data to determine the point of initial tissue cutting, F_N.

Experiment 1: As shown in Figure 4.6, 16 flat blades were manufactured with λ and α that cover a broad range of two-plane symmetric needle geometries, i.e., $10° \leq \xi \leq 30°$ as depicted in Figure 4.7. These blades were inserted 10 times each into bovine liver and the cutting behavior was experimentally evaluated. These experiments allowed for the determination of the specific force model $f(\lambda,\alpha)$.

Experiment 2: Five 11 gauge two-plane symmetric needles with bevel angles of 10°, 15°, 20°, 25°, and 30° were each inserted into bovine liver tissue ten times, for a total of 50 trials. The depth of the needle at the point of tissue cutting was recorded to determine the relationship between θ and ξ along with the initial cutting force to validate the force model, Equation 4.5.

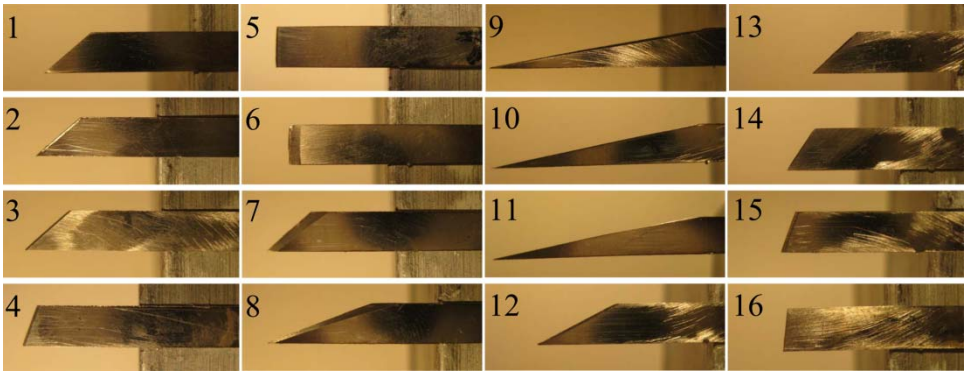

Figure 4.6: 16 blades of varying rake and inclination angles

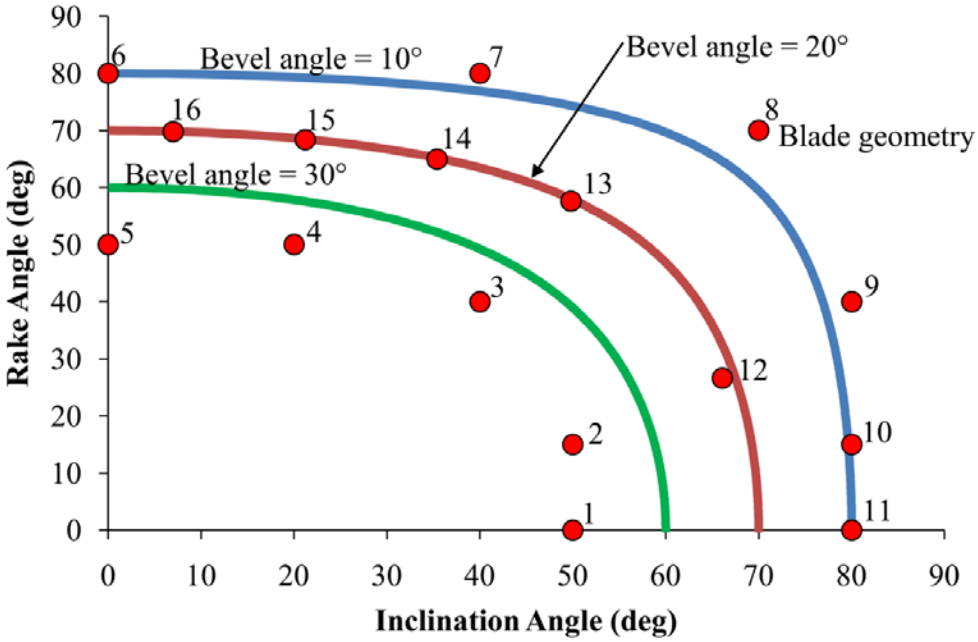

Figure 4.7: Inclination and rake angle of 16 experimental blades

4.5 Results and Discussion

Based on the two sets of experiments $f(\lambda,\alpha)$, $\theta(\xi)$, and S were determined and used to validate the force model.

4.5.1 Determination of the specific force – $f(\lambda, \alpha)$

The dots in Figure 4.8 show the average specific force calculated from the blade results in Experiment 1 for given λ and α. The surface shown in Figure 4.8 depicts $f(\lambda,\alpha)$ [N/mm] that corresponds to a 3rd order multivariable (λ and α) best fit polynomial of the data, see Equation 4.6. The coefficients were estimated using MatLab for given values of

α and λ in radians. The model fits well with an R^2 value of 0.97. The estimated $f(\lambda,\alpha)$ function is valid for needles with bevel angles between $\xi = 10°$ to $\xi = 30°$ because the blades tested were within this range.

$$f(\lambda,\alpha) = -0.042 + 0.296\lambda + 0.298\alpha - 0.255\,\lambda^2 - 0.408\,\lambda\,\alpha - 0.011\,\alpha^2 + 0.083\,\lambda^3 + 0.118\,\lambda^2\,\alpha + 0.080\lambda\,\alpha^2 - 0.059\alpha^3 \quad (4.6)$$

Figure 4.9 shows the standard deviation for the specific force results compared to λ and α with the space between the data points linearly interpolated. It is evident that there is a high variability for low λ and for a combination of low α and high λ. This information is of interest because geometries that cause high variability should be avoided in needle tip designs to maximize needle performance consistency.

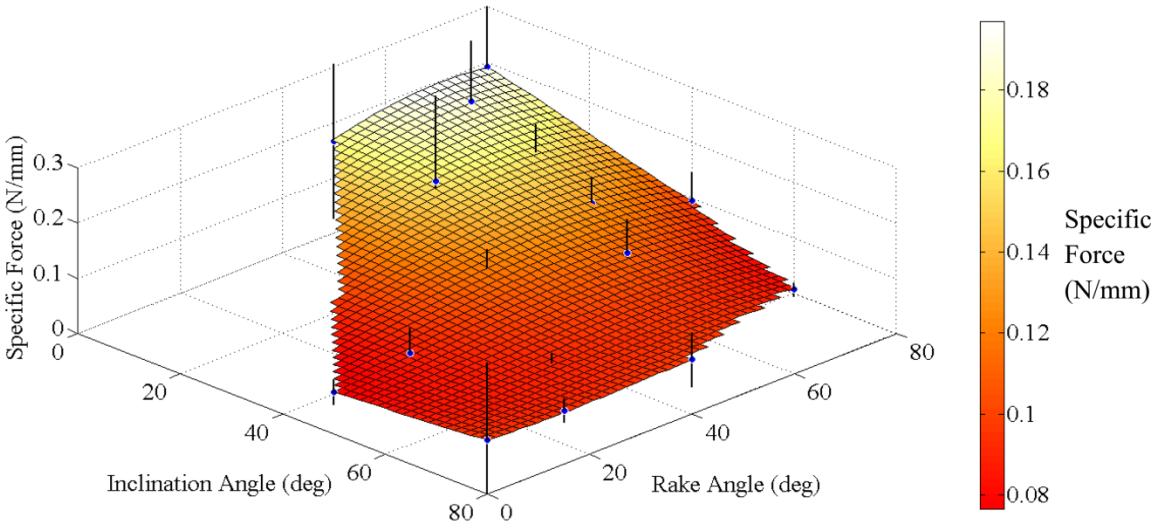

Figure 4.8: Mechanistic model from blade results, $f(\lambda, \alpha)$

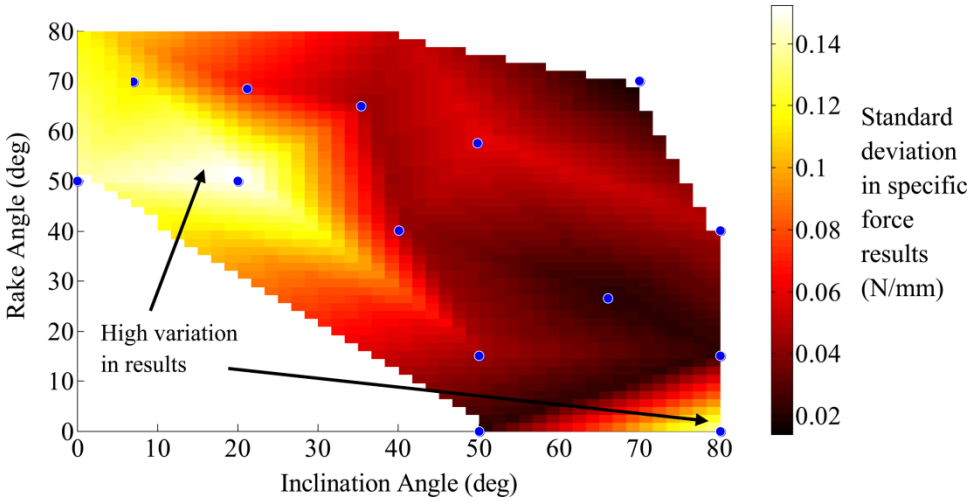

Figure 4.9: Standard deviation in blade results

4.5.2 Determination of the specific force – $\theta(\xi)$

In Experiment 2, θ was found for each of the five needles as shown in Figure 4.10. A least squares linear curve fit relationship between θ and ξ was found to be:

$$\theta = 9.2\ \xi \qquad \xi < 19.6^{o}$$
$$\theta = 180^{o} \qquad \xi > 19.6^{o} \tag{4.7}$$

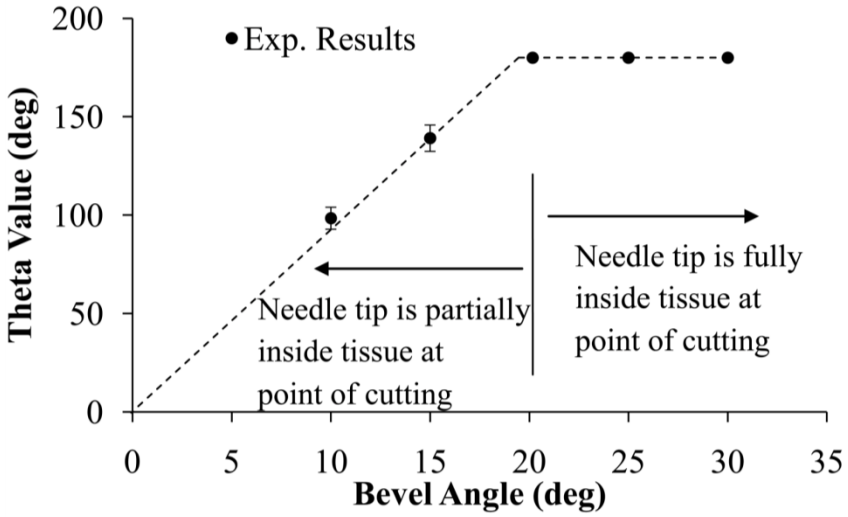

Figure 4.10: θ value measured and least squares fit model

4.5.3 Comparative assessment of predicted and experimental results

The experimentally measured average initial tissue cutting forces for the five needles are given in Figure 4.11 along with the forces predicted by the needle force model Equation 4.5 for $S = 1.00$ and 1.26 by utilizing the values that were derived for θ and $f(\lambda,\alpha)$. $S = 1.26$ was found using a least squares fit and is valid for 11 gauge thin walled needles with no vacuum applied. The model has an $R^2 = 0.979$; thereby confirming the validity of the force model for an 11 gauge needle.

In order to use the general force model expressed by Equation 4.4, both S and θ must be experimentally determined. The specific force model, $f(\lambda,\alpha)$ is valid as long as the needle geometry remains within the range of the inclination and normal rake angles of the tested ECT edges, shown in Figure 4.7.

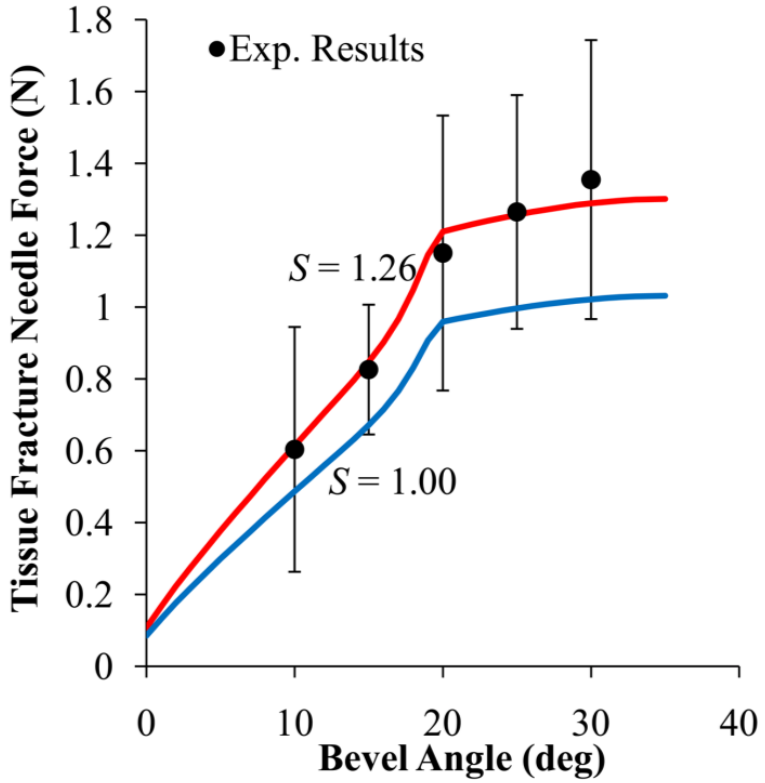

Figure 4.11: Force model compared to needle force results

4.6 Conclusions

A mechanistic approach, using the ECT concept, was used to develop a force model based on λ and α. The approach has demonstrated to accurately predict needle

insertion forces. The force model was validated based on experimental force results obtained from five 11 gauge two-plane symmetric biopsy needles thereby proving the concept of using ECTs to develop a needle tip force model. The force model provides insights into the distribution of the tissue cutting forces during needle insertion and can be used to improve needle tip designs for more efficient cutting of tissue and better biopsy outcomes.

The force model developed is shown to have an R^2 value of 0.979 when compared to the actual needle data. It was also found that cutting edges with higher λ cut tissue with lower cutting forces. Cutting edges with low λ (less than 30°) or a combination of high λ (greater than 70°) and low α (less than 10°) are demonstrated to produce a greater variation in cutting forces.

Chapter 5 Novel Needle Cutting Edge Geometry for End Cut Biopsy

This chapter is based on Moore et al. (2010d). The novel concept of the enhanced cutting edge (ECE) needle tip design is introduced, which contains high inclination angles that allow for more efficient tissue cutting. ECE and regular two-plane symmetric needle tip's biopsy performance and cutting force are compared over a series of needle insertion experiments into bovine liver under varying levels of vacuum. From these experiments the effect of vacuum on biopsy performance and force is also studied. The novel ECE needle tip design is determined to outperform the regular two-plane symmetric needle by yielding longer biopsy samples.

5.1 Introduction

A predictive force model was developed for hollow needle insertion in Chapter 4, and concluded that high λ can lower both insertion force as well as force variation. A lower insertion force represents more efficient cutting of tissue, which is essential to improve biopsy performance. This knowledge is applied in this study to design a new needle tip geometry, called enhanced cutting edge (ECE), to increase the λ along the cutting edge. The idea to increase λ on the leading cutting edge of the needle by creating a sharp needle tip point, known as a lancet point (Kucklick 2006), has been around since the patent by Huber in 1946 for hypodermic needles. The lancet point contains two extra surface planes that are ground at the one-plane bevel needle tip to increase λ on the leading needle tip point to reduce the needle insertion force. It is unlikely that Huber (1946) understood the inclination angle effect in oblique cutting of tissue. The knowledge in tissue cutting mechanics helped design the advanced ECE needle concept which targets increasing λ on the heel of the bevel cutting edge (last section of bevel needle tip that enters patient).

Some biopsy devices apply a vacuum pressure inside the hollow needle (negative internal needle pressure) to improve biopsy sample length, a common practice in many breast biopsy devices. It has been shown in breast biopsy that a 14 gauge vacuum assisted end-cut biopsy device can obtain more samples faster than with a regular 14 gauge needle device (Lehman 2004). However, quantified studies of vacuum level on end-cut biopsy performance have not been well documented.

In this study, the ECE and regular two-plane needles are evaluated for end-cut biopsy of tissue under various levels of internal needle pressure. Experiments of needle insertion into bovine liver are performed using regular and ECE 11 gauge two-plane symmetric needles. The levels of internal needle pressure tested are atmospheric 0 kPa and the vacuum gauge pressures of −68.9 and −137.8 kPa. These insertion studies compare both the initial cutting force and the biopsy sample length to distinguish the performance of the ECE vs. regular needle tip designs.

In this study the rake and inclination angles of two-plane and ECE needle tips are compared. Next a needle insertion force model is reviewed. Lastly biopsy experiments into bovine liver are conducted and the results are discussed.

5.2 Two-Plane and ECE Needle Tip Geometry

As discussed in Chapter 2 a two-plane symmetric needle, as illustrated in Figure 5.1, contains inclination angles that vary, $0 \le \lambda \le 90° - \xi$, and rake angles that vary, $0 \le \alpha \le 90° - \xi$. Results of λ and α for a two-plane needle with $\xi = 20°$ is shown in Figure 5.2. The $\lambda = 0°$ at point B_1, known as the heel of the bevel, which is marked in Figure 5.1(A) and Figure 5.2. Increasing this region's λ can improve tissue cutting efficiency and thereby allow for longer biopsy samples to be obtained.

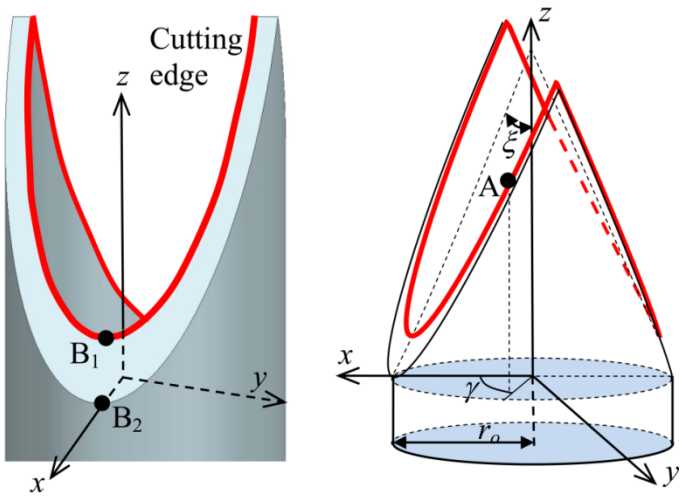

(A) (B)

Figure 5.1: (A) CAD and (B) line drawing of a regular two-plane symmetric needle defined by the bevel angle ξ

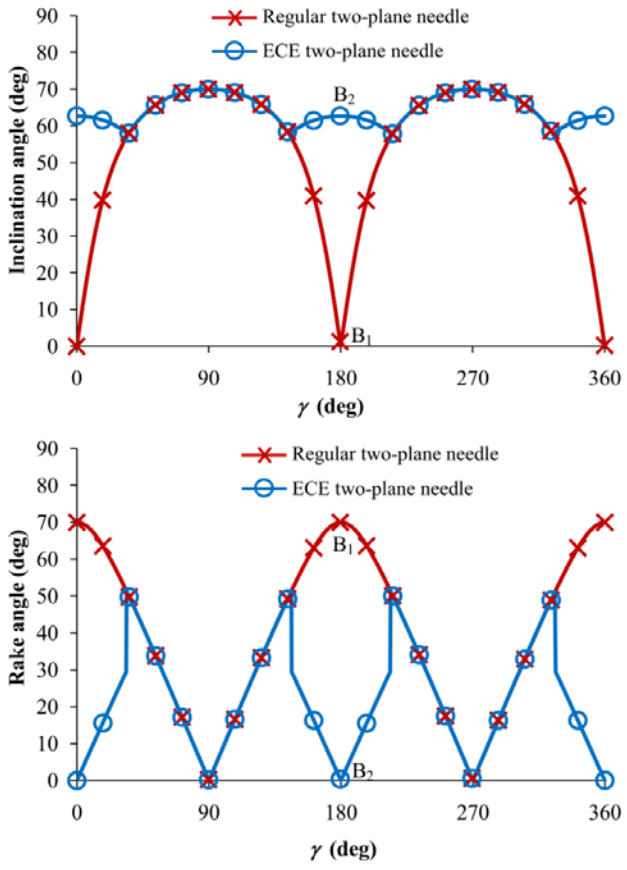

Figure 5.2: Inclination and rake angle of regular two-plane symmetric needle and ECE two-plane needle

Figure 5.3(A) shows an ECE two-plane needle that uses a wedge with angle φ to cut the angled edges into the heel of the bevel where $\lambda = 0°$, thereby eliminating this poor cutting condition found at and around B_1. The wedge removes material up to point B_2, the lowest point in the z-direction on the ground surfaces in the needle tip. The groove in the ECE needle is created using electrical discharge machining (EDM) with a wedge electrode made of graphite as shown in Figure 5.3. The cutting edge profile of the needle can be either continuous as with the example in Figure 5.3(A) or discontinuous as with Figure 5.3(B).

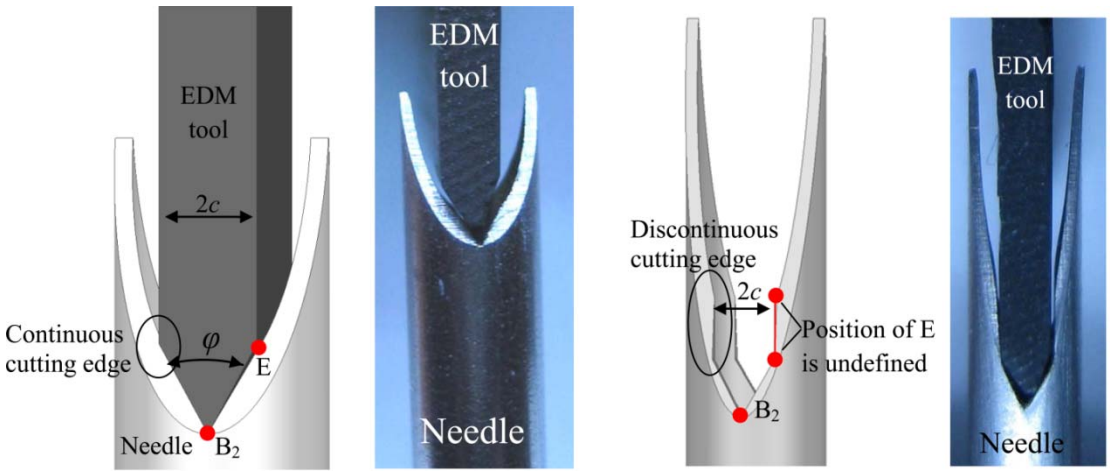

Figure 5.3: (A) ECE two-plane needle with a continuous cutting edge and (B) ECE two-plane needle with a discontinuous cutting edge

The λ and α for an ECE two-plane needle is found by dividing the needle into sections based on how the needle cutting edge geometry was created. The needle is found to contain two sections shown in Figure 5.4. Section 1 is the area where the needle cutting edge is formed by grinding two planes on the needle, Section 2 is the area where the needle cutting edge is formed by EDM cutting. The placement of the sections depends on the angle γ where the wedge takes effect, denoted as γ_e, as shown in Figure 5.4 (C). Section 1 occurs when $\gamma_e \leq \gamma \leq 180°-\gamma_e$ and $180°+\gamma_e \leq \gamma \leq 360°-\gamma_e$. Section 2

occurs when $0 \le \gamma \le \gamma_e$, $180° - \gamma_e \le \gamma \le 180° + \gamma_e$, and $360° - \gamma_e \le \gamma \le 360°$. The λ and α for the ECE needle are:

$$\text{Section 1:} \quad \lambda(\xi,\gamma) = \arcsin \frac{\left|\cot\xi \sin\gamma\right|}{\sqrt{1+\cot^2\xi \sin^2\gamma}}$$

$$\text{Section 2:} \quad \lambda(\xi,\gamma) = \arcsin \frac{\left|\cot\frac{\phi}{2}\sin\left(\gamma+\frac{\pi}{2}\right)\right|}{\sqrt{1+\cot^2\frac{\phi}{2}\sin^2\left(\gamma+\frac{\pi}{2}\right)}} \tag{5.1}$$

$$\text{Section 1:} \quad \alpha = \arccos\sqrt{\cos^2\gamma \sin^2\xi + \sin^2\gamma}$$

$$\text{Section 2:} \quad \alpha = \arccos\sqrt{\cos^2\left(\gamma+\frac{\pi}{2}\right)\sin^2\frac{\phi}{2} + \sin^2\left(\gamma+\frac{\pi}{2}\right)} \tag{5.2}$$

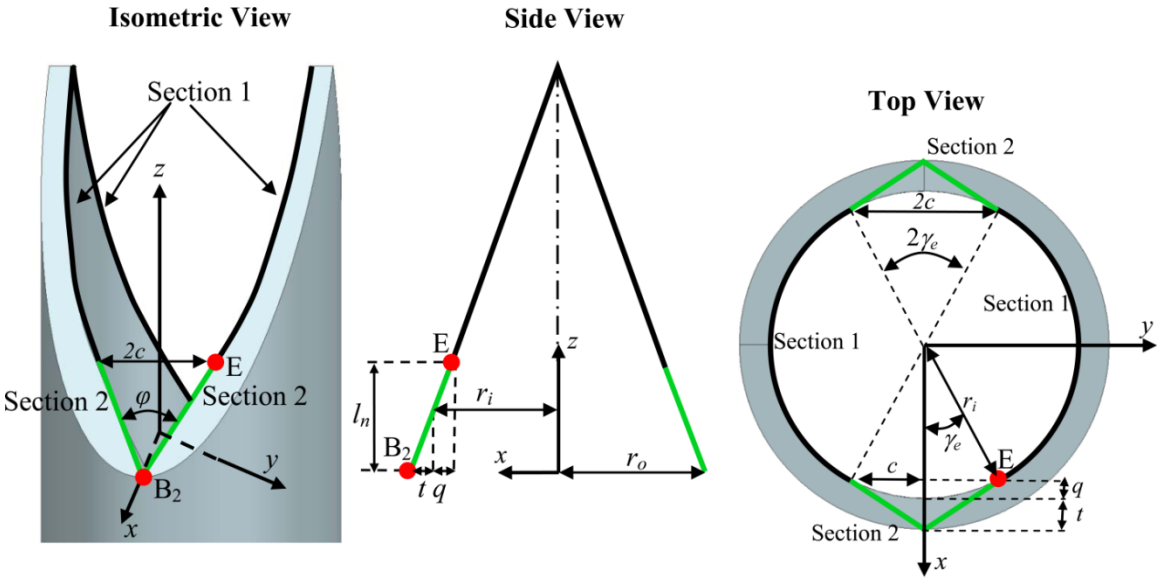

(A) (B) (C)

Figure 5.4: ECE two-plane needle in (A) isometric view (B) side view, and (C) top view

Figure 5.2 illustrates the λ and α for an ECE two-plane needle tip with $\xi = 20°$ and $\varphi = 57.5°$. The ECE two-plane needle at point B_2 has $\lambda = 90° - \varphi/2$ as compared to $\lambda = 0°$ of point B_1 on a regular two-plane needle.

For the continuous cutting edge ECE two-plane needle configuration in Figure 5.3(A), the angles of φ, γ_e , and ξ are all related where point E at $\gamma = \gamma_e$ is continuous. The distance from B_2 to E in the z-direction, is l_n, as shown in Figure 5.4(B) and solved as:

$$l_n = (t + q)\cot\xi \tag{5.3}$$

where t is the needle wall thickness and q is the distance in the x-direction when $y = 0$ from the inside needle wall to E as shown in Figure 5.4(B) and (C). The length q can be put in terms of γ_e and r_i, the inside radius of the needle, as:

$$q = r_i(1 - \cos\gamma_e) \tag{5.4}$$

The width of the top of the wedge is equal to $2c$, as shown in Figure 5.3(A), Figure 5.4 (A), and Figure 5.4(C), and c is:

$$c = l_n\tan(\varphi/2) = r_i \sin\gamma_e \tag{5.5}$$

Combining Equations 5.3 to 5.5 gives the relationship among φ, γ_e, and ξ.

$$\cot\xi \tan(\varphi/2)\,(t + r_i - r_i \cos\gamma_e) = r_i \sin\gamma_e \tag{5.6}$$

Using trigonometric identities and the quadratic equation, this equation is solved in terms of γ_e as:

$$\gamma_e = 2\tan^{-1}\left(\frac{1 - \sqrt{1 - \tan^2\left(\frac{\varphi}{2}\right)\cot^2(\xi)\left(\frac{t^2 + 2tr_i}{r_i^2}\right)}}{\tan\left(\frac{\varphi}{2}\right)\cot(\xi)\frac{t + 2r_i}{r_i}}\right) \tag{5.7}$$

If Equation 5.7 produces an imaginary solution to γ_e then the cutting edge must be discontinuous. In the case that the cutting edge of Section 1 is tangent to the cutting edge of Section 2, the square root in Equation 5.7 equals 0 with the given parameters of t, r_i, φ, and ξ.

The needle cutting edge is discontinuous when point E is discontinuous at $\gamma = \gamma_e$, as in the example in Figure 5.3(B). In this situation the values of φ, ξ, and γ_e are independent of each other and Equation 5.7 does not apply. The geometry of a discontinuous ECE two-plane needle is defined by φ, ξ, and c. While the geometry of a continuous ECE two-plane needle is defined by φ and ξ.

5.3 Experimentation

5.3.1 Setup for needle insertion experiments

The overview and close-up view of the experimental setup to perform the needle insertion experiments is shown in Figure 5.5. As in Chapter 4 the experimental setup uses a Siskiyou Instrument's 200cri linear stage, a Kistler 9256A1 piezoelectric force dynamometer, and a tissue holder that, via a pneumatic cylinder, applies a static pressure of 15.5 kPa on the top of the bovine liver tissue block to ensure consistent tissue conditions. The needles were inserted at a rate of 1.5 mm/s through 50 mm length of tissue. Faster insertion speed experiments were conducted and are given in Appendix B. A vacuum pump is used to supply a constant vacuum pressure to the inside of the needle for the experiments using the vacuum gauge pressures of −68.9 and −137.8 kPa. After each needle insertion, the sample was then extracted using a solid rod and biopsy length was measured.

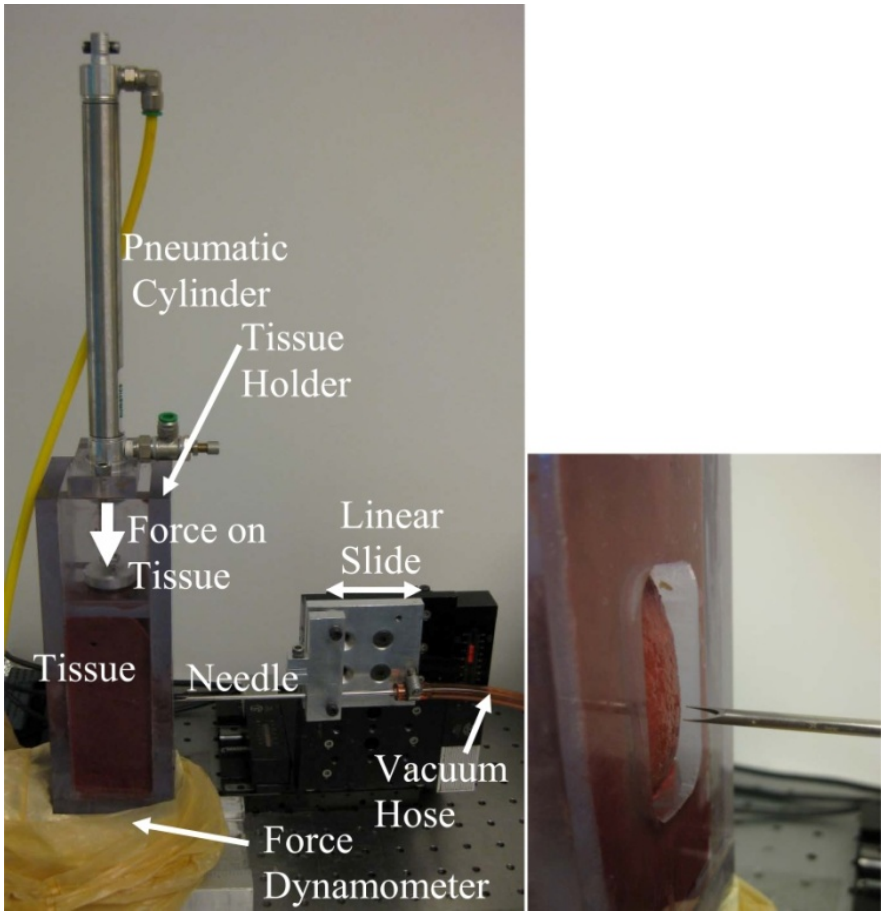

Figure 5.5: Experimental setup for needle insertion into bovine liver

5.3.2 Needles

A total of 10 needles were manufactured as shown in Figure 5.6; five regular two-plane needles and five ECE two-plane needles both having bevel angles ξ of 10°, 15°, 20°, 25°, and 30°. All the ECE two-plane needles are machined with the angle φ = 57.5°. This angle is used because for ξ = 20°, the wedge cutting edge will be tangent to the inside cutting edge. Given this angle for the ECE needles of ξ = 15° and ξ = 10°, Section 1 will be discontinuous as shown previously in Figure 5.3(B). The c value for needles ξ = 10° and 15° are all 0.69 mm because the graphite EDM milling tool used to make the needles has a width, $2c$, of 1.38 mm. The needles are 11 gauge thin walled 316 stainless steel needles (OD 3.05 mm and ID 2.54 mm).

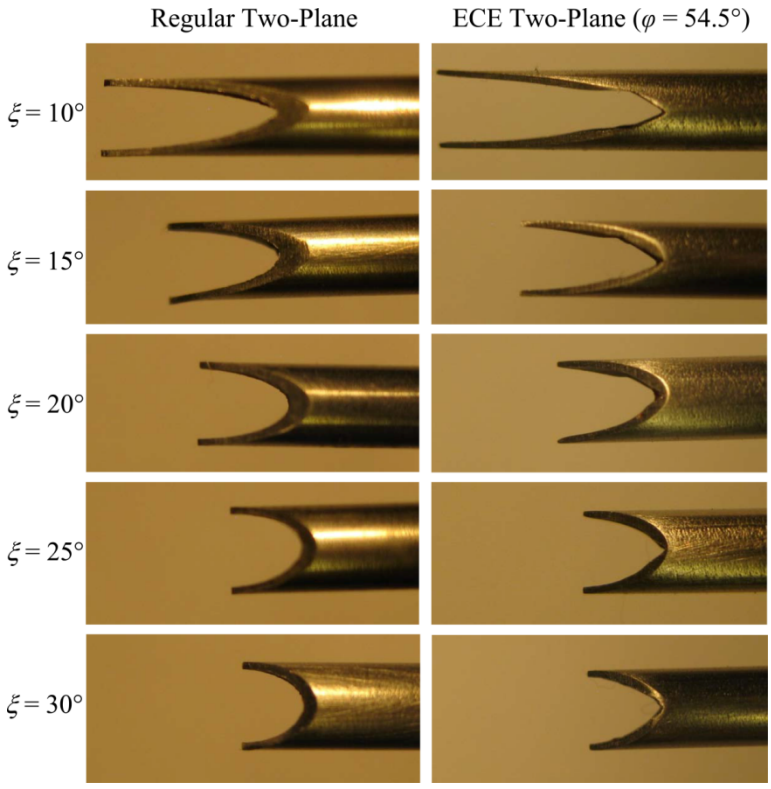

Figure 5.6: Regular two-plane symmetric and ECE needles used for experiments

5.3.3 Determination of initial tissue cutting force from the experiments

The force model previously described in Chapter 4 examines the force, F_N, when the tissue is initially cut. An example force graph of an ECE needle being inserted into bovine liver is shown in Figure 5.7. There are two phases observed; the initial Phase 1 where the tissue deflects and force increases but no physical tissue cutting occurs, and Phase 2 where the tissue is cut and the force suddenly drops or levels off. There can be multiple iterations of Phase 1 and Phase 2 in a needle insertion process. The first transition between Phase 1 and Phase 2 marks the initial cutting force F_N. The experimental force data from all the experiments are examined in this way to determine F_N.

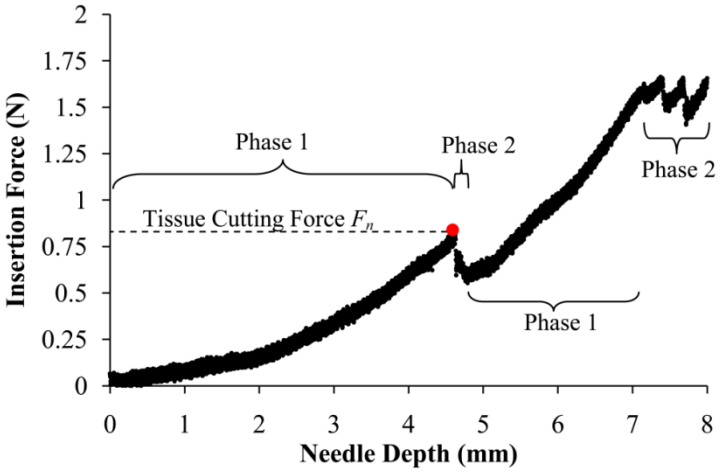

Figure 5.7: Tissue cutting force example in ECE needle of $\xi = 20°$

5.3.4 Summary of experimental procedure

In summary, this study uses five regular two-plane needles and five ECE two-plane needles (both having $\xi = 10°$, 15°, 20°, 25°, and 30°). The ECE needles are tested at the pressures of 0, −68.9, and −137.8 kPa. The regular two-plane needles are tested at the pressures of −68.9, and −137.8 kPa. Needle insertion is performed for each needle and pressure level 10 times upon which both insertion force and biopsy length are measured for a total of 250 needle insertions. Results from Chapter 4 for five regular two-plane needles with the same ξ = 10°, 15°, 20°, 25°, and 30° at 0 kPa pressure were included for analysis.

5.4 Results and Analysis

Biopsy length and force results are discussed in the following two sections.

5.4.1 Biopsy length

5.4.1.1 Needle Geometry Effect

The ECE needle produces longer biopsy results than the regular needle. As illustrated in Figure 5.8, the biopsy sample length is on average 22%, 30%, and 49% longer for ECE needles compared to that of regular needles for the internal pressures of 0, −68.9, and −137.8 kPa, respectively. This demonstrates that the ECE concept by modifying the needle to increase inclination angle on cutting edge is beneficial for end-

cut biopsy. The higher inclination angles allow for more efficient needle tip cutting of tissue and, therefore, longer biopsy samples.

Lower bevel angles result in longer biopsy lengths for both ECE and regular two-plane needles. The lower bevel angles contain higher average inclination angles that allow for more efficient biopsy cutting. The effect of vacuum is not easily distinguished in Figure 5.8; therefore, Figure 5.9 is created by rearranging the biopsy length data to compare the three vacuum levels.

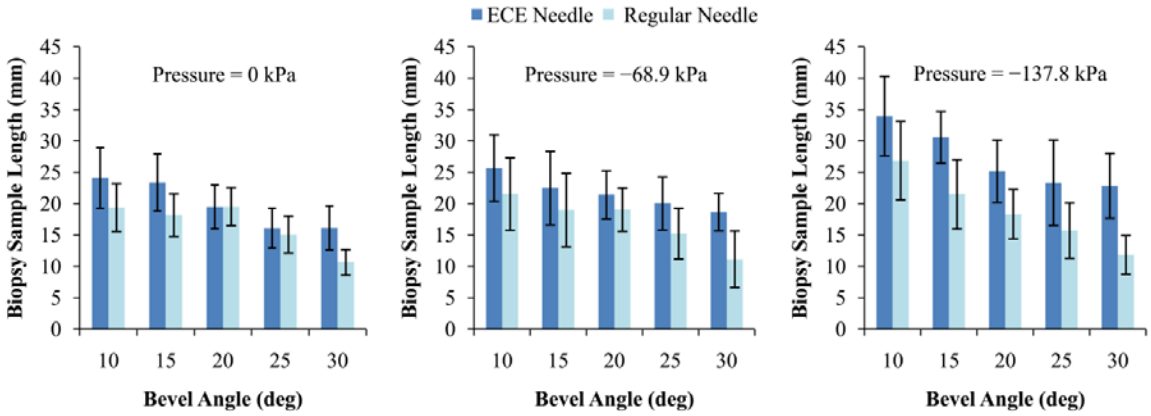

Figure 5.8: Biopsy sample length comparing ECE two-plane needle to regular two-plane needle

5.4.1.2 Vacuum Effect

For regular two-plane needles shown in Figure 5.9(A), the use of vacuum improves biopsy length for of $\xi = 10°$ and 15° but shows no effect for $\xi = 20°$, 25° and 30°. The low inclination angles in the regular needles of $\xi = 20°$, 25° and 30° make them inefficient at cutting tissue. The vacuum is only beneficial to biopsy length if the needle tip is efficiently cutting. If the needle tip can efficiently cut tissue then the tissue sample that enters the needle can be pulled into the needle by the vacuum force which acts to overcome the internal needle friction as shown in Figure 5.10. If the needle is unable to effectively cut tissue then the tissue sample does not effectively enter the needle preventing the vacuum force from benefitting the biopsy yield.

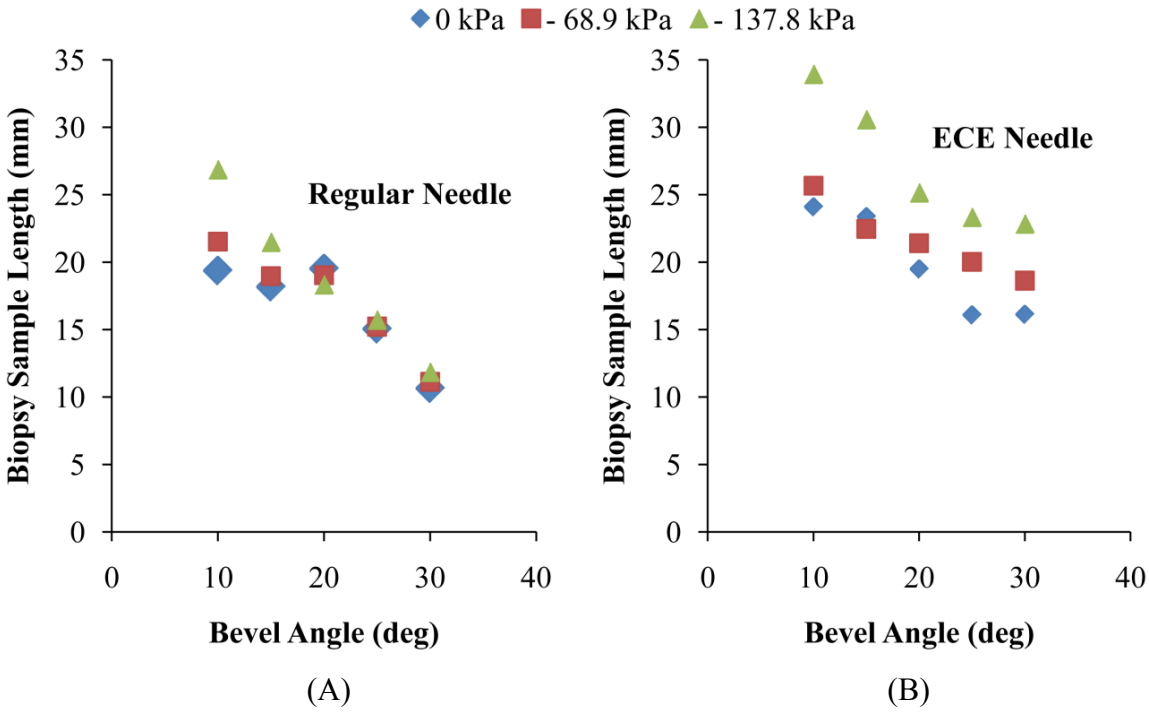

Figure 5.9: Biopsy sample length comparing pressure effect for (a) Regular and (b) ECE two-plane

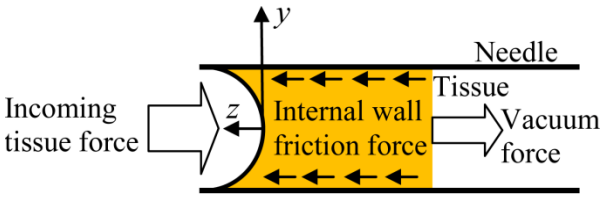

Figure 5.10: Internal wall friction force repels the motion of the incoming tissue while the vacuum force helps to pull the sample into the needle

For ECE needles the vacuum level of –137.8 kPa produces on average biopsy lengths that are 41, 31, 29, 45, and 42% longer compared to no vacuum for $\xi = 10°$, 15°, 20°, 25°, and 30° respectively as illustrated in Figure 5.9(B). The vacuum is proven to be beneficial for ECE needles which are efficient at cutting tissue due to their high average inclination angle. The use of ECE needles combined with vacuum is shown to greatly improve biopsy sample length over regular needles without vacuum.

5.4.2 Biopsy force

5.4.2.1 Needle Geometry Effect

The ECE needle produces lower needle insertion forces than regular needles for ξ = 20°, 25°, and 30° as shown in Figure 5.11. The initial insertion force is on average 20%, 9%, and 5% higher for regular compared to ECE two-plane needles for the internal needle pressures of 0, −68.9, and −137.8 kPa, respectively, on the needles of ξ = 20°, 25°, and 30°. The needles of ξ = 10° and ξ = 15° show little change because the ECE needle geometry differs from the regular two-plane needle only at the far back of the needle tip and the initial tissue cutting occurs at the front of the needle tip when ξ = 10° and 15°. This lower force for higher inclination angles corresponds to previous findings in Chapter 4.

For both ECE and regular two-plane needles lower bevel angles result in lower biopsy insertion forces. Therefore, less force is required to cut tissue when using needles containing higher inclination angles.

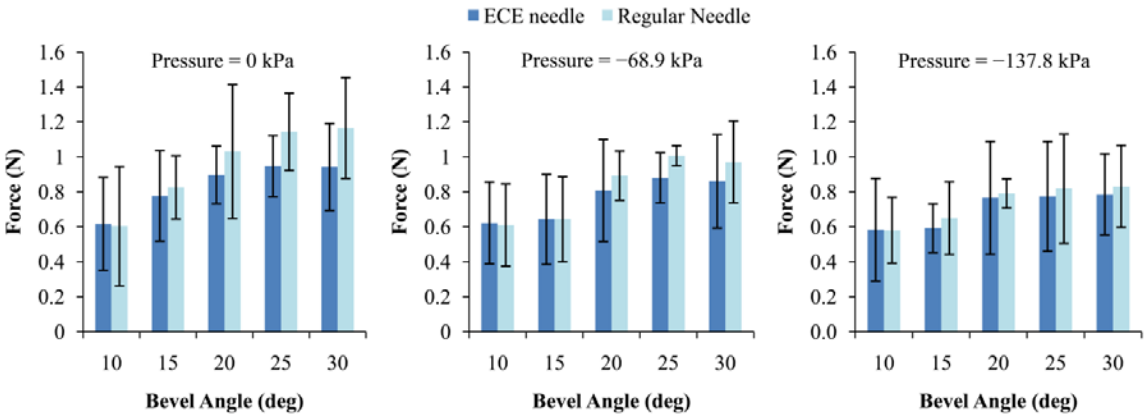

Figure 5.11: Needle insertion force comparing ECE two-plane needle to regular two-plane needle

5.4.2.2 Vacuum Effect

Vacuum lowers the average insertion force for both the regular and ECE two-plane needles of ξ = 15°, 20°, 25°, and 30° as illustrated in Figure 5.12(A) and (B) respectively. The needle applies a specific amount of force to the tissue in order to cut. When vacuum is used the vacuum force helps to apply the force necessary to cut the

tissue which leads to lower insertion forces. For the needles of $\xi = 10°$ the vacuum level appears to have little effect on the insertion force. This happens because the initial tissue cutting occurs at the very front of the needle $\xi = 10°$. In this configuration the vacuum is unable to apply a vacuum force on the tissue because mostly air is being pulled into the needle.

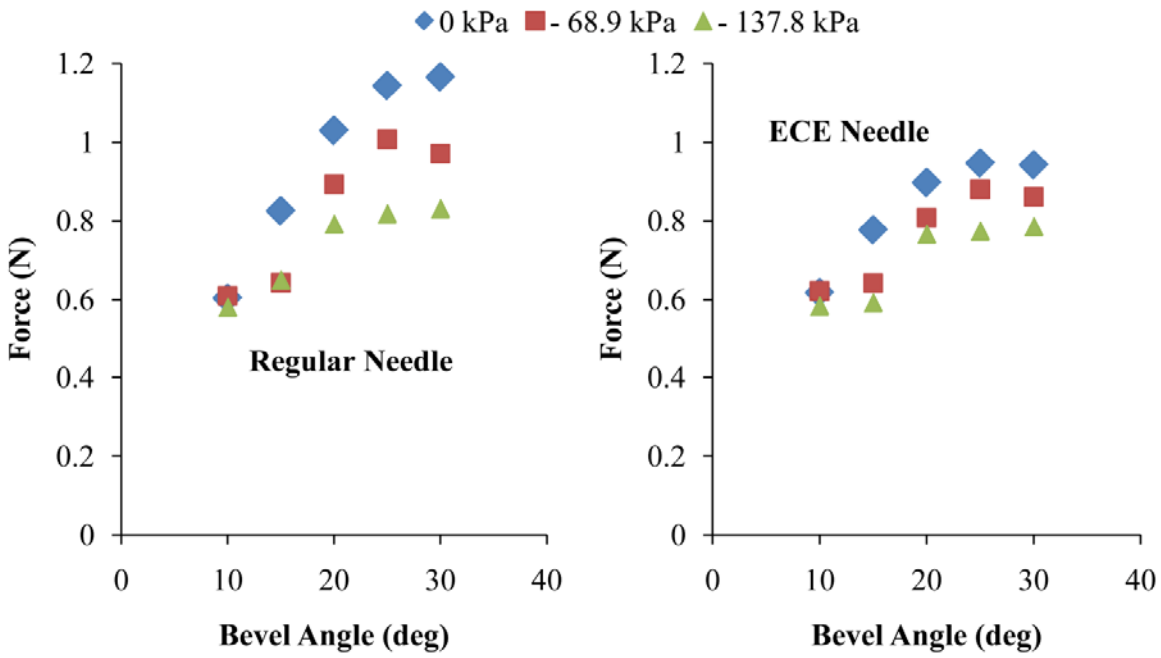

(A) (B)

Figure 5.12: Needle insertion force comparing pressure effect for (A) Regular and (B) ECE two-plane needles

5.4.2.3 S-Factor Variation for Vacuum

The *S* factor decreases at higher vacuum levels for both ECE and regular needles showing that vacuum improves cutting efficiency. The *S* factor in Equation 4.5 is determined using a least squares fit to the force data for the regular two-plane needles, shown in Figure 5.13, and ECE needles, shown in Figure 5.14, for all the three tested levels of internal needle pressure. The *S* factors determined give a reasonable fit to the experimental force data.

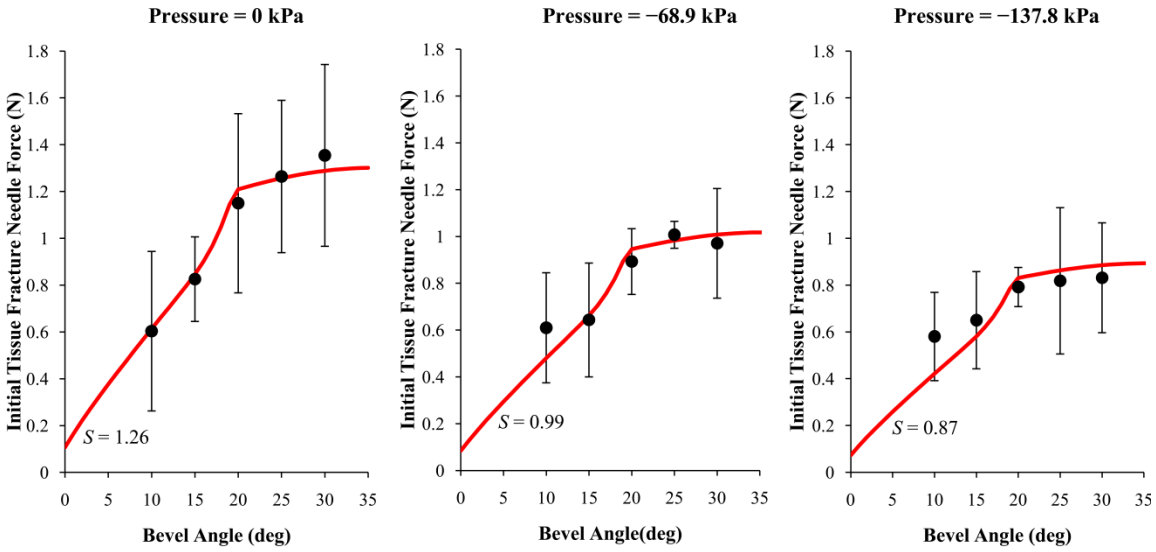

Figure 5.13: Regular two-plane needle pressure effect on *S* factor

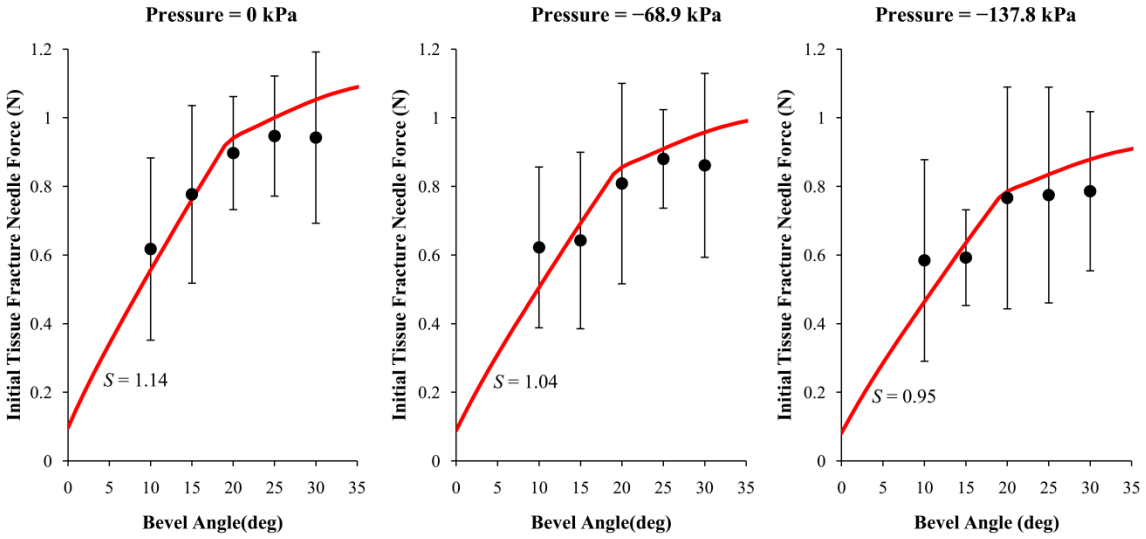

Figure 5.14: ECE two-plane needle pressure effect on *S* factor

Figure 5.15 shows that the *S* factor for both types of needles decreases at lower pressures. The *S* factors for both ECE and regular two-plane needles are close in value for the three given pressures. This similarity occurs because the *S* factor is independent of λ and α of the needle. The *S* factor depends on the needles diameter, thickness, and level of vacuum applied.

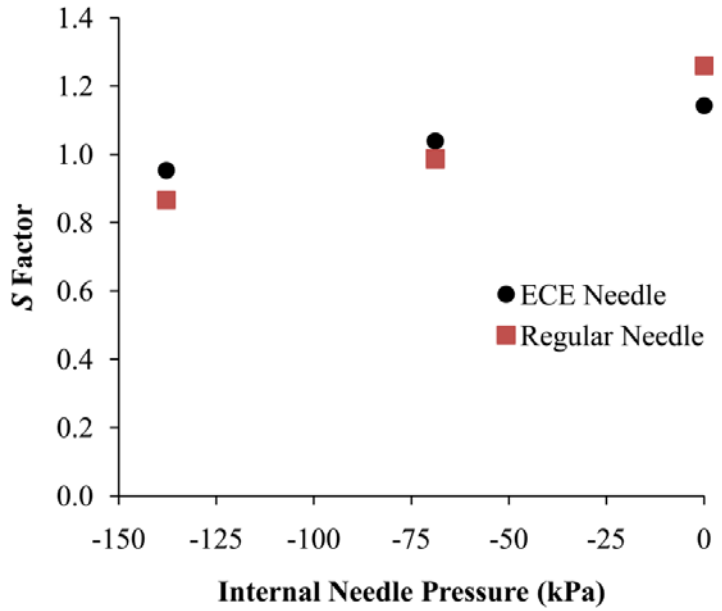

Figure 5.15: *S* factor compared to needle pressure

5.4.3 Comparing biopsy length to biopsy force

Figure 5.16 (A), (B), and (C) shows the relationship between needle insertion forces and biopsy length for internal needle pressures of 0 kPa, -68.9 kPa, and -137.8 kPa, respectively. Least squares fit linear lines are illustrated for both ECE and regular needles. It is shown that for both ECE and regular needles lower needle insertion forces coincide with longer biopsy lengths as shown with least squares fit linear lines all having negative slopes. Lower insertion forces are an indication of more efficient tissue cutting. More efficient tissue cutting leads to longer biopsy sample lengths.

Figure 5.17 illustrates the R^2 values for the linear least squares best fit lines. Higher levels of vacuum lead to higher R^2 values which indicate a more linear relationship. This improved linearity is a direct result of the vacuum force overcoming the internal needle friction which hinders longer biopsy lengths from being obtained. Figure 5.16(A) shows that for the internal needle pressure of 0 kPa both ECE and regular needles lower force corresponds to little improvement in biopsy length when $\xi = 10°$ and 20°. However, for the internal needle pressure of −68.9 kPa (Figure 5.16(B)) and −137.8 kPa (Figure 5.16(C)) lower forces correspond to significantly longer biopsy lengths even for the highest biopsy lengths found when $\xi = 10°$ and 20°.

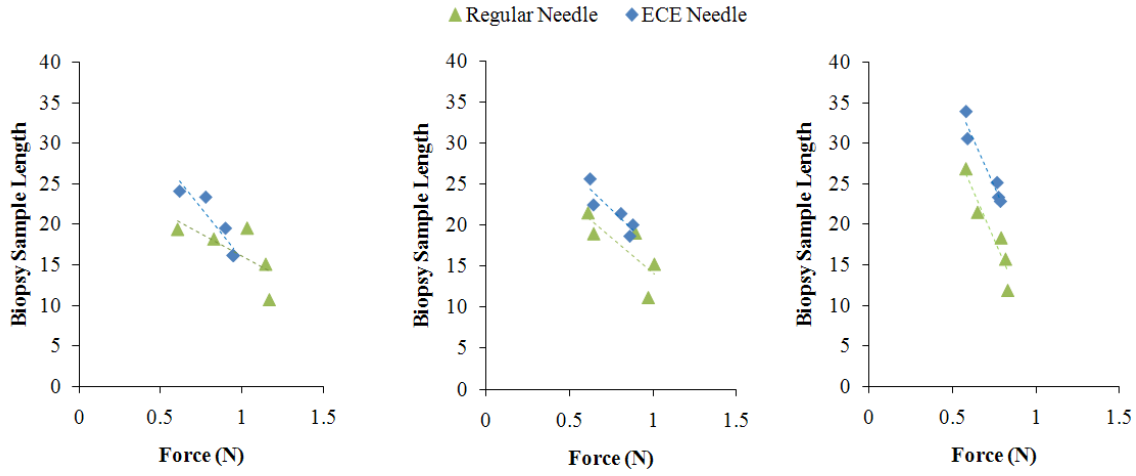

Figure 5.16: Needle insertion force compared to biopsy length with least squares best fit lines for needle pressures of (A) 0 kPa, (B) -68.9 kPa, and (C) -137.8 kPa

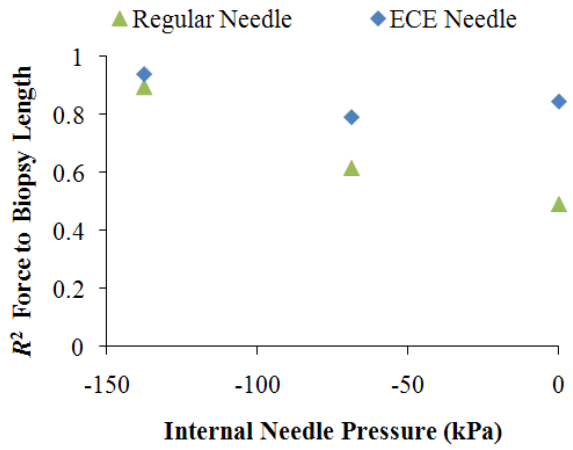

Figure 5.17: R^2 value for force to biopsy length

Higher vacuum allows for a steeper slope in force to biopsy length results as shown in Figure 5.18. This is a result of vacuum creating both lower needle insertion forces and longer biopsy lengths. The slope of both ECE and regular needles are shown to be very similar for the vacuum pressures of -68.9 kPa and -137.8 kPa. This can be

explained by the fact that internal needle friction is not hindering the biopsy length acquisition; therefore, the force of insertion is the only direct determinate of biopsy length regardless of the needle geometry, ECE or regular.

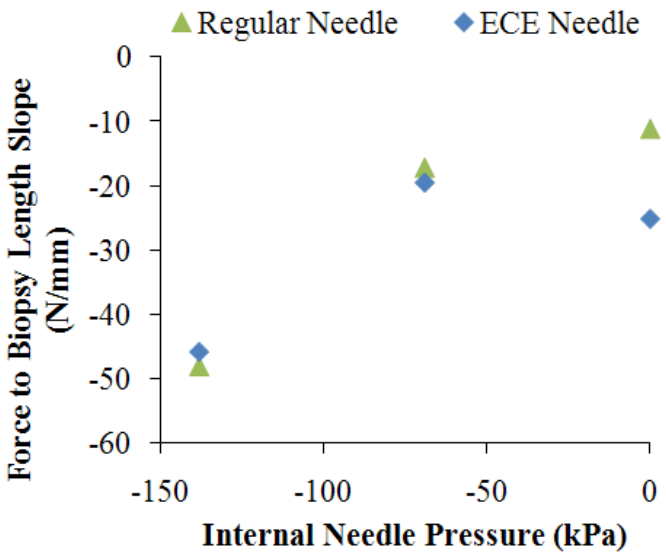

Figure 5.18: Force to biopsy length slope's magnitude increases as internal needle pressure decreases

5.5 Conclusions

The novel ECE needle tip design was proposed and experimentally determined to outperform the regular two-plane symmetric needle by on average yielding longer biopsy samples. Biopsy sample length is on average 22%, 30%, and 49% longer for ECE needle compared to that of regular needle for the internal pressures of 0, −68.9, and −137.8 kPa, respectively. The use of vacuum further improved the ECE needle tips biopsy sample length. For ECE needles the vacuum level of –137.8 kPa produces on average biopsy lengths that are 41, 31, 29, 45, and 42% longer compared to no vacuum for $\xi = 10°$, 15°, 20°, 25°, and 30°, respectively.

The force results showed the ECE needle could be inserted with less initial insertion force than the two-plane needle for needles where the needle tip was fully contacting the tissue upon insertion. Vacuum was also showed to help lower insertion forces. The *S* factor of the needle force model was shown to decrease upon increasing the vacuum, proving more efficient tissue cutting can take place with the use of vacuum.

The performance of the ECE needle is limited by the needle tip length. Results showed lower values of ξ improved biopsy performance but the needle tip length, which equals $r_i/\tan\xi$, increases greatly at lower ξ values. Too long of a needle tip length will cause the needle tip to become weaker which puts the needle at risk for bending or breaking inside the patient.

Results showed that higher vacuum can allow for longer biopsy lengths. However, too high of a vacuum may cause the tissue sample to be pulled into the vacuum hose making it difficult to be retrieved. High vacuum levels may also cause fragmented biopsy samples which cause less accurate diagnosis (Iczkowski 2002). Therefore, an optimal needle tip design would be the ECE needle at the lowest ξ and vacuum pressure that would still be safe for patient use and not lead to damaged or difficult to retrieve biopsy samples.

Chapter 6 Conclusions and Future Work

6.1 Conclusions

The need for biopsy needles to cut more efficiently has been well established with false negative biopsies reported to be as high as 24% (Lane 2008). More efficient biopsy tissue cutting leads to longer biopsy samples which allow for a more accurate diagnosis and a shorter less painful procedure. A lack of understanding about needle geometry has led to current needle designs which are not ideal for efficiently cutting tissue. This thesis fulfills this gap of knowledge by specifically addressing how geometrical characteristics of a needle tip affect a needles ability to cut tissue. The results of this thesis enhance the understanding of needle geometry, needle forces, and a needle tips ability to acquire long tissue samples. The major outcome of the thesis was the development of the enhanced cutting edge (ECE) needle which increases the inclination angles of a needle to create a better needle cutting geometry.

The major findings of this dissertation are:

- *Needle geometry defined*: The inclination angle, rake angle, needle tip insertion length, and needle tip insertion area were analytically solved for a wide variety of needle tip styles, including both flat plane and curved needle tip geometries. Based on these definitions it was found for plane needles that the maximum inclination angle is dictated by ξ ($\lambda \leq 90^{o}-\xi$) and other variables such as h, ψ, and the number of planes could only decrease this maximum. Similarly the rake angle of flat plane needles was limited by ξ ($\alpha \leq 90^{o}-\xi$). Curved surface needle tips had the ability to create more variation in inclination and rake angle than traditional plane needles. Unlike the bias bevel needle the inclination and rake angles were not identical at both the top and bottom of curved needle tips. This flexibility in choosing λ and α allows for greater freedom in creating designing needle tip geometry.

- *Needle tip contact length defined:* The contact length was determined through experimentation and analytical models were made. Experimental results showed that the oblique cutting tissue flow direction was different from Stabler's rule and dependent on not only the inclination angle but also the rake angle and, for the case of needle, the bevel angle ξ. For the needle it was observed that the tissue flow followed the direction of the *xz* plane across the needle tip surface. A contact length model based on this observation along with two other models were proposed and analyzed.
- *ECT based needle tip force model developed:* A mechanistic approach, using the ECT concept, was used to develop a force model based on λ and α. The approach demonstrated to accurately predict needle insertion forces. The force model was validated based on experimental force results obtained from five 11 gauge two-plane symmetric biopsy needles thereby proving the concept of using ECTs to develop a needle tip force model. The force model developed is shown to have an R^2 value of 0.979 when compared to the actual needle data. It was also found that cutting edges with higher λ cut tissue with lower cutting forces. Cutting edges with low λ (less than 30°) or a combination of high λ (greater than 70°) and low α (less than 10°) are demonstrated to produce a greater variation in cutting forces.
- *Novel ECE needle tip developed*: The novel ECE needle tip design was proposed and experimentally determined to outperform the regular two-plane symmetric needle by on average yielding longer biopsy samples. Biopsy sample length is on average 22%, 30%, and 49% longer for ECE needle compared to that of regular needle for the internal pressures of 0, −68.9, and −137.8 kPa, respectively. The use of vacuum further improved the ECE needle tips biopsy sample length. For ECE needles the vacuum level of –137.8 kPa produces on average biopsy lengths that are 41, 31, 29, 45, and 42% longer compared to no vacuum for ξ = 10°, 15°, 20°, 25°, and 30°, respectively. The force results showed the ECE needle could be inserted with less initial insertion force than the two-plane needle for needles where the needle tip was fully contacting the tissue upon insertion. Vacuum was also showed to help lower insertion forces. The *S* factor of the needle force model was shown to decrease upon increasing the vacuum, proving more efficient tissue cutting can take place with the use of vacuum.

The original contributions of this work are as follows:

(1) The geometrical cutting parameters of λ, α, L, A were defined for specific plane needle tip geometries.

(2) The geometrical cutting parameters of λ and α were generally defined for curved plane style needles.

(3) The oblique cutting tissue flow direction was experimentally determined and found to differ from Stabler's rule.

(4) A general needle force model was developed and validated for the specific case of an 11 gauge two plane needle.

(5) Improved needle geometry (ECE needle tip) was created and shown to outperform a regular needle.

6.2 Future Work

This dissertation focused on creating a better understanding of needle tip design to improve biopsy yield. Other factors including needle insertion speed, internal needle friction, and varying levels of internal needle vacuum can also affect biopsy yield. Biopsy yield of a needle can be further improved through the following research:

(1) Investigation in how insertion speed affects needle insertion force, and biopsy sample length. Determining the optimum insertion speed can allow for greater needle cutting efficiency.

(2) Determining internal needle friction and how it affects biopsy sample length. The internal needle friction directly hinders biopsy acquisition and through a better friction understanding this force can be reduced.

(3) Investigation in how varying levels of vacuum during needle insertion affect biopsy yield. The use of vacuum can be optimized to create longer biopsy samples.

(4) Investigation in needle tip insertion length and safety to the patient. Needle tips with lower bevel angles cut more efficiently but have much higher needle tip insertion lengths that could potentially break off or bend inside the patient. A study is necessary to determine how small the bevel angle can be but still be safe for clinical use.

Appendices

Appendix A: Non-Symmetric Two-Plane Needle Tip Point Location Equation

The solution of γ_A and γ_B are expressed below in terms of the parameter E_1 and E_2 with $0° < \psi < 180°$. In E_1 there is a minus sign in front of the square root while in E_2 there is a positive sign. If $\psi = 180°$ then the limit as ψ approaches 180° can be taken in order to find γ_A and γ_B.

$$\gamma_A = \tan^{-1}\left(\frac{r_o \tan\xi_1 - r_o \tan\xi_2 + h \tan\xi_2 \tan\xi_1}{-E_1 \tan\xi_1 \cos\psi} - \frac{\tan\xi_2}{\tan\xi_1 \cos\psi} + 1\right)$$

$$\gamma_B = \tan^{-1}\left(\frac{r_o \tan\xi_1 - r_i \tan\xi_2 + h \tan\xi_2 \tan\xi_1}{-E_2 \tan\xi_1 \cos\psi} - \frac{\tan\xi_2}{\tan\xi_1 \cos\psi} + 1\right)$$

where

$$\begin{aligned}(E_1, E_2) = & -h \tan^2\xi_2 \tan\xi_1 \\ & + r_o \tan^2\xi_1 \cos\psi - r_o \tan\xi_1 \tan\xi_2 \\ & + r_o \tan^2\xi_2 - r_o \tan\xi_1 \cos\psi \tan\xi_2 + h \tan^2\xi_1 \cos\psi \tan\xi_2 \\ & \pm \left[-h^2 \tan^4\xi_1 \tan^2\xi_2 + 2 r_o{}^2 \tan^3\xi_1 \tan\xi_2 - 2 r_o{}^2 \tan^3\xi_1 \cos\psi \tan\xi_2 \right. \\ & - 2 r_o{}^2 \tan^3\xi_1 \cos^2\psi \tan\xi_2 + h^2 \tan^4\xi_1 \cos^2\psi \tan^2\xi_2 \\ & + 2 r_o h \tan^4\xi_1 \cos^2\psi \tan\xi_2 - 2 r_o h \tan^3\xi_1 \cos^2\psi \tan^2\xi_2 \\ & + 2 r_o{}^2 \tan^3\xi_1 \cos^3\psi \tan\xi_2 - 2 r_o h \tan^4\xi_1 \tan\xi_2 \\ & \left. + 2 r_o h \tan^3\xi_1 \tan^2\xi_2\right]^{0.5} / (\tan^2\xi_2 - 2 \tan\xi_1 \cos\psi \tan\xi_2 + \tan^2\xi_1)\end{aligned}$$

Appendix B: High Speed Needle Biopsy Experiments

To measure the effect of insertion speed on both needle force and biopsy sample length, experiments were performed using a high speed pneumatic needle insertion device shown in Figure B.1. Figure B.2 shows the experimental setup using an earlier built high speed pneumatic device. Both devices use a pneumatic cylinder to propel a needle through the needle grid and into bovine liver. To record needle insertion force the bovine liver rests on top of a Kistler 9256A1 piezoelectric force dynamometer as illustrated in Figure B.2. A linear optical encoder, Heidenhain Lida 277 records the speed during needle insertion.

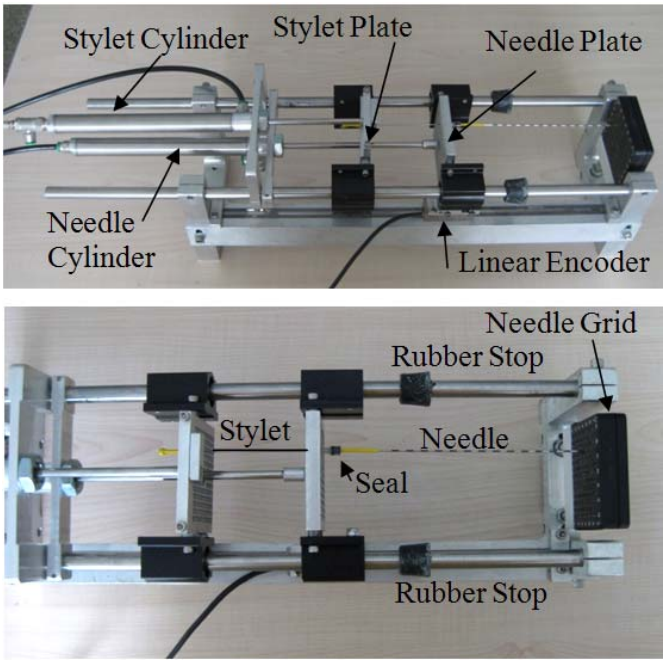

Figure B.1: High speed pneumatic needle insertion device used for experiments

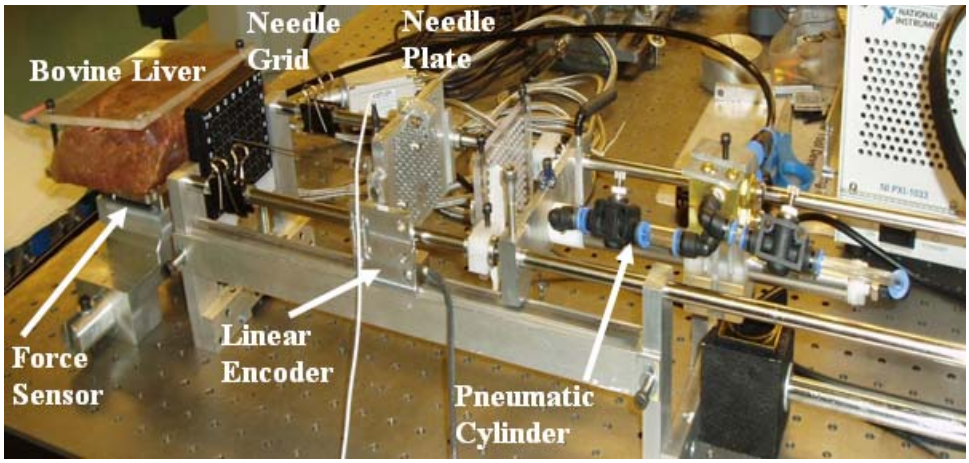

Figure B.2: Earlier higher speed pneumatic needle insertion device with bovine liver and force sensor

Two sets of biopsy needle experiments are performed using an 18 gauge UTW (OD 1.27 mm and ID 1.12 mm) two-plane symmetric needle with a bevel angle of 20°.

For the first set of experiments the needle is inserted at 10 different speeds ranging from 162 to 2120 mm/sec. Each experiment is repeated 3 times. The force is recorded throughout each insertion and averaged when the needle depth inside the bovine liver is between 20 and 30 mm as illustrated in Figure B.3(A), (B), (C), and (D) which shows the three force results for being inserted at 162, 995, 1137, and 2120 mm/s respectively. The depth range of 20 to 30 mm is chosen to ensure needle cutting is occurring but not so deep as to experience high levels of tissue friction. This average force is compared to the speed of insertion in Figure B.4. As shown the increased speed creates higher levels of force for the needle insertion. This can be explained because the tissue must accelerate faster away from the needle as it is cut at a greater speed. This higher acceleration of tissue mass creates a greater force necessary for needle insertion.

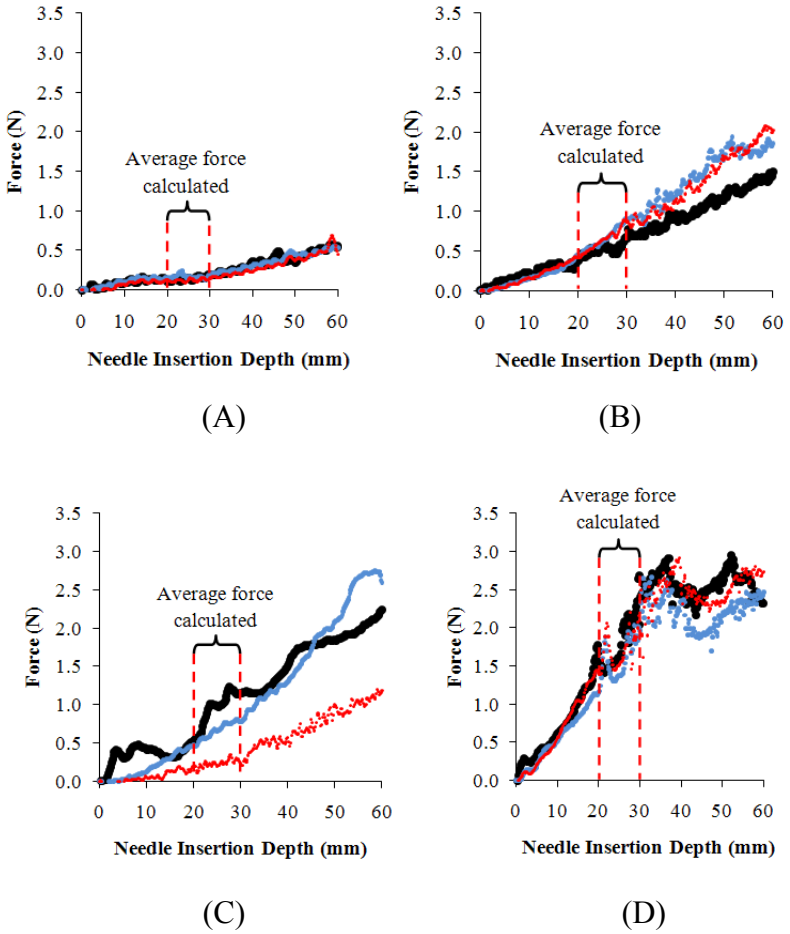

Figure B.3: Four needle force experiments conducted at (A) 162 mm/s, (B) 995 mm/s (D) 1137 mm/s and (C) 2120 mm/s

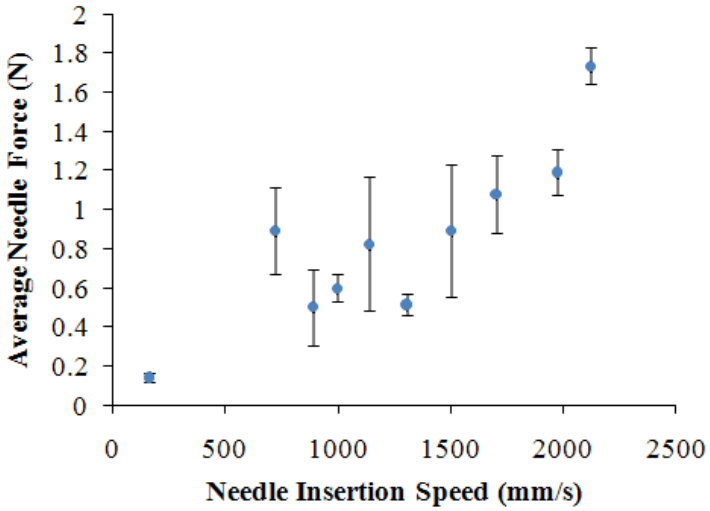

Figure B.4: Average needle force increases as speed of insertion increases

For the second set of experiments the same two plane symmetric needle is inserted at 3 different speeds (465, 751, and 983 mm/s) through 80 mm of tissue and the length of the biopsy sample is recorded. Each experiment is performed 3 times. Figure B.5 gives the results of how the biopsy length improves upon insertion. The higher insertion speeds allow for greater efficiency in cutting the tissue, thereby allowing for longer biopsy sample lengths.

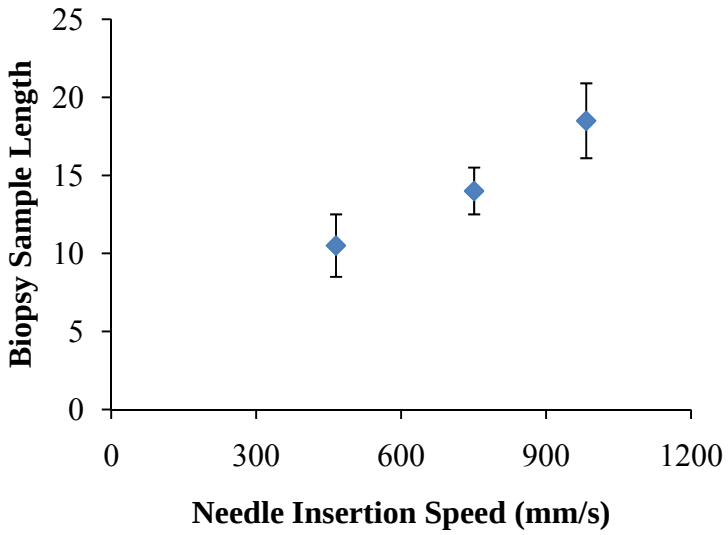

Figure B.5: Biopsy sample length improves with needle insertion speed

References

Abolhassani, N., R. Patel, and M. Moallem. (2007) "Needle insertion into soft tissue: A survey." *Medical Engineering & Physics* **29**(4):413-431.

Boothroyd, G.and W. Knight. (2006) *Fundamentals of Machining and Machine Tools*: Boca Raton, Taylor & Francis Group.

Brett, P.N., T.J. Parker, A.J. Harrison, T.A. Thomas, and A. Carr. (1997) "Simulation of resistance forces acting on surgical needles." *Proceedings of the Institution of Mechanical Engineers Part H-Journal of Engineering in Medicine* **211**(4):335-347.

Chanthasopeephan, T., J.P. Desai, and A.C.W. Lau. (2006) "Determining Fracture Characteristics in Scalpel Cutting of Soft Tissue." Pp. 899-904 in *Proceedings of the First IEEE/RAS-EMBS International Conference on Biomedical Robotics and Biomechatronics*. Piscataway, NJ 08855-1331, United States: Institute of Electrical and Electronics Engineers Computer Society.

Dehghan, E.and S.E. Salcudean. (2007) "Needle Insertion Point and Orientation Optimization in Non-linear Tissue with Application to Brachytherapy." Pp. 2267-2272 in *2007 IEEE International Conference on Robotics and Automation*.

DiMaio, S.P.and S.E. Salcudean. (2003) "Needle Insertion Modeling and Simulation." *IEEE Transactions on Robotics and Automation* **19**(5):864-875.

Ehmann, K.F., S.G. Kapoor, R.E. DeVor, and I. Lazoglu. (1997) "Machining process modeling: A review." *Journal of Manufacturing Science and Engineering-Transactions of the Asme* **119**(4B):655-663.

Fang, G.and P. Zeng. (2005) "Three-dimensional thermo-elastic-plastic coupled FEM simulations for metal oblique cutting processes." *Journal of Materials Processing Technology* **168**(1):42-48.

Fink, K.G., G. Hutarew, A. Pytel, and N.T. Schmeller. (2005) "Prostate biopsy outcome using 29 mm cutting length." *Urologia Internationalis* **75**(3):209-212.

Glozman, D.and M. Shoham. (2004) "Flexible Needle Steering and Optimal Trajectory Planning for Percutaneous Therapies." Pp. 137-144 in *Medical Image Computing and Computer-Assisted Intervention – MICCAI 2004*.

Haggarth, L., P. Ekman, and L. Egevad. (2002) "A new core-biopsy instrument with an end-cut technique provides prostate biopsies with increased tissue yield." *BJU Int* **90**(1):51-55.

Heverly, M., P. Dupont, and J. Triedman. (2005) "Trajectory optimization for dynamic needle insertion." Pp. 1646-1651in *Ieee International Conference on Robotics and Automation (Icra)*.

Hing, J.T., A.D. Brooks, and J.P. Desai. (2006) "Reality-based needle insertion simulation for haptic feedback in prostate brachytherapy." Pp. 619-624 in *IEEE International Conference on Robotics and Automation (Icra)*.

Hopper, K.D., C.S. Abendroth, K.W. Sturtz, Y.L. Matthews, J.S. Hartzel, and P.S. Potok. (1995) "Ct Percutaneous Biopsy Guns - Comparison of End-Cut and Side-Notch Devices in Cadaveric Specimens." *American Journal of Roentgenology* **164**(1):195-199.

Hopper, K.D., C.S. Abendroth, K.W. Sturtz, Y.L. Matthews, S.J. Shirk, and L.A. Stevens. (1993a) "Blinded Comparison of Biopsy Needles and Automated Devices in-Vitro .1. Biopsy of Diffuse Hepatic-Disease." *American Journal of Roentgenology* **161**(6):1293-1297.

Hopper, K.D., C.S. Abendroth, K.W. Sturtz, Y.L. Matthews, S.J. Shirk, and L.A. Stevens. (1993b) "Blinded Comparison of Biopsy Needles and Automated Devices in-Vitro .2. Biopsy of Medical Renal-Disease." *American Journal of Roentgenology* **161**(6):1299-1301.

Huber, R.L. (1946) Hypodermic needle, US patent 2 409 979, (October 22, 1946).

Iczkowski, K.A., G. Casella, R.J. Seppala, G.L. Jones, B.A. Mishler, J.Q. Qian, and D.G. Bostwick. (2002) "Needle core length in sextant biopsy influences prostate cancer detection rate." *Urology* **59**(5):698-703.

Kataoka, H., T. Washio, K. Chinzei, K. Mizuhara, C. Simone, and A. Okamura. (2002) "Measurement of the Tip and Friction Force Acting on a Needle during Penetration." Pp. 216-223 in *Medical Image Computing and Computer-Assisted Intervention — MICCAI 2002*.

Kucklick, T.R. 2006. *The medical device R & D handbook*. Boca Raton: CRC/Taylor & Francis.

Lane, B.R., A.S. Moussa, C.D. Zippe, R. Abouassaly, L. Schoenfeld, C. Magi-Galluzzi, and J.S. Jones. (2008) "Saturation technique does not reduce cancer detection during follow-up after initial prostate biopsy." *Journal of Urology* **179**(4):716-717.

Lehman, C.D.and T. Aikawa. (2004) "MR-guided vacuum-assisted breast biopsy: Accuracy of targeting and success in sampling in a model." *Radiology* **232**(3):911-914.

Li, R.and A.J. Shih. (2007) "Tool temperature in titanium drilling." *Journal of Manufacturing Science and Engineering-Transactions of the Asme* **129**(4):740-749.

Luk, W.K. (1972) "The Direction of Chip Flow in Oblique Cutting." *International Journal of Production Research*, **10**:67-76.

Moore, J.Z., C.S. McGill, Q. Zhang, P.W. McLaughlin, H. Zheng, and A.J. Shih (2009a). "Blade Oblique Cutting of Tissue for Investigation of Biopsy Needle Insertion." *Transactions of NAMRI/SME*, **37**:49-56.

Moore, J.Z., Q. Zhang, C.S. McGill, P.W. McLaughlin, H. Zheng, and A.J. Shih (submitted 2009b). "Modeling Cutting Edge Geometry for Plane and Curved Needle Tips." *Proceedings of the Institution of Mechanical Engineers Part B: Journal of Engineering Manufacture*.

Moore, J.Z., C.S. McGill, Q. Zhang, P.W. McLaughlin, H. Zheng, and A.J. Shih (2010a) "Cutting Edge Rake and Inclination Angles Modeling for Plane Needles." *Journal of Manufacturing Science and Engineering*, **132**(5):051005-1-8.

Moore J.Z., A.J. Shih (2010b) "Tissue Oblique Cutting Flow Angle and Needle Insertion Contact Length." *Transactions of NAMRI/SME*, **38**:711-718.

Moore J.Z., K. Malukhin, A. Shih, and K. Ehmann, (submitted 2010c) "Hollow Needle Tissue Insertion Force Model." *CIRP Annals*.

Moore J.Z., A.J. Shih (submitted 2010d) "Tissue Oblique Cutting Flow Angle and Needle Insertion Contact Length." *Medical Physics*.

Okamura, A.M., C. Simone, and M.D. O'Leary. (2004) "Force Modeling for Needle Insertion into Soft Tissue." *IEEE Transactions on Biomedical Engineering* **51**(10):1707-1716.

O'Leary, M.D., C. Simone, T. Washio, K. Yoshinaka, and A.M. Okamura. (2003) "Robotic needle insertion: effects of friction and needle geometry." Pp. 1774-1780 in *Robotics and Automation, 2003. Proceedings. ICRA '03. IEEE International Conference on*.

Ozden, E., C. Gogus, O. Tulunay, and S. Baltaci. (2004) "The long core needle with an end-cut technique for prostate biopsy: does it really have advantages when compared with standard needles?" *Eur Urol* **45**(3):287-291.

Podder, T.K., D.P. Clark, J. Sherman, D. Fuller, E.M. Messing, D.J. Rubens, J.G. Strang, Y.D. Zhang, W. O'Dell, W.S. Ng, and Y. Yu. (2005) "Effects of tip geometry of

surgical needles: an assessment of force and deflection." in *3rd European Medical and Biological Engineering Conference*. Prague, Czech Republic.

Podder, T.K., J. Sherman, E. Messing, D.J. Rubens, D. Fuller, J.G. Strang, R.A. Brasacchio, and Y. Yu. (2006) "Needle Insertion Force Estimation Model Using Procedure-specific and Patient-specific Criteria." Pp. 555-558 in *Annual International Conference of the IEEE Engineering in Medicine and Biology Society*. Piscataway, NJ, USA: IEEE.

Race, G.J., G.W. Tillery, and P.A. Dysert, 2nd. (2004) "A history of pathology and laboratory medicine at Baylor University Medical Center." *Proc (Bayl Univ Med Cent)* **17**(1):42-55.

Russell, J.K., and R.H. Brown (1966) "Measurement of Chip Flow Direction." *International Journal of Machine Tool Design and Research*, **6:**129-138.

Sarvazyan, T., V. Stolarsky, B. Fishman, and A. Sarvazyan. (1998) "Development of Mechanical models or Breast and Prostate with Palpable Nodules." *International Conference of the IEEE Engineering in Medicine and Biology Society* **20**(2).

Shih, A.J., M.A. Lewis, and J.S. Strenkowski. (2004) "End milling of elastomers - Fixture design and tool effectiveness for material removal." *Journal of Manufacturing Science and Engineering-Transactions of the Asme* **126**(1):115-123.

Stabler, G.V. (1951) "The Foundational Geometry of Cutting Tool." Proceedings of the Institution of Mechanical Engineers, **165**:14-26.

Stephenson, D.A.and J.S. Agapiou. (2006) *Metal cutting theory and practice*. Boca Raton, FL: CRC Taylor & Francis.

Ubhayakar, G.N., W.Y. Li, C.M. Corbishley, and U. Patel. (2002) "Improving glandular coverage during prostate biopsy using a long-core needle: technical performance of an end-cutting needle." *BJU Int* **89**(1):40-43.

Webster III, R.J., N.J. Cowan, G. Chirikjian, and A. Okamura. (2006) "Nonholonomic Modeling of Needle Steering." Pp. 35-44 in *Experimental Robotics IX*.

Wen, D.H., L. Zheng, Z.Z. Li, and R.S. Hu. (2004) "On the prediction of chip flow angle in non-free oblique machining." *Proceedings of the Institution of Mechanical Engineers Part B-Journal of Engineering Manufacture* **218**(10):1267-1278.

Zerbino, D.D. (1994) "[Biopsy: its history, current and future outlook]." *Lik Sprava* (**3-4**):1-9.

Zheng, H., Q. Zhang, J. Moore, J. Schwartz, C.S. McGill, P.W. McLaughlin, and A.J. Shih (2009) "Biopsy Needle Tissue Cutting Analysis." *Proceedings of the 8th International Conference on Frontiers of Design and Manufacturing.*